

INFORMATION TO USERS

This material was produced from a microfilm copy of the original document. While the most advanced technological means to photograph and reproduce this document have been used, the quality is heavily dependent upon the quality of the original submitted.

The following explanation of techniques is provided to help you understand markings or patterns which may appear on this reproduction.

1. The sign or "target" for pages apparently lacking from the document photographed is "Missing Page(s)". If it was possible to obtain the missing page(s) or section, they are spliced into the film along with adjacent pages. This may have necessitated cutting thru an image and duplicating adjacent pages to insure you complete continuity.
2. When an image on the film is obliterated with a large round black mark, it is an indication that the photographer suspected that the copy may have moved during exposure and thus cause a blurred image. You will find a good image of the page in the adjacent frame.
3. When a map, drawing or chart, etc., was part of the material being photographed the photographer followed a definite method in "sectioning" the material. It is customary to begin photoing at the upper left hand corner of a large sheet and to continue photoing from left to right in equal sections with a small overlap. If necessary, sectioning is continued again -- beginning below the first row and continuing on until complete.
4. The majority of users indicate that the textual content is of greatest value, however, a somewhat higher quality reproduction could be made from "photographs" if essential to the understanding of the dissertation. Silver prints of "photographs" may be ordered at additional charge by writing the Order Department, giving the catalog number, title, author and specific pages you wish reproduced.
5. PLEASE NOTE: Some pages may have indistinct print. Filmed as received.

University Microfilms International

300 North Zeeb Road
Ann Arbor, Michigan 48106 USA
St. John's Road, Tyler's Green
High Wycombe, Bucks, England HP10 8HR

77-12,733

CHANG, Len-Fu Walter, 1948-
A NUMERICAL STUDY OF THE DIURNAL VARIATION
OF THE LOW-LEVEL JET.

The University of Oklahoma, Ph.D., 1976
Physics, atmospheric science

Xerox University Microfilms, Ann Arbor, Michigan 48106

THE UNIVERSITY OF OKLAHOMA
GRADUATE COLLEGE

A NUMERICAL STUDY OF THE DIURNAL
VARIATION OF THE LOW-LEVEL JET

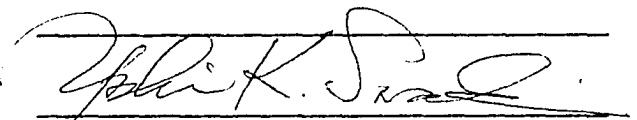

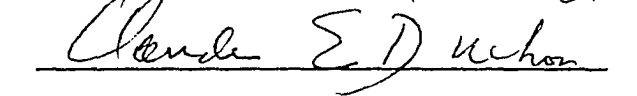
A DISSERTATION
SUBMITTED TO THE GRADUATE FACULTY
in partial fulfillment of the requirements for the
degree of
DOCTOR OF PHILOSOPHY

BY
LEN-FU WALTER CHANG
Norman, Oklahoma
1976

A NUMERICAL STUDY OF THE DIURNAL
VARIATION OF THE LOW-LEVEL JET

APPROVED BY



DISSERTATION COMMITTEE

ABSTRACT

Southerly flow over the eastern slope of the Rocky Mountains under the influence of a diurnal surface temperature wave is studied by numerical experiments and by analytic methods. The purpose of this study is to determine the interrelationships of various processes associated with the diurnal variation of the low-level jet.

Analytic solutions have been obtained in order to diagnose the structure of the boundary layer of a rotating stratified fluid over a sloping surface undergoing heating and cooling. The results show that the thermal and momentum fields of this boundary layer are coupled; the cross-isobar boundary layer flow is increased by the effect of a buoyant force along the direction of the terrain slope. Also, the vertical motion field is shown to be controlled by two mechanisms, namely, Ekman pumping and buoyant pumping, respectively.

For the numerical experiments, a two-dimensional meso-scale model has been adopted. The horizontal domain (east-west direction, perpendicular to the sloping terrain) is 1000 km in extent and is resolved by 21 grid points. The vertical domain extends to 4000 m above the ground and is resolved by 22 grid points. Turbulent transport of momentum

and sensible heat and the radiational cooling process are included in the model through parameterizations. A geostrophic wind field with shear in the horizontal direction only is specified as an initial condition.

The diurnal variation of the vertical profiles of wind and potential temperature are in good agreement with observations. Most important, the diurnal variation of the momentum field and the evolution of the low-level jet is well simulated; this development is characterized by a significant increase of wind shear in both directions (x, z). The mechanisms which are responsible for this two-dimensional low-level jet are the self-organization processes of the turbulent boundary layer. The vertical motion field (and low-level convergence) is found to be closely related to the processes associated with the formation of the low-level jet. The maximum amplitude of this field occurs in the early evening hours, and internal gravity waves are excited during this period.

ACKNOWLEDGMENTS

I wish to express my sincere thanks to Professor Rex Inman for his enduring encouragement, inspiration and guidance throughout my graduate study in Norman. I also wish to thank Professors Y. K. Sasaki, C. E. Duchon, J. S. Fein, J. F. Kimpel, E. F. Blick and M. C. Jischke for their many helpful suggestions. I also thank Ms. Jo Ann Oberst for her expert and patient typing of the manuscript.

This research was supported by the National Severe Storms Laboratory, National Oceanic and Atmospheric Administration, Contract 04-6-022-44002, and by the George C. Marshall Space Flight Center, Contract NAS8-31377.

TABLE OF CONTENTS

	Page
LIST OF FIGURES	vii
LIST OF TABLES	ix
LIST OF SYMBOLS	x
Chapter	
I. INTRODUCTION	1
II. BUOYANT-EKMAN LAYER THEORY AND ITS APPLICATIONS	9
III. THE NUMERICAL MODEL AND THE EXPERIMENTS	23
IV. RESULTS AND COMPARISONS	41
V. SUMMARY AND SUGGESTIONS	58
BIBLIOGRAPHY	63
APPENDIX A	92
APPENDIX B	96
APPENDIX C	101

LIST OF FIGURES

Figure	Page
1. Sloping terrain coordinate system	67
2a. Initial u-, v-field for Case IV and Case V (1000 LST).	68
2b. Initial potential temperature field for Case IV and Case V (1000 LST)	68
3. Diurnal surface temperature waves	69
4a. Wind field for Case IV (1200 LST)	70
4b. Wind field for Case IV (1400 LST)	70
4c. Wind field for Case IV (1600 LST)	71
4d. Wind field for Case IV (1800 LST)	71
4e. Wind field for Case IV (2000 LST)	72
4f. Wind field for Case IV (2200 LST)	72
4g. Wind field for Case IV (2400 LST)	73
4h. Wind field for Case IV (0200 LST)	73
4i. Wind field for Case IV (0400 LST)	74
4j. Wind field for Case IV (0600 LST)	74
4k. Wind field for Case IV (0800 LST)	75
4l. Wind field for Case IV (1000 LST)	75
4m. Wind field for Case IV (1200 LST)	76
4n. Wind field for Case IV (1400 LST)	76
4o. Wind field for Case IV (1600 LST)	77
5. Potential temperature profiles for the middle grid point for Case IV.	78
6. Surface heat fluxes predicted by the model for Case IV	79
7. u-profiles for the middle grid point for Case I (slope = 0)	80

Figure	Page
8. v-profiles for the middle grid point for Case I (slope = 0)	81
9. Diurnal variation of PBL depth for the middle grid point for Case I	82
10. Diurnal variation of veering angle profiles for the middle grid point for Case I.	83
11. Schematic diagram showing the diurnal variation of PBL depth as suggested by Hoxit.	84
12. Diurnal variation of veering angle profiles observed by Hoxit	84
13. Diurnal variation of u-profiles for the middle grid point for Case II.	85
14. Diurnal variation of v-profiles for the middle grid point for Case II.	86
15. Hodographs for the middle grid point at an altitude 625 m above ground (Case I, Case II) . .	87
16. Diurnal variation of the surface geostrophic wind for the middle grid point for Case I and Case II	87
17. A comparison of diurnal wind variations associated with large and small amplitude surface temperature waves (y-component)	88
18. Same as Fig. 17, except for the x-component	88
19. A comparison of diurnal wind variations at different latitudes (y-component)	89
20. Same as Fig. 19, except for x-component of wind	89
21. Vertical velocity at 2 km above ground for Case IV	90
22. Vertical velocity at 2 km above ground for Case V.	91
C.1. Relative amplitude of the spurious wave as a function of the wave number of the incident wave.	106

LIST OF TABLES

Table		Page
1.	Summary of parameters specified in the six numerical experiments	42
C.1.	Correlation coefficients showing the relationship between analytic solutions and numerical solutions of the advection equation obtained with an open boundary condition	109

LIST OF SYMBOLS

A	Amplitude of incident wave
A_R	Amplitude of supurious wave
A_T	Amplitude of transmissive wave
B_1, B_2, B_3	Amplitudes of diurnal surface temperature wave
C	Phase speed
\tilde{C}	Phase speed of incident wave
c_p	Specific heat at constant pressure
C_x	Component of phase speed along x-direction
D	Mean depth of the atmosphere overlying the sloping terrain
D	Horizontal divergence
E	The Ekman number
f	The Coriolis parameter
\hat{f}	$f \cos \varphi$
\vec{g}	Gravitational acceleration vector
g	Gravitational acceleration
$h(t)$	Time-varying depth of planetary boundary layer
h_c	Depth of constant flux layer
H	Scale height of atmosphere
i	Finite-difference space index in x-direction
j	Finite-difference space index in z-direction
K_M	Turbulent exchange coefficient for momentum
K_H	Turbulent exchange coefficient for sensible heat
k	von-Kármán's constant
k	Wave number in x-direction
L	Horizontal scale of sloping terrain

LST	Local standard time
n	Finite-difference time index
N	Brunt-Väsäili frequency
O()	Order of magnitude
p	Pressure
p_0	Reference pressure
\hat{p}	p/ρ_m
R_0	Rossby number
R	Gas constant for dry air
S	Measure of static stability
T_s	Surface temperature
\bar{T}_s	Mean surface temperature
\bar{T}	Mean temperature of constant flux layer
ΔT_s	$T_s - \bar{T}_s$
Δt	Time step for finite-difference time integration
$\tan \phi$	Slope of terrain
u_{*0}	Friction velocity
\bar{u}_I	Initial x-component of wind
U	Scale velocity of horizontal wind
\bar{v}_I	Initial y-component of wind
V_g	Geostrophic wind
$(\overline{w'\theta'})$	Kinematic surface heat flux
Δx	Grid distance in x-direction
Δz	Grid distance in z-direction
α_m	Mean thermal expansion coefficient
β	Buoyancy parameter

γ_{θ}	Proportionality constant for radiational cooling
Γ	Mean lapse rate of temperature
η	$E^{-\frac{1}{2}} z$
θ_*	Characteristic potential temperature of constant flux layer
θ_s	Time varying surface potential temperature
$\bar{\theta}_I$	Initial potential temperature
$\hat{\theta}$	$\theta - g \alpha_m$
$\bar{\theta}_m$	Mean potential temperature of atmosphere
λ	Aspect ratio
μ	Wave number in z-direction
ν	Kinematic viscosity; the frequency of the wave solution
π	$(p_0/p)^{R/C_p}$
$\bar{\pi}_I$	Initial pressure
ζ	Density of dry air
ζ_m	Mean density of atmosphere
$ \vec{\tau} $	Magnitude of surface stress

A NUMERICAL STUDY OF THE DIURNAL
VARIATION OF THE LOW-LEVEL JET

CHAPTER I

INTRODUCTION

The planetary boundary layer (PBL) is the lowest 1 ~ 2 km layer of the atmosphere which is significantly affected by surface conditions. Surface friction and surface heating are the dominant factors which control the characteristics of the PBL. The situation becomes complicated for planetary flow over a continental surface. The inhomogeneity of the distribution of mountains, hills, forest, and urban areas, etc. may cause additional perturbations in planetary flow. From the point of view of numerical weather prediction weather events are solutions of a set of mathematical equations, corresponding to various combinations of initial and boundary conditions. Because of the lack of adequate knowledge of the physical processes induced by the boundary conditions, current models are formulated with very simple or even without treatment of these boundary conditions. Thus, weather events predicted by these models are primarily dictated by initial conditions specified for the planetary flow. The initial state of kinetic energy,

potential energy, and internal energy determines the evolution of weather events through nonlinear energy cascade processes. This situation is probably one of the major reasons for the limitation of predictability of current models. The problem of determining to what extent boundary layer processes can affect planetary flow both temporally and spatially remains as the next frontier of research in meteorology.

Many examples of weather disturbances which are closely related to boundary layer processes can be found. We do know a considerable amount about the upper-level frontogenesis process; however, frontogenesis near the surface (Sanders, 1955) still is not well understood because it is affected by relatively unclear boundary layer processes. Similarly, the relation between the dry-line and low-level confluence zones is unclear, although it is of much interest because of its importance in thunderstorm forecasting over high terrain. In order to investigate phenomena of this kind one must make adequate assumptions to define the localized phenomena such that the system of interest is well isolated from the large scale prevailing circulations. Only under these assumptions can one understand the cause and effect relationships. The validity of these assumptions may be justified by consideration of the distinct time and space scales associated with the large and small scale circulations, respectively.

Micrometeorologists and turbulence dynamists have directed their interest to theories of the constant flux layer

and of the planetary boundary layer, in highly idealized situations. Assumptions of horizontal homogeneity and fixed upper and lower boundary conditions are generally used such that similarity theory can be developed to a high degree. It is of practical urgency to check the applicability of these theories in general cases through numerical experiments; this is the parameterization problem.

One of the boundary layer phenomena which has been documented in detail both observationally and theoretically is the low-level jet stream; however, some important problems still remain. The definition of the low-level jet utilized in the literature is ambiguous. The low-level jet, in comparison with the upper-level jet stream, should be a core of flow with a high concentration of momentum, except it is found in the lower portion of the atmosphere. Thus, the low-level jet may be defined as a two-dimensional core of high velocity flow which is located near the surface such that its behavior is closely related to boundary layer processes. In other works the low-level jet is sometimes defined in terms of a maximum of horizontal wind speed in a low-level vertical profile. In order to distinguish these two phenomena, the terminology one-dimensional (1-D) low-level jet and two-dimensional (2-D) low-level jet are used to avoid this ambiguity. Hoxit (1973), by analyzing low-level wind data, found that the 1-D low-level jet is a common phenomenon of the boundary layer over continental areas, especially in the summer season when the surface

receives maximum radiational heating. Bonner (1968), in his study of the climatology of the l-D low-level jet, has shown that the place of maximum frequency of occurrence of this phenomenon is located to the east of the Rocky Mountains and within a latitudinal band of about $35^{\circ} \sim 45^{\circ}\text{N}$.

A significant feature of the formation of the low-level jet is the diurnal variation of the horizontal wind in the PBL. Hoecker (1963) has observed that the horizontal winds are sub-geostrophic during the daytime and super-geostrophic at nighttime. The two-dimensional low-level jet has been depicted by Wexler (1961) using observational data for a cross-section perpendicular to the jet stream. He found that the low-level wind field experiences a strong diurnal variation of wind speed about a mean state. Also, this variation seemingly is associated with the low-level lapse rate of temperature; the wind speed is a minimum when a super-adiabatic lapse rate exists in the lower levels. On the other hand a well defined low-level jet develops when a stable lapse rate of temperature is in existence.

The low-level jet has aroused wide attention and interest not only because of the phenomenon itself, but because of its close relationship with meso-scale disturbances. Pitchford and London (1962) have shown that the location of high frequency of occurrence of nocturnal thunderstorms coincides with areas characterized by high frequency of occurrence of the low-level jet. Sangster (1967) showed that in this area the surface

geostrophic wind experiences a diurnal cycle of variation with the maximum surface geostrophic wind occurring during the daytime. Sangster believes that this variation of the surface geostrophic wind must have a close relationship with the low-level jet. From this information about the low-level jet, it seems natural that the question about the cause and effect relationship of these different features accompanying the development of the low-level jet needs to be answered. The relationship between the low-level jet and the low-level convergence and/or divergence fields is of special interest and importance from the point of view of interaction of mesoscale and small scale phenomena. Also, since the low-level jet phenomenon is closely associated with specific terrain and with diurnal heating and cooling of the surface these two factors need to be critically evaluated.

The diurnal variation of the low-level wind field has been theoretically studied by several authors. The most important theories which concern the 1-D low-level jet have been proposed by Bujitti and Blackadar (1957) and Holton (1967), respectively. They deal with two different mechanisms which may cause low-level wind variations. Bujitti and Blackadar assumed that the diurnal variation of the lapse rate of temperature in the lower atmosphere affects the efficiency of the turbulent momentum transport process. This effect is explicitly shown by the diurnal variation of the value of the turbulent exchange coefficient K_M . An analytic solution

derived by them well simulates the diurnal wind variation seen in the vertical wind profile. Holton discussed a large scale "drainage" wind caused by the downslope movement of radiationally cooled air along the slope of the Rocky Mountains. This gravitational drainage mechanism implies that the thermal and viscous boundary layer are coupled through the diurnally oscillating density field, and that the diurnal low-level wind oscillation over a sloping terrain is driven by this density oscillation. Combination of the mechanisms associated with terrain and the turbulent exchange coefficients may explain the intensity of the 1-D low-level jet observed over the central Great Plains (Bonner et al., 1970). However, the relationship of the concepts of the drainage wind and of the surface geostrophic wind has been unclear. On the other hand, conditions which favor the formation of the 1-D low-level wind maxima do not necessarily guarantee the formation of the two-dimensional low-level jet. For example, low-level wind maxima may develop in the vertical profiles with no apparent increase of the horizontal wind shear. A significant increase of the wind shear in both the vertical and horizontal directions is a necessary condition for the development of the two-dimensional low-level jet. Wexler (1961) noticed this point and proposed a theory of the 2-D low-level jet analogous to the theory of the Gulf Stream. Both are geophysical flows blocked on the western boundary. The Gulf Stream theory can partly explain the development of the

horizontal shear but not the vertical shear of the low-level jet. Consequently, these problems remain to be thoroughly studied and explained.

Considering the relation between the low-level jet and the low-level convergence field, Tepper (1955) applied the geostrophic adjustment theory to explain the relationship between gravity waves and the low-level jet in the state of super-geostrophy. According to this theory, the horizontal velocity convergence (associated with gravity waves) in the flow must occur after the maximum development of the low-level jet. This implies that the convective system must occur several hours after the maximum development of the low-level jet. This is not consistent with climatological evidence presented by Wallace (1975).

In order to study these phenomena and their interrelationships, it is intended to develop a unified theory of the low-level jet over the central Great Plains. Holton's ideas concerning the coupling of the thermal and viscous boundary layers are further extended by the development of the buoyant-Ekman layer theory in Chapter II. From analytical results characteristic structures of the momentum and thermal fields of the boundary layer over sloping terrain are revealed. Thus, the concepts of the "drainage" wind (Holton, 1967) and the surface geostrophic wind (Sangster, 1967) become related and clear. In addition, because of rapid progress in the development of the theory of the planetary boundary layer

in recent years, these up-to-date theories have been incorporated into the turbulent parameterization within the numerical model. Numerical experiments are carried out to test the diurnal variation of the low-level jet in a two-dimensional model. In addition, the free atmosphere and the boundary layer are coupled within the model such that the feedback effects of the boundary layer can be examined. The design of the model, the experiments, and the results are discussed in the following chapters.

CHAPTER II

BUOYANT-EKMAN LAYER THEORY

AND ITS APPLICATIONS

The major forces acting in a rotating and stratified fluid with a flat bottom surface are the Coriolis, pressure gradient, and frictional forces. In this type of boundary layer, which is known as the Ekman layer, stratification plays only a secondary role. But in the case of a boundary layer with a sloping bottom surface a component of the gravitational force is parallel to the bottom and the characteristics of the Ekman layer may be modified as long as temperature perturbations occur at the bottom boundary. In some situations the buoyancy force may be of the same order of magnitude as other forces; thus hereafter, the boundary layer above a sloping bottom surface is called the buoyant-Ekman layer to distinguish it from the normal Ekman layer. Below, a scale analysis will be completed to show the importance of the buoyant forces. Then the equations will be solved by regular and singular perturbation methods which are described in Greenspan (1968) and Cole (1968). Hseuh (1968) studied the buoyant-Ekman layer, especially the thickness of the layer; here this type of treatment is extended to include heating and cooling processes

of the buoyant-Ekman layer which resemble the diurnal heating and cooling of the PBL along sloping terrain. The analysis is attempted in an effort to explain that the heating and cooling processes of the buoyant-Ekman layer causes an increase or decrease of the low-level geostrophic wind. The analysis also shows that heating and cooling of the buoyant-Ekman layer may enhance the Ekman pumping effect (see Greenspan, 1968 or Holton, 1972).

The Basic Equations and the Scale Analysis

Consider a rotating and stratified fluid in the coordinate-system shown in Fig. 1; the x' -coordinate is to the east and the z' -coordinate is upward. The x - z coordinates represent a sloping-terrain coordinate system. Here it is assumed that the fluid properties are homogeneous along the y -direction. Furthermore, it is assumed that the Prandtl number is unity, i.e., the kinematic viscosity and the thermal conductivity are equal. Finally, if the scale height of the atmosphere ($H = \alpha_m / (d\bar{\theta}/dz)$) is much larger than the depth, D , of the fluid the Boussinesq assumption is valid (Spiegel and Veronis, 1960). Under the above conditions the governing equations may be written as

$$\frac{\partial u}{\partial t} + \vec{V} \cdot \nabla u - f \cos \varphi v = - \frac{1}{\rho_m} \frac{\partial p}{\partial x} - g \alpha_m \theta \sin \varphi + \nu \nabla^2 u, \quad (1)$$

$$\frac{\partial v}{\partial t} + \vec{V} \cdot \nabla v + f \cos \varphi u = \nu \nabla^2 v, \quad (2)$$

$$\frac{\partial w}{\partial t} + \vec{V} \cdot \nabla w = - \frac{1}{\rho_m} \frac{\partial p}{\partial z} + g \alpha_m \theta \cos \varphi + \nu \nabla^2 w, \quad (3)$$

$$\frac{\partial \theta}{\partial t} + \vec{V} \cdot \nabla \theta + \Gamma (-\sin \varphi u + \cos \varphi w) = \nu \nabla^2 \theta , \quad (4)$$

$$\frac{\partial u}{\partial x} + \frac{\partial w}{\partial z} = 0 . \quad (5)$$

In the above equations u , v , and w are the east-west, north-south, and vertical components of the wind, respectively, φ is the angle of the sloping terrain, ρ_m is the mean density of the fluid, α_m is the mean thermal expansion coefficient, and Γ is the lapse rate of temperature. All other variables have conventional definitions.

Before performing a scale analysis of the equations all variables are normalized as follows:

$$(u, v) = U(u^*, v^*) , \quad (6)$$

$$x = L(x^*) , \quad (7)$$

$$z = D(z^*) , \quad (8)$$

$$w = U \frac{D}{L} (w^*) , \quad (9)$$

$$t = f^{-1}(t^*) , \quad (10)$$

$$p = \rho_m f L U (p^*) , \quad (11)$$

$$\theta = f L U / g \alpha_m D (\theta^*) . \quad (12)$$

Here the starred variables are dimensionless. The time scale for this problem is f^{-1} ; in this time scale only inertial-gravity waves and diffusive transport processes of the boundary layer are important phenomena. Thus, the pressure perturbations are scaled considering quasi-geostrophic balance,

while the temperature perturbations are in hydrostatic balance with the pressure perturbations. It should be noted that this scaling of the perturbations is quite different from that appropriate for convective processes where the Coriolis force may be neglected and the appropriate time scale is N^{-1} (N is the Brunt-Väisälä frequency). Horizontal distance is scaled with the span of the terrain L , and vertical distance is scaled with the depth of the atmosphere. After substituting the expressions (6) - (12) into the governing equations the dimensionless equations become

$$\frac{\partial u}{\partial t} + R_o (\vec{V} \cdot \nabla u) - \cos \varphi v = - \frac{\partial p}{\partial x} - \frac{\sin \varphi}{\lambda} \theta + E (\lambda^2 \frac{\partial^2 u}{\partial x^2} + \frac{\partial^2 u}{\partial z^2}) , \quad (13)$$

$$\frac{\partial v}{\partial t} + R_o (\vec{V} \cdot \nabla v) + \cos \varphi u = E (\lambda^2 \frac{\partial^2 v}{\partial x^2} + \frac{\partial^2 v}{\partial z^2}) , \quad (14)$$

$$\lambda^2 \left[\frac{\partial w}{\partial t} + R_o (\vec{V} \cdot \nabla w) \right] = - \frac{\partial p}{\partial z} + \cos \varphi \theta + E \lambda^2 \left(\lambda^2 \frac{\partial^2 w}{\partial x^2} + \frac{\partial^2 w}{\partial z^2} \right) , \quad (15)$$

$$\frac{\partial \theta}{\partial t} + R_o (\vec{V} \cdot \nabla \theta) + S (- \sin \varphi u + \lambda \cos \varphi w) = E (\lambda^2 \frac{\partial^2 \theta}{\partial x^2} + \frac{\partial^2 \theta}{\partial z^2}) , \quad (16)$$

$$\frac{\partial u}{\partial x} + \frac{\partial w}{\partial z} = 0 . \quad (17)$$

Here, all the star superscripts are omitted and the variables are dimensionless. Several nondimensional parameters are defined as follows:

$$R_o = \frac{U}{fL} = \text{the Rossby number,}$$

$$\lambda = \frac{D}{L} = \text{the aspect ratio,}$$

$$E = \frac{v}{fD^2} = \text{the Ekman number, and}$$

$$S = \frac{\Gamma g \alpha_m D}{f^2 L} = \text{a measure of the static stability.}$$

For a special application of these equations to the central Great Plains, it is assumed that R_0 is of the order of magnitude of 10^{-1} , the aspect ratio λ is of the order of magnitude of 10^{-2} , the Ekman number is of the order of magnitude of 10^{-3} , and the static stability S is of the order of magnitude of 10^2 . It can be seen that as long as the slope of the terrain is of the order of magnitude ranging from 10^{-3} to 10^{-2} , the buoyant force parallel to the terrain becomes as important as the Coriolis and pressure gradient forces. Thus, it can be expected that characteristics of the PBL in the central Great Plains must be significantly different from those of the traditional stable and/or unstable baroclinic or barotropic planetary boundary layers.

Some Analytical Results

It is of interest to understand the physics of a buoyant-Ekman layer under the influence of diurnal heating and cooling of the underlying surface. Mathematically, this becomes an initial boundary value problem with a sixth-order partial differential equation. The transient part of the solution reveals interactions between four different kinds of oscillatory modes. These four modes are the inertial oscillation, the gravitational oscillation, and modes related to the diurnal

heating cycle and the diffusive transport rate. Finding an analytical solution for the transient part of the solution thus becomes extremely difficult, although not impossible. On the other hand it is possible to determine the solution corresponding to the forced oscillation; that is, the part of the oscillatory motion connected to the frequency of the forcing oscillation. But, physically, this may be somewhat misleading, since the solution for the forced oscillation is valid only after many cycles of the forcing oscillation, without varying other boundary conditions. In reality this seldom occurs. For simplicity only steady state solutions are pursued. This procedure may sacrifice information about the important inbetween processes, but it is helpful in understanding the trend of the physical processes. With the assumptions of steady state and an aspect ratio λ asymptotic to zero, and utilizing an expansion about the small parameter R_0 (the reason not to choose the Ekman number at this stage will be clear later), the set of equations is greatly simplified. Thus,

$$E \frac{\partial^2 u}{\partial z^2} - \frac{\sin\varphi}{\lambda} \theta - \frac{\partial p}{\partial x} + \cos\varphi v = 0 , \quad (18)$$

$$E \frac{\partial^2 v}{\partial z^2} - \cos\varphi u = 0 , \quad (19)$$

$$\frac{\partial p}{\partial z} - \cos\varphi \theta = 0 , \quad (20)$$

$$E \frac{\partial^2 \theta}{\partial z^2} - S(-\sin\varphi u + f \cos\varphi w) = 0 , \quad (21)$$

$$\frac{\partial u}{\partial x} + \frac{\partial w}{\partial z} = 0 . \quad (22)$$

Here the Ekman number E is much smaller than unity; however a straightforward omission of all the terms associated with the Ekman number reduces the order of the partial differential equations. Then, it is impossible to fit all the boundary conditions; e.g., the no-slip boundary conditions at the lower boundary surface. This situation leads to the singular perturbation problem which has been discussed by Cole (1968) and Greenspan (1968). The solution for this problem can be decomposed into two parts; an interior part which satisfies the equations as the Ekman number asymptotically approaches zero and a boundary part which satisfies the surface boundary conditions. Thus,

$$u = u^I + u^B , \quad (23)$$

$$v = v^I + v^B , \quad (24)$$

$$\theta = \theta^I + \theta^B , \quad (25)$$

$$p = p^I + p^B , \quad (26)$$

$$w = w^I + w^B , \quad (27)$$

where variables superscripted with I represent interior solutions and variables superscripted with B represent boundary layer solutions. All interior variables are asymptotically expanded in terms of the small parameter $E^{\frac{1}{2}}$ as follows:

$$u^I = u_0^I + E^{\frac{1}{2}} u_1^I + E u_2^I + \text{-----} , \quad (28)$$

$$v^I = v_O^I + E^{1/2} v_1^I + E v_2^I + \text{-----} , \quad (29)$$

$$\theta^I = \theta_O^I + E^{1/2} \theta_1^I + E \theta_2^I + \text{-----} , \quad (30)$$

$$p^I = p_O^I + E^{1/2} p_1^I + E p_2^I + \text{-----} , \quad (31)$$

$$w^I = w_O^I + E^{1/2} w_1^I + E w_2^I + \text{-----} . \quad (32)$$

By substituting the expanded interior solutions into (18) - (22), and grouping terms of the same order, one can obtain the zero-order equations:

$$\cos\varphi v_O^I = \frac{\partial p_O^I}{\partial x} + \frac{\sin\varphi}{\lambda} \theta_O^I , \quad (33)$$

$$u_O^I = 0 , \quad (34)$$

$$\frac{\partial p_O^I}{\partial z} = \cos\varphi \theta_O^I , \quad (35)$$

$$w_O^I = 0 . \quad (36)$$

Physically, the zero-order interior solutions represent a hydrostatic and geostrophic balance state; the horizontal wind is nondivergent. On the other hand, since the boundary layer solutions must satisfy the lower boundary conditions,

$$u = 0 = u^I + u^B$$

$$v = 0 = v^I + v^B$$

$$\theta = \theta_s = \theta^I + \theta^B$$

$$w = 0 = w^I + w^B$$

at $z = 0$,

where θ_s is the surface temperature. This requires that there must be a stretched z-coordinate such that terms associated with the Ekman number become order of unity. With the stretched coordinate $\eta = E^{-\frac{1}{2}} z$, the boundary layer equations become

$$\frac{\partial^2 u^B}{\partial \eta^2} - \frac{\sin \varphi}{\lambda} \theta^B - \frac{\partial p^B}{\partial x} + \cos \varphi v^B = 0, \quad (37)$$

$$\frac{\partial^2 v^B}{\partial \eta^2} - \cos \varphi u^B = 0, \quad (38)$$

$$\frac{\partial p^B}{\partial \eta} - E^{\frac{1}{2}} \cos \varphi \theta^B = 0, \quad (39)$$

$$\frac{\partial^2 \theta^B}{\partial \eta^2} - S(-\sin \varphi u^B + \lambda \cos \varphi w^B) = 0, \quad (40)$$

$$\frac{\partial u^B}{\partial x} + E^{-\frac{1}{2}} \frac{\partial w^B}{\partial \eta} = 0. \quad (41)$$

The boundary layer variables may be expanded as

$$u^B = u_0^B + E^{\frac{1}{2}} u_1^B + E u_2^B + \text{-----}, \quad (42)$$

$$v^B = v_0^B + E^{\frac{1}{2}} v_1^B + E v_2^B + \text{-----}, \quad (43)$$

$$w^B = w_0^B + E^{\frac{1}{2}} w_1^B + E w_2^B + \text{-----}, \quad (44)$$

$$p^B = p_0^B + E^{\frac{1}{2}} p_1^B + E p_2^B + \text{-----}, \quad (45)$$

$$\theta^B = \theta_0^B + E^{\frac{1}{2}} \theta_1^B + E \theta_2^B + \text{-----}. \quad (46)$$

The boundary layer zero-order equations then may be written

as

$$\frac{\partial^2 u_O^B}{\partial \eta^2} - \frac{\sin \varphi}{\lambda} \theta_O^B + \cos \varphi v_O^B = 0 , \quad (47)$$

$$\frac{\partial^2 v_O^B}{\partial \eta^2} - \cos \varphi u_O^B = 0 , \quad (48)$$

$$\frac{\partial p_O^B}{\partial \eta} = 0 , \quad (49)$$

$$\frac{\partial^2 \theta_O^B}{\partial \eta^2} + S \sin \varphi u_O^B = 0 , \quad (50)$$

$$\frac{\partial w_1^B}{\partial \eta} = - \frac{\partial u_O^B}{\partial x} . \quad (51)$$

The boundary conditions at $\eta = 0$ are given below:

$$u_O^B = - u_O^I = 0 , \quad v_O^B = - v_O^I , \quad \theta_O^B = \theta_s - \theta_O^I = \Delta T_s ,$$

$$w_1^B = w_O^B = 0 , \quad \text{and } p_O^B = 0 .$$

As $\eta \rightarrow \infty$ all the boundary layer variables should be bounded.

After elimination and manipulation of the zero-order equations, equations for u_O^B , v_O^B , and θ_O^B may be written as

$$\frac{\partial^4 u_O^B}{\partial \eta^4} + \mu^2 u_O^B = 0 , \quad (52)$$

$$\frac{\partial^6 v_O^B}{\partial \eta^6} + \mu^2 \frac{\partial^2 v_O^B}{\partial \eta^2} = 0 , \quad (53)$$

$$\frac{\partial^6 \theta_o^B}{\partial \eta^6} + \mu^2 \frac{\partial^2 \theta_o^B}{\partial \eta^2} = 0 . \quad (54)$$

Here,

$$\mu^2 = \cos^2 \varphi + \frac{\sin^2 \varphi}{\lambda} S . \quad (55)$$

The corresponding boundary conditions for u_o^B are:

$$\text{at } \eta = 0 , u_o^B = 0 , \frac{\partial^2 u_o^B}{\partial \eta^2} = \cos \varphi v_o^I + \frac{\sin \varphi}{\lambda} \Delta T_s ;$$

$$\text{as } \eta \rightarrow \infty , u_o^B \text{ and } \frac{\partial^2 u_o^B}{\partial \eta^2} \text{ are bounded.}$$

The boundary conditions for v_o^B are:

$$\text{at } \eta = 0 , v_o^B = -v_o^I , \frac{\partial^2 v_o^B}{\partial \eta^2} = 0 , \frac{\partial^4 v_o^B}{\partial \eta^4} = \cos^2 \varphi v_o^I + \frac{\sin \varphi \cos \varphi}{\lambda} \Delta T_s ;$$

$$\text{as } \eta \rightarrow \infty , v_o^B , \frac{\partial^2 v_o^B}{\partial \eta^2} , \text{ and } \frac{\partial^4 v_o^B}{\partial \eta^4} \text{ are bounded.}$$

The boundary conditions for θ_o^B are:

$$\text{at } \eta = 0 , \theta_o^B = \Delta T_s , \frac{\partial^2 \theta_o^B}{\partial \eta^2} = 0 , \text{ and } \frac{\partial^4 \theta_o^B}{\partial \eta^4} = -S \sin \varphi \left[\frac{\sin \varphi}{\lambda} \Delta T_s + \cos \varphi v_o^I \right] ;$$

$$\text{as } \eta \rightarrow \infty , \theta_o^B , \frac{\partial^2 \theta_o^B}{\partial \eta^2} , \text{ and } \frac{\partial^4 \theta_o^B}{\partial \eta^4} \text{ are bounded.}$$

Solutions of (52), (53), and (54) under the boundary conditions become

$$u_0^B = -\frac{1}{\mu} \left[\cos \varphi v_0^I + \frac{\sin \varphi}{\lambda} \Delta T_s \right] \exp\left[-\sqrt{\frac{\mu}{2}} \eta\right] \sin \sqrt{\frac{\mu}{2}} \eta, \quad (56)$$

$$v_0^B = -v_0^I + \frac{\cos \varphi}{\mu} \left[\cos \varphi v_0^I + \frac{\sin \varphi}{\lambda} \Delta T_s \right] (1 - e^{-\sqrt{\frac{\mu}{2}} \eta} \cos \sqrt{\frac{\mu}{2}} \eta), \quad (57)$$

$$\theta_0^B = \Delta T_s - \frac{S \sin \varphi}{\mu} \left[\cos \varphi v_0^I + \frac{\sin \varphi}{\lambda} \Delta T_s \right] (1 - \cos \sqrt{\frac{\mu}{2}} \eta e^{-\sqrt{\frac{\mu}{2}} \eta}). \quad (58)$$

The vertical velocity at the top of the boundary layer can be obtained by integrating (51); that is,

$$w_1^B(\eta \rightarrow \infty) = - \int_0^{\infty} \left(\frac{\partial u_0^B}{\partial x} \right) d\eta. \quad (59)$$

The solution may be written as

$$w_1^B(\eta \rightarrow \infty) = \sqrt{\frac{1}{2\mu^3}} \left(\cos \varphi \frac{\partial v_0^I}{\partial x} + \frac{\sin \varphi}{\lambda} \frac{\partial \Delta T_s}{\partial x} \right). \quad (60)$$

It should be noted that the vertical velocity induced by the boundary layer flow is $O(E^{\frac{1}{2}})$.

By utilizing the same procedure higher order solutions can be deduced. The higher order solutions apply to the physical processes of order $O(E^{\frac{1}{2}})$ and $O(E)$, etc. But these secondary and/or tertiary circulations have less physical significance. Consequently, only circulations of $O(E^0)$ and vertical motions of $O(E^{\frac{1}{2}})$ are pursued.

Physical Explanation and Application

Eqs. (56), (57), and (58) represent the velocity and

potential temperature fields of a buoyant-Ekman layer. In the limiting case as $\sin \varphi \rightarrow 0$ and $\cos \varphi \rightarrow 1$, the solutions represent the familiar Ekman boundary layer. It can be seen that in the limiting case the momentum field becomes decoupled from the thermal field. The vertical motion is induced only by frictional convergence or the Ekman-pumping effect. In contrast, for a heated buoyant-Ekman layer ($\Delta T_s > 0$) the cross-isobar flow u_O^B is increased by an additional buoyant force and for a cooled buoyant-Ekman layer ($\Delta T_s < 0$) the cross-isobar flow u_O^B is decreased by a negative buoyant force. From another point of view, the quantity $[\cos \varphi v_O^I + (\sin \varphi / \lambda) \Delta T_s] / \mu$ appearing in (56), (57), and (58) can be regarded as an equivalent geostrophic wind by comparison with the Ekman-spiral solutions. Thus, heating along a sloping terrain has the equivalent effect of increasing the geostrophic wind, and cooling along a sloping terrain acts to decrease the geostrophic wind.

By examining the temperature solution (58) for the buoyant-Ekman layer, it can be seen that as long as $\sin \varphi \neq 0$ the temperature profile shows a spiral shape. This is caused by the spiral cross-isothermal flow pattern of u_O^B . Veronis (1967) also has discussed the spiral temperature field of a pure buoyant boundary layer associated with a vertical wall within a rotating fluid.

It is useful to further examine the expression (60) for the vertical motion induced by the basic vorticity field $\partial v_O^I / \partial x$ and the differential heating $\partial \Delta T_s / \partial x$. First, if the surface heating is homogeneous, the vertical motion is controlled

by the basic vorticity field only. In the case of an uneven distribution of surface heating, the second term in (60) represents another mechanism which contributes to the vertical motion. An analog to the concept of Ekman pumping may be drawn; thus, the vertical motion field caused by an uneven distribution of surface heating may be called buoyant pumping. It may enhance or decrease the vertical motion induced by the vorticity field. A simple statement of the concept of Ekman and/or buoyant pumping is as follows. If the surface heating increases eastward across the axis of maximum vorticity of the southerly flow, the upward motion may be enhanced. On the other hand, if the surface heating decreases eastward across the axis of maximum vorticity, the upward motion may be reduced.

Finally, we wish to raise a question about whether the theory of the buoyant-Ekman layer is a rule rather than an exception for the central Great Plains planetary boundary layer. For the case of temperature perturbations on a gently sloping surface the lowest order boundary layer solution shows a coupling between the thermal and momentum fields. Specifically, the cross-isobar flow is significantly altered in this situation compared with the case of level terrain. The turbulent transport processes must be modified in this situation also. Thus, one needs to be cautious in the application of traditional PBL theories, which are based on the assumption of level terrain, to the sloping terrain case. Modification and assessment of traditional PBL theories for a general terrain situation is an important problem.

CHAPTER III

THE NUMERICAL MODEL AND THE EXPERIMENTS

The Formulation of the Model

From the results of the scale analysis in Chapter II, there are three small numbers associated with the governing equations; the Rossby number, the Ekman number and the aspect ratio. In the numerical experiment it is assumed that $\lambda \ll 1$. Then, the governing equations are reduced to the familiar set of equations under the hydrostatic approximation. The horizontal diffusion processes are also excluded by choosing $\lambda \ll 1$. This set of equations may be written as follows:

$$\frac{\partial \bar{u}}{\partial t} + \frac{\partial(\bar{u}\bar{u})}{\partial x} + \frac{\partial(\bar{u}\bar{w})}{\partial z} - f \cos \varphi \bar{v} = -C_p \bar{\theta} \frac{\partial \bar{\pi}}{\partial x} + g \sin \varphi + \frac{\partial(-\bar{u}'w')}{\partial z}, \quad (61)$$

$$\frac{\partial \bar{v}}{\partial t} + \frac{\partial(\bar{u}\bar{v})}{\partial x} + \frac{\partial(\bar{w}\bar{v})}{\partial z} + f \cos \varphi \bar{u} = \frac{\partial(-\bar{v}'w')}{\partial z}, \quad (62)$$

$$C_p \bar{\theta} \frac{\partial \bar{\pi}}{\partial z} = -g \cos \varphi, \quad (63)$$

$$\frac{\partial \bar{\theta}}{\partial t} + \frac{\partial(\bar{u}\bar{\theta})}{\partial x} + \frac{\partial(\bar{w}\bar{\theta})}{\partial z} = \frac{\partial}{\partial z}(-\bar{\theta}'w') + \left(\frac{d\bar{\theta}}{dt}\right)_{\text{RAD}}, \quad (64)$$

$$\frac{\partial \bar{u}}{\partial x} + \frac{\partial \bar{w}}{\partial z} = 0. \quad (65)$$

These are the momentum equations, the thermodynamic equation, and the continuity equation, respectively. The overbarred variables are the mean variables which can be resolved at the grid points of the numerical model. The primed variables are associated with the sub-grid scale turbulent diffusion processes and need to be parameterized in terms of the mean variables. The last term, $(d\theta/dt)_{\text{RAD}}$, in (64) denotes the effect of radiational cooling occurring in the nocturnal boundary layer. According to Elliott (1964), the radiational transfer mechanism plays a significant role in the total energy transfer of the nocturnal planetary boundary layer.

Parameterization of the Turbulent

Transport Processes

There are actually nine components of the Reynold stress tensor associated with the subgrid scale turbulent momentum flux. Three are neglected by the hydrostatic approximation. Another four components are neglected in each of the horizontal momentum equations because of the assumption that the dominant stress components are along the direction normal to the boundary surface. This is partially justified by the scale analysis in Chapter II; such terms as $\partial(\overline{u'^2})/\partial x$, $\partial(\overline{u'v'})/\partial x$, $\partial(\overline{u'v'})/\partial y$, and $\partial(\overline{v'^2})/\partial y$ are then omitted. Similarly, the horizontal diffusion terms in the thermodynamic equations are neglected.

In order to close the set of equations two major approaches have been utilized. One approach is analogous to laminar

flow theory where it is assumed that the stress tensor is proportional to the rate of strain. The proportionality constants also may be a function of the mean variables. This kind of approach is the so-called K-theory. Another method commonly used in closure theory is the higher order closure model (Deardorff, 1974). Instead of relating the turbulent stress terms directly to the rate of strain terms, a set of prognostic equations governing the time evolution of the subgrid scale turbulent eddy terms are formulated. Although the higher order closure model has a more sound physical basis, it seems impossible to adopt this kind of approach in the mesoscale boundary layer model in the foreseeable future because of the formidable time and storage requirements for the computational work. Thus, it is assumed that

$$-\overline{u'w'} \sim K_M \left(\frac{\partial \bar{u}}{\partial z} + \frac{\partial \bar{w}}{\partial x} \right) \sim K_M \frac{\partial \bar{u}}{\partial z} , \quad (66)$$

$$-\overline{v'w'} \sim K_M \left(\frac{\partial \bar{v}}{\partial z} + \frac{\partial \bar{w}}{\partial y} \right) \sim K_M \frac{\partial \bar{v}}{\partial z} , \quad (67)$$

$$-\overline{\theta'w'} \sim K_H \frac{\partial \bar{\theta}}{\partial z} , \quad (68)$$

In these expressions, K_M and K_H denote the turbulent exchange coefficients for momentum and heat, respectively. It is further assumed that the vertical shear of horizontal momentum is dominant in the rate of strain expression. The turbulent exchange coefficients K_M and K_H are functions of the mean state variables. They can be determined empirically or

semi-empirically. Before determining the functional form of K_M and K_H , it is worthwhile to first describe some properties of the planetary boundary layer. A basic assumption of this numerical experiment is that the subgrid scale transport processes of the PBL over the sloping surface are identical to those of a PBL over a flat surface.

The planetary boundary layer can be divided into two different regions. In the vicinity of the planetary surface the turbulent flux of momentum and heat remain nearly constant with height; this is the constant flux layer. The laws concerning the profiles of velocity and temperature within the constant flux layer are well understood for a wide range of conditions from observational measurements. In the upper part of the PBL the Coriolis force, the pressure gradient force, and the frictional force are the dominant forces. The velocity structure exhibits spiral properties and this layer is generally called the turning layer.

The PBL, except over oceanic areas is strongly affected by a diurnal cycle of heating and cooling of the underlying surface due to solar radiation; thus, the thermal stratification continuously changes due to this diurnal cycle. Because of the concept that atmospheric turbulence is driven by buoyant and/or velocity shear mechanisms, one can expect that the depth of the PBL will to some extent be a function of the surface heat flux. From numerical experiments (Deardorff, 1972a, 1974) and observational facts (Lenschow, 1973) the

depth of the unstable PBL is believed to be determined by the height of the temperature inversion. Turbulent activity is confined below this level. In contrast, the night-time PBL is confined to a shallow layer several hundreds of meters in depth (Uthe, 1972). This is because the Richardson number characteristic of the nocturnal PBL usually exceeds some critical value and then turbulent activity ceases in the upper portion of the boundary layer. With present knowledge of the PBL parameterization of the turbulent exchange coefficients, K_M and K_H , can be accomplished in the following way. First, the functional forms of K_M and K_H can be determined uniquely according to the profile laws of the constant flux layer. They can then be extrapolated upward into the turning layer, and boundary conditions may be imposed at the top of the planetary boundary layer.

According to Businger et al. (1971) velocity and potential temperature profiles for the surface constant flux layer can be expressed as:

$$\frac{\partial \bar{u}}{\partial z} = \frac{u_{*0}}{kz} \left[1 + 4.7 \frac{z}{L} \right] \quad \text{for } L > 0 , \quad (69.a)$$

$$\frac{\partial \bar{u}}{\partial z} = \frac{u_{*0}}{kz} \left[1 - 15 \frac{z}{L} \right]^{-\frac{1}{4}} \quad \text{for } L < 0 , \quad (69.b)$$

and

$$\frac{\partial \bar{\theta}}{\partial z} = \frac{\theta_*}{kz} \left[0.74 \left(1 - 9 \frac{z}{L} \right)^{-\frac{1}{2}} \right] \quad \text{for } L < 0 , \quad (70.a)$$

$$\frac{\partial \bar{\theta}}{\partial x} = \frac{\theta_*}{kz} \left[0.74 + 4.7 \frac{z}{L} \right] \quad \text{for } L > 0 . \quad (70.b)$$

In the above expressions L is the Monin-Obukhov length and is defined as

$$L = - \frac{u_{*0}^3}{k \frac{g}{\bar{T}} (\overline{w'\theta'})_0} , \quad (71)$$

where u_{*0} is the surface frictional velocity defined as

$$u_{*0} = \sqrt{\frac{|\vec{\tau}|}{\rho}} , \quad (72)$$

$\vec{\tau}$ is the surface frictional stress, $(\overline{w'\theta'})_0$ denotes the surface kinematic heat flux, and θ_* is the characteristic temperature defined as

$$\theta_* = - \frac{(\overline{w'\theta'})_0}{u_{*0}} . \quad (73)$$

Next, the distribution of K_M and K_H within the constant flux layer can be deduced from the definition of K_H and K_M and the profile relationships (69) and (70). These expressions are

$$K_M = k u_{*0} z \left(1 + 4.7 \frac{z}{L}\right)^{-1} \quad \text{for } L > 0 , \quad (74.a)$$

$$K_M = k u_{*0} z \left(1 - 15 \frac{z}{L}\right)^{\frac{1}{4}} \quad \text{for } L < 0 , \quad (74.b)$$

and

$$K_H = \frac{k u_{*0} z}{0.74} \left(1 - 9 \frac{z}{L}\right)^{\frac{1}{2}} \quad \text{for } L < 0 , \quad (75.a)$$

$$K_H = k u_{*0} z \left(0.74 + 4.7 \frac{z}{L}\right)^{-1} \quad \text{for } L > 0 . \quad (75.b)$$

From these expressions it can be seen that the ratio of K_H/K_M is equal to 1.35 for neutral stratification and becomes larger as the stratification becomes more unstable. This is the

major difference between the formulations for the constant flux layer by Businger et al. and KEYPS. The KEYPS formulation (Plate, 1971) assumes a constant ratio of K_H/K_M and is not consistent with observational studies.

Since the top of the unsteady planetary boundary layer is assumed to represent the upper limit of the nonzero turbulent eddy fluxes, a prognostic or a diagnostic equation for the PBL height serves as an important constraint on the vertical distribution of the turbulent exchange coefficients. Zilitin-kevich (1975) proposed a theory of the development of the unstable planetary boundary layer. He assumed that there are no moist convective processes within the PBL. Then the thermodynamic equation, with the assumption that advection contributes only a secondary effect compared to the vertical turbulent flux divergence, becomes

$$\frac{\partial \bar{\theta}}{\partial t} \approx \frac{\partial (-\overline{w'\theta'})}{\partial z} . \quad (76)$$

Integrating (76) from the surface to the time dependent height of the PBL $h(t)$, utilizing Leibnitz's rule, the expression becomes

$$\frac{\partial}{\partial t} \int_0^{h(t)} \bar{\theta} dz - \bar{\theta}(h) \frac{\partial h}{\partial t} = (\overline{w'\theta'})_0 . \quad (77)$$

From observations of a well-developed unstable PBL, the lapse rate of temperature is adiabatic except for a shallow super-adiabatic layer near the ground. So it can be assumed that the potential temperature profile is given by

$$\bar{\theta}(z) = \bar{\theta}(h) . \quad (78)$$

Then (77) becomes

$$h(t) \frac{\partial \bar{\theta}}{\partial t}(h, t) = (\overline{w' \theta'})_0, \quad (79)$$

with the boundary condition at the top of PBL, i.e.,

$$\frac{\partial \bar{\theta}}{\partial t}(h, t) = \left(\frac{\partial \bar{\theta}}{\partial z} \right)_{z=h} \left(\frac{\partial z}{\partial t} \right)_{z=h}. \quad (80)$$

The prognostic equation for the development of the unstable PBL may be written as

$$\frac{\partial h}{\partial t} \approx \frac{(\overline{w' \theta'})_0}{\left(\frac{\partial \bar{\theta}}{\partial z} \right)_{FA} h(t)}. \quad (81)$$

Here $(\partial \bar{\theta} / \partial z)_{FA}$ is the lapse rate of temperature in the free atmosphere. Eq. (81) is similar to the inversion rising model (Tennekes, 1973), except here entrainment and the strength of the temperature inversion are not taken into consideration. With such a coarse mesoscale PBL model, it is not expected that small-scale fluctuations of the temperature inversion can be resolved adequately.

The development of a stable planetary boundary layer is neither theoretically nor observationally well documented. Deardorff (1972b) inferred from a limited number of observations that the height of the stable PBL is

$$h(t) = \left(\frac{1}{30L} + \frac{f}{0.35 u_{*0}} \right)^{-1}. \quad (82)$$

But with this expression the predicted height of the PBL in the numerical model is too high to well simulate the development

of the low-level jet. So this expression is modified to be

$$h(t) = \left(\frac{1}{15L} + \frac{f}{0.15 u_{*0}} \right)^{-1}, \quad (83)$$

such that a shallower PBL is predicted with the same stability parameter L .

The distribution of K_M and K_H throughout the planetary boundary layer is determined by a method similar to that suggested by O'Brien (1970), except here a time dependent PBL height is used. In order to specify the hypothetical distribution of K_M and K_H , one needs to know the depth of the constant flux layer. Although there is no strict theory concerning the depth of the constant flux layer, it is safe to assume that the depth is less than a hundred meters. In this numerical experiment, the constant flux layer is assumed to be 25 m in depth and to be constant with time. According to O'Brien (1970), $K_M(z)$ can be determined if the values of $K_M(h)$, $K'_M(h)$, $K_M(h_c)$, and $K'_M(h_c)$ are known; a polynomial can be chosen to fit these values at the levels h_c and h , where h_c is the height of the constant flux layer and h is the time dependent PBL height which is predicted by (81) and (83). The prime superscript on K_M denotes a derivative with respect to z . The value of the turbulent exchange coefficient at the top of PBL is assumed to be equal to the value of the kinematic viscosity of the free atmosphere and is very small; the slope of K_M and K_H at the top of PBL is assumed to be zero, i.e., the value of K_M or K_H is constant above the PBL. A polynomial

which fits these requirements is

$$K_M(z) = K_M(h) + [(z - h)^2 / (\Delta z)^2] \times \{K_M(h_c) - K_M(h) + (z - h_c)[K'_M(h_c) + 2(K_M(h_c) - K_M(h))/\Delta z]\} . \quad (84)$$

In this expression $\Delta z = h - h_c$. The turbulent exchange coefficient for heat, $K_H(z)$, is determined in the same manner.

Eq. (84) is valid only above the constant flux layer. The distribution of K_M and K_H within the constant flux layer is determined according to (74) and (75). The distribution above and within the constant flux layer is matched at the top of the constant flux layer with zero and first order continuity.

Parameterization of Radiational Cooling

The radiative heat transfer in the PBL during unstable conditions is much smaller than the turbulent eddy transport; thus, it is not necessary to take this mechanism into account for the unstable case. However, the amount of sensible heat transferred by radiation is significant compared to that transported by eddy processes in a stable PBL. Thus, in this numerical experiment radiational cooling is taken into account only during stable conditions. Yamamoto et al. (1973) adopted a simple method to evaluate the effects of radiation cooling. As a first approximation, the cooling term is represented by means of Newtonian cooling referred to the surface temperature and is given by

$$\left(\frac{d\bar{\theta}}{dt}\right)_{\text{RAD}} = \delta \gamma_{\theta} (T - T_s) , \quad (85)$$

where

γ_{θ} = proportionality constant,
 T = temperature at level z ,
 T_s = surface temperature, and

$$\delta = \begin{cases} 1 & \text{if } T \geq T_s \\ 0 & \text{if } T < T_s . \end{cases}$$

Since

$$\frac{\partial T}{\partial z} \sim \frac{\partial \bar{\theta}}{\partial z} - \frac{g}{c_p} , \quad (86)$$

and

$$T(z) \sim \bar{\theta} - \frac{g}{c_p} z , \quad (87)$$

(85) can be simplified to

$$\left(\frac{d\bar{\theta}}{dt}\right)_{\text{RAD}} \sim \delta \gamma_{\theta} (\bar{\theta} - \bar{\theta}_s - \frac{g}{c_p} z) . \quad (88)$$

The constant γ_{θ} used in this experiment has a value ranging from 0.5×10^{-5} /sec to $3. \times 10^{-5}$ /sec.

The Finite-Difference Analog of the Governing Equations

The finite-difference scheme adopted in this numerical experiment is the leap-frog scheme, with centered time and space finite-difference analogs of the time and space derivatives. The finite-difference operators are first introduced as follows:

$$\delta_x \varphi = \frac{1}{\Delta x} [\varphi_{i+\frac{1}{2}} - \varphi_{i-\frac{1}{2}}] , \quad (89)$$

$$\bar{\varphi}^x = \frac{1}{2} [\varphi_{i+\frac{1}{2}} + \varphi_{i-\frac{1}{2}}] , \quad (90)$$

$$\delta_t \varphi = \frac{1}{\Delta t} [\varphi^{n+\frac{1}{2}} - \varphi^{n-\frac{1}{2}}] , \quad (91)$$

$$\bar{\varphi}^t = \frac{1}{2} [\varphi^{n+\frac{1}{2}} + \varphi^{n-\frac{1}{2}}] . \quad (92)$$

Since all variables in this numerical experiment are functions of two space coordinates (x, z) and time (t), $\varphi_{i,j}^n$ denotes the variable at ($i \Delta x, j \Delta z, n \Delta t$); i.e.,

$$\varphi_{i,j}^n = \varphi(i \Delta x, j \Delta z, n \Delta t) . \quad (93)$$

Hereafter, the superscripted and subscripted indexes are omitted and it is understood that the variable is for the grid point (i, j, n) if not otherwise indicated. By this symbolic convention it is clear that

$$\delta_x \bar{\varphi}^x = \overline{\delta_x \varphi^x} = \frac{1}{2\Delta x} [\varphi_{i+1} - \varphi_{i-1}] , \quad (94)$$

$$\delta_x \delta_x \varphi = \frac{1}{(\Delta x)^2} [\varphi_{i+1} - 2\varphi_i + \varphi_{i-1}] . \quad (95)$$

The finite-difference forms of the governing equations can be written as

$$\begin{aligned} \delta_t \bar{u}^t + \delta_x (\bar{u}^x \bar{u}^x) + \delta_z (\bar{u}^z \bar{w}^z) - f \cos \varphi v \\ = - c_p \theta \delta_x \bar{\pi}^x + g \sin \varphi + [\delta_z (K_M \delta_z u)]^{n-1} , \end{aligned} \quad (96)$$

$$\begin{aligned} \delta_t \bar{v}^t + \delta_x (\bar{u}^x \bar{u}^x) + \delta_z (\bar{w}^z \bar{v}^z) + f \cos \varphi u \\ = [\delta_z (K_M \delta_z v)]^{n-1} , \end{aligned} \quad (97)$$

$$c_p [\bar{\theta}^z \delta_z \pi]_{j+\frac{1}{2}} = -g \cos \varphi , \quad (98)$$

$$\delta_t \bar{\theta}^t + \delta_x (\bar{u}^x \bar{\theta}^x) + \delta_z (\bar{w}^z \bar{\theta}^z) = [\delta_z (K_H \delta_z \theta)]^{n-1} - \left(\frac{d\bar{\theta}}{dt} \right)_{\text{RAD}} , \quad (99)$$

and

$$\delta_x \bar{u}^x + \delta_z \bar{w}^z = 0 . \quad (100)$$

In the finite-difference equations the diffusion terms are evaluated at a time step lag.

Discussion of the computational stability of the proposed finite-difference equations can be divided into two parts; linear computational stability and nonlinear computational stability. It is assumed here that the system of finite-difference equations along with the initial and boundary conditions are well posed. During the last decade linear computational properties of various forms of meteorological equations have been thoroughly surveyed. So it is not necessary to provide a similar analysis and proof here. The papers by Ogura and Charney (1960), Fischer (1965), Williamson (1966), and the text by Haltiner (1971) cover various finite-difference approximations and their linear computational stability. The stability criterion for numerical integration of a simple advection equation utilizing the leap-frog scheme is $C \Delta t / \Delta x \leq 1$, where C is the maximum phase speed of waves allowed by the system of equations. For the numerical integration of a diffusion equation with a forward time and

centered space difference scheme, the stability criterion is $2 \nu \Delta t / (\Delta x)^2 \leq 1$. Here ν is the coefficient of diffusion. In conclusion, if a smaller value of Δt than required by any of these criteria is used in the time integration of the set of equations (96) - (100), linear computational stability is usually insured.

Phillips (1959) discussed the nonlinear computational instability arising from numerical integration of nonlinear advection or vorticity equations. This kind of instability cannot be eliminated by simply reducing the time step in the numerical calculations. Thus, the criterion for linear stability has nothing to do with nonlinear instability. According to Phillips, nonlinear instability arises from the nonlinear interaction between different wave modes; some wave modes may be created which are beyond the resolving limit of the finite grid domain. Thus, aliasing causes spurious growth of the amplitude of certain waves, especially those with a wavelength between two and four grid lengths. In his original paper Phillips suggested that nonlinear instability can be controlled by smoothing with a low-pass filter. However, a smoothing operator which is completely effective and simple is not available. In general, a smoothing operator may cause undesired damping of waves of low wave number in long range numerical integrations. Arakawa (1966) pointed out the importance of developing a scheme for conserving quadratic quantities. In the words of Arakawa,

"When quadratic quantities are conserved in a finite difference scheme, nonlinear computational instability cannot occur. This follows from the fact that if the square of a quantity is conserved with time when summed up over all the grid points in the domain, the quantity itself will be bounded, at every individual grid point, throughout the entire period of integration."

Thus, it seems appropriate to say that a sufficient condition to prevent nonlinear instability is to use a quadratic conservative scheme. The finite-difference scheme proposed for this numerical experiment does satisfy this requirement. Additional properties and proof are given in Appendix B.

For this numerical experiment the horizontal grid distance Δx is set equal to 5×10^4 m and the vertical grid distance Δz is chosen to be 200 m. A time step of 100 sec is satisfactory. The model employs 21 grid points in the horizontal direction and 22 grid points in the vertical direction for the numerical integration.

Initial and Boundary Conditions

Integration of the set of equations is started from a balanced state. In general the pressure field is balanced with the temperature field. Above the planetary boundary layer, the wind field is geostrophically balanced, and within the planetary boundary layer the Coriolis, pressure gradient, and frictional forces are in balance. These relations are expressed as follows:

$$\frac{\partial \bar{\pi}_I}{\partial z} = - \frac{g \cos \varphi}{c_p \bar{\theta}_I} , \quad (101)$$

$$\bar{v}_I = \frac{1}{f \cos \varphi} \left[c_p \bar{\theta}_I \frac{\partial \bar{\pi}_I}{\partial x} - g \sin \varphi - \frac{\partial}{\partial z} \left(K_H \frac{\partial \bar{u}_I}{\partial z} \right) \right], \quad (102)$$

$$\bar{u}_I = \frac{1}{f \cos \varphi} \left[\frac{\partial}{\partial z} \left(K_M \frac{\partial v_I}{\partial z} \right) \right]. \quad (103)$$

In the above expressions the subscript I indicates initial variables; the distribution of K_M is determined by the PBL parameterization; K_M has a value of zero above the PBL. The specific numerical values utilized in the initialization procedure are varied in different numerical experiments and will be summarized in the next chapter. The initialization is accomplished by specifying the lapse rate of temperature and then determining the pressure distribution. The wind field above the PBL is specified by setting $K_M = 0$ and then utilizing the geostrophic relation. Within the PBL the wind must be obtained by solving (102) and (103), iteratively. Because of the use of a three time-level leap-frog integration scheme, it is further assumed that all variables have a zero time tendency initially. This assumption avoids the use of a forward time integration scheme initially. Also it allows for better control of the unwanted gravity wave associated with the initialization, since the condition $\partial D / \partial t = 0$ is satisfied initially (D is the horizontal divergence $\partial \bar{u} / \partial x$).

The boundary conditions specified in any numerical experiment, in general, should be consistent with the physical conditions and also the order of the partial differential equation used in the integration. Mathematically, a first-

order partial differential equation needs one boundary condition, and a second-order equation needs two boundary conditions, and so on. In this numerical experiment, the governing equations for u , v , and θ are of first order in the horizontal direction and of second order in the vertical direction. But, with the centered space difference approximation, an additional boundary condition is required in the horizontal direction. Thus, the lower boundary conditions become

$$\left. \begin{aligned} \bar{u} = \bar{v} = \bar{w} &\equiv 0, \\ \bar{\theta} &= \theta_s(x, t) \end{aligned} \right\} \text{ at } z = 0. \quad (104)$$

Here θ_s is a prescribed function for the surface potential temperature. For a numerical study of the low-level jet, it also is of importance to understand the waves generated by the boundary layer mechanisms. From Appendix A, the possible wave solutions are inertial-gravity waves propagating in the east-west direction. Although the Doppler effect may affect the phase speed of the waves a little, the maximum phase speed calculated from (A.15) is about 50 m sec^{-1} . In order to avoid spurious reflection of the waves at both sides of the domain, an open boundary condition is applied to u , v , and θ at lateral and upper boundaries of the model. The details of this open boundary condition are discussed in Appendix C. The diagnostic equation for the pressure $\bar{\pi}$, i.e., the hydrostatic equation, is a first-order equation, so one boundary condition is needed to specify $\bar{\pi}$. Physically, one needs to specify $\bar{\pi}$ at the top of

the numerical model. It is desirable that this boundary condition only allow internal type gravity wave solutions, because external type gravity waves not only have less physical significance, but also are very fast-moving waves. This situation may cause an additional time requirement in the numerical calculations to insure computational stability. So, as discussed in Appendix A, $\bar{\pi}$ is specified as

$$\bar{\pi}(x,t,D) = \bar{\pi}_I(x,D) , \quad (105)$$

where D is the top of the numerical model and the subscript I indicates the initial value.

CHAPTER IV

RESULTS AND COMPARISONS

As have been pointed out in Chapter I, an examination of the development of the low-level jet can be divided into two categories: a description of the development of the low-level jet in one dimension (vertical profile) and a description of the development of the low-level jet as a two-dimensional (x - z) concentration of momentum. Although phenomena in these two categories are not mutually exclusive, only the development of two-dimensional low-level jet has physical significance as far as mesoscale circulations are concerned. From testing of the numerical model it is known that horizontal momentum can be dispersed because of the distribution of the surface heating. This point can be deduced from the theory of the buoyant-Ekman layer and will be discussed further later.

Numerical experiments with the two-dimensional model have been carried out to determine the importance of the sloping terrain and to study the response of the PBL to the surface temperature wave. In order to achieve this purpose, six different cases have been investigated with the numerical model. These cases are for different terrain slopes (slope

Table 1. Summary of parameters specified in the six numerical experiments. The height of the terrain increases westward. $V_g(x)$ shown in the table denotes the initial geostrophic wind. The latitude of the various experiments is denoted by φ . The diurnal surface temperature wave is denoted by ΔT_s , and B_1, B_2, B_3 are amplitudes of the three harmonics of the surface temperature wave. The unit for x within the expression for V_g is km. The unit of time (t) in the expression for ΔT_s is hr.

	Case I	Case II	Case III	Case IV	Case V	Case VI
Slope	0	1/600	1/600	1/600	1/600	1/600
$V_g(x)$	$A_1 = 15$ $A_2 = 0$	$A_1 = 15$ $A_2 = 0$	$A_1 = 15$ $A_2 = 0$	$A_1 = 15$ $A_2 = 5$	$A_1 = 15$ $A_2 = 5$	$A_1 = 15$ $A_2 = 5$
φ	35°	35°	35°	35°	35°	40°
ΔT_s	$B_1 = 6$ $B_2 = 1.5$ $B_3 = 1.0$	$B_1 = 6.0$ $B_2 = 1.5$ $B_3 = 1.0$	$B_1 = 8.0$ $B_2 = 1.5$ $B_3 = 1.0$	$B_1 = 6.0$ $B_2 = 1.5$ $B_3 = 1.0$	$B_1 = 8.0$ $B_2 = 1.5$ $B_3 = 1.0$	$B_1 = 8.0$ $B_2 = 1.5$ $B_3 = 1.0$

$$V_g(x) = A_1 \exp\left[-\left(\frac{x - 500}{400}\right)^2\right] + A_2 \exp\left[-\left(\frac{x - 500}{150}\right)^2\right]$$

$$\Delta T_s = B_1 \text{SIN}(15t - 140) + B_2 \text{SIN}(30t + 5) + B_3 \text{SIN}(45t + 45)$$

along east-west direction), different latitudes, different amplitudes of the diurnal surface temperature waves, and different initial horizontal geostrophic vorticity. Table 1 shows a summary of these cases. The horizontal pressure field for all of these experiments corresponds to southerly geostrophic flow. An example of the initialization for Case IV and Case V is shown in Fig. 2a and Fig. 2b. This initial state represents a slightly unstable boundary layer. The potential temperature lapse rate of the U.S. standard atmosphere ($3.26 \text{ }^\circ\text{K/km}$) is used to specify the initial potential temperature field above the planetary boundary layer. Within the PBL an adiabatic lapse rate is assumed except that a super-adiabatic lapse rate is specified in the constant flux layer. The initial field of the numerical integration is specified in such a manner to represent 10:00 a.m. local time. After the initialization the only driving force accounted for in the numerical model is that due to the diurnal variation of the surface temperature. The form of the surface temperature wave is specified by

$$\begin{aligned} \Delta T_s = & B_1 \times \sin(15 t - 140) + B_2 \times \sin(30 t + 5) \\ & + B_3 \times \sin(45 t + 45) , \end{aligned} \quad (106)$$

and is shown by Fig. 3. This expression was derived from a radiation-conduction boundary layer model by Kuo (1968). It simulates actual diurnal temperature variations very well. In this expression, t is time measured in hours. A slight

modification of the phase angle from Kuo's original form has been made in (106) such that the maximum surface temperature occurs at 1600 LST (LST is local standard time). The values of the constants B_1 , B_2 , and B_3 are given in Table 1. The time evolution from the numerical integration of Case IV is shown by a series of figures. Figs. 4a - 4o represent the horizontal momentum field. The solid lines in the figures represent the north-south component (v) of the horizontal wind and the dashed-lines represent the east-west component (u). Fig. 5 shows vertical profiles of potential temperature θ for the middle grid point of the numerical model. The arrow-marks shown in the figures indicate the height of the PBL predicted by the model. In general, from 0900 to 1800 LST the PBL is unstable with upward surface heat flux; during the remaining hours the planetary boundary layer is stable. The depth of the PBL increases during the period of upward surface heat flux. The maximum depth predicted by the model occurs at about 1800 LST. After this, the depth of the PBL decreases to a shallow layer because the turbulent eddies lose their support from the buoyant activity. The surface heat flux corresponding to the diurnal temperature wave is calculated by the model and is shown in Fig. 6. There is upward flux during daytime hours and downward flux at night time. But the horizontal distribution is uneven and depends on the wind speed (actually the bulk Richardson number of the surface layer). In order to clarify and illustrate the concept of the development of the

one-dimensional jet and of the two-dimensional jet, in the following paragraphs comparisons are discussed and physical explanations are offered.

One-D Low-level Jet

The one-D low-level jet which develops in the vertical profile of the horizontal wind has been observed and investigated by many authors. It is believed that the most significant mechanism which affects the diurnal variation of the low-level jet was proposed by Buajitti and Blackardar (1957). According to their theory the diurnal wind variations in the lower atmosphere are driven by the diurnal variation of the eddy exchange coefficient K_M . The vertical profile of the horizontal wind at the center of the grid in Case I (slope = 0) is shown in Figs. 7 and 8. The diurnal wind variation is about 4-5 m/sec at a height of 500 ~ 800 m above the surface. A unique feature of this experiment is the time dependent PBL height which is different from previous one-dimensional analytical or numerical models (Bonner et al., 1970; Krishna, 1968) where a constant PBL height has been specified. To illustrate the effect of the diurnal variation of PBL height, Fig. 9 shows the diurnal variation of PBL height at the center grid point. It can be seen that the PBL becomes very shallow after 1800 LST. Thus, the layer between about 0.4 ~ 1.5 km becomes fully unbalanced and the wind begins rotating in a clockwise sense. This can be further illustrated by Fig. 10 which shows the variation

of the boundary layer wind veering angle, α . The angle α denotes the angle between the wind velocity vector and the isobars. Positive values of α indicate cross isobar flow toward low pressure, and vice versa. The dramatic change of the PBL height after the beginning of surface cooling also has been simulated by Olanski et al. (1974) with a more sophisticated model. Hoxit (1973), by analyzing wind data for the southeast U.S. (over rather flat terrain), has described features similar to those predicted in this experiment. For purposes of comparison Figs. 11 and 12 are adopted from his results.

In order to reveal the importance of the sloping terrain as predicted by buoyant-Ekman layer theory, Case II is compared with Case I. Case II has all the same physical conditions as that of Case I, except sloping terrain is specified. Figs. 13 and 14 show the u- and v-components from this experiment at the same location as before. The terrain slope is 1/600 (terrain height increases westward). A significant increase of the amplitude of the diurnal wind variation is observed. The maximum development of the southerly jet in the vertical profile occurs between 2400 and 0200 LST. The wind hodographs at 625 m above the ground at the central grid point of the model are plotted in Fig. 15. The solid line represents the hodograph from the results of Case II, while the dash line represents the hodograph from the results of Case I. It clearly shows the relative amplitude for the cases with different slopes. The hodograph compared with the observed one (Bonner

et al., 1970) is realistic in both the amplitude and the phase relation, except that the hodograph from their observations is averaged so the cycle can be closed.

As has been pointed out in Chapter II the buoyant force has a component along the sloping terrain; this causes the so-called drainage wind. Thus, the drainage wind is up the slope when the surface is heated and down the slope when the surface is cooled. The relation between the drainage wind and the surface geostrophic wind is easily seen from the following expressions for the geostrophic wind:

$$V_g = \frac{\cos\varphi}{f} [c_p \theta \frac{\partial \pi}{\partial x} - g \sin\varphi] . \quad (107)$$

Eq. (107) for the geostrophic wind can be decomposed into two terms as shown below. The first term is the diurnally averaged geostrophic wind \bar{V}_g and the second is a perturbation which is related to the buoyant force along the sloping terrain. Thus,

$$V_g = \bar{V}_g + \frac{\cos\varphi}{f} \left(\frac{g}{\bar{\theta}} \theta' \sin\varphi \right) . \quad (108)$$

In this expression, $\bar{\theta}$ is the diurnally averaged potential temperature and θ' is the perturbation potential temperature associated with the surface temperature wave. Thus, part of the geostrophic wind over sloping terrain is associated with the large scale prevailing pressure distribution. Another part is associated with the buoyant force along the terrain slope and is induced by surface heating and cooling. This is actually equivalent to the concept of a drainage wind in the

direction of the terrain slope as suggested by Holton (1967).

Sangster (1967) and Bonner et al. (1970), by using the altimeter correction formula, have calculated the surface geostrophic wind over the Great Plains area. A large amplitude diurnal variation of the surface geostrophic wind was found by both investigators. Furthermore, Sangster (1967) had pointed out that the shape of the curve is quite similar to a normal temperature trace.

Values of surface V_g computed from the numerical experiments of Case I and Case II are plotted in Fig. 16. It can be seen from the figure that the diurnal variation of the surface V_g for the level terrain case is relatively small. But, because the result is from a two-dimensional model, the pressure gradient may be varied by the uneven distribution of surface heating and subsequent redistribution of the mass field. For the sloping terrain case the amplitude of the diurnal variation of the surface V_g is relatively large. The maximum variation is about 10 m/sec. Another interesting feature of this variation is that it takes a form similar to the variation of the surface temperature wave. So, the surface V_g is actually controlled by the surface temperature wave. These results are very similar to Sangster's averaged value of surface geostrophic wind for the month of June 1966 over the Great Plains area. From the numerical experiment it has been found that the amplitude of the diurnal variation of V_g decays rather rapidly with height. In order to gain physical insight

of the cause of the diurnal variation of the boundary layer wind, it is worthwhile to examine the phase relationship of the diurnal variation of u , v , and V_g as simulated by the model. In general, as the surface temperature increases due to radiational heating, the buoyant force has a component up the slope. Meanwhile the turbulent transport of momentum becomes more efficient; thus, the frictional force increases in this period. By these mechanisms, V_g increases during the development of the unstable PBL; v , the component parallel to the isobars decreases because of the increased retarding force and u increases because of the buoyant and retarding forces. After surface heating ceases the PBL is cooled by both turbulent diffusion and radiational cooling; so the buoyant force is directed downslope. During this period V_g decreases in magnitude and the magnitude of the cross isobar flow decreases (becomes less negative). Meanwhile, during the period of dramatic reduction of the frictional force in the stable PBL, v becomes increasingly larger. All the variation acts as an inertial rotation of the wind component in a clockwise sense. Indeed, this mechanism can be explained through a combination of the concepts of Buajitti et al. (1957) and Holton (1967). But, from this numerical experiment it is evident that the transport mechanism which causes the variation of the buoyant force is dominated by the turbulent diffusion process rather than by radiational heating or cooling, as suggested by Holton.

As has been mentioned before, the sloping terrain effect

tends to increase the amplitude of the diurnal wind variation. From further numerical experiments it has been found that the amplitude of the surface temperature wave also has a direct effect on the amplitude of the wind variation. As the amplitude of the temperature wave is increased, the diurnal wind variation becomes larger. This is shown in Fig. 17 and 18 as a comparison of the results from Case IV and Case V. It is apparent that a larger amplitude surface temperature wave may excite larger amplitude low-level wind variations.

The time of formation of the low-level jet has long been believed to depend on latitude only. This is probably because previous studies are all based on climatological data; so the phase relation of the surface temperature wave has been neglected. From other numerical experiments, not discussed here, it is known that the time of formation of the low-level jet can be shifted by changing the phase of the surface temperature wave. With a specific surface temperature wave, it is obvious that only the latitude can affect the time of the formation. This point has been investigated in depth by Krishna (1968). His results show that as the latitude increases above 30°N , the time of formation of the low-level jet shifts to before midnight. As the latitude is decreased lower than 30°N , the time of formation of the low-level jet shifts after midnight. This is also verified by these numerical experiments; Figs. 19 and 20 show the results for different latitudes. With a latitude increase from 35°N to 40°N , the time of formation of

the low-level jet is shifted 1-2 hours earlier. Thus, one must question the validity of the assumption of homogeneity along the north-south direction. With different times of formation of the low-level wind maximum, the β -plane effect should be taken into consideration. The different time of formation of the low-level jet along the y-direction may cause low-level divergent wind fields in this direction. However, this point cannot be investigated with this numerical model.

It is of interest to point out several properties of the one-dimensional low-level jet as simulated by this model. Since the conditions which favor the formation of this kind of low-level jet exist over almost all the continental area, this nocturnal phenomena is not uncommon. From the vertical profiles of the low-level jet, it can be observed that several inflection points exist. The most prominent inflection point is located at a level slightly above the nose of the jet. Further significance of these inflection points cannot be revealed by this numerical model. Lilly (1966) has studied the inflection point instability of a neutral Ekman layer. Recently, Wagner (1975) studied a very similar phenomenon; his study deals with the inflection point instability within the nocturnal inversion.

Two-Dimensional Low-level Jet

From the point of view of mesoscale interactions, the formation of the two-dimensional low-level jet has further physical significance. The mechanism which will be discussed

below probably is one of the most possible physical mechanisms which may be responsible for the low-level jet, especially for the nocturnal jet observed to the east of the Rockies (Wexler, 1961). There are several other types of low-level jet streams delineated by mesoscale observations. For example, Browning (1973) showed that several parallel jet cores often are observed in advance of cold fronts.

For the discussion of the 2-D low-level jet, results for Case IV are shown in Fig. 4a to Fig. 4o. As shown by the figures, in the beginning stages of the development of the unstable PBL, only a weak horizontal vorticity (shear) exists in the southerly wind. Because of the frictional effects of the PBL, a small cross-isobar flow exists and is up slope. As the development of the unstable PBL goes on, the depth of the boundary layer increases and the kinetic energy of the southerly component of flow becomes weaker. Meanwhile the cross-isobar flow shows more development. As shown by the numerical experiment, the cross-isobar flow is to some extent proportional to the strength of the basic southerly flow. The proportionality is enhanced by the development of the unstable PBL, because of the increasing magnitude of the retarding and buoyant forces. Then, through this boundary layer mechanism, an increase of low-level convergence is observed on the cyclonic-shear side of the southerly flow. Similarly, an increase of the low-level divergence is seen on the anti-cyclonic shear side of the southerly flow. This also can be seen in the vertical motion

field shown in Fig. 21. For a better explanation, the buoyant-Ekman layer theory is utilized. The calculated surface heat flux is shown in Fig. 6. From this figure it can be seen that the surface heat flux responds to the surface temperature wave unevenly.

Large surface heat flux is also associated with large wind speed. This is a unique feature of the turbulent boundary layer, since the turbulent flux is proportional to both the temperature stratification and the mechanical shear. The feedback effect of this uneven surface heat flux is clearly shown by Eq. (56) from the theory of buoyant-Ekman layer. Thus, a large cross-isobar flow is associated with a large surface heat flux. The enhancement of the low-level convergence and divergence is the natural result of the development of the unstable boundary layer over the sloping surface. This can happen over level terrain also; but, without the effect of buoyancy the development is comparatively weaker. The maximum development of the cross-isobar flow occurs two hours after the cessation of the surface heating as shown in the figure. This is because the effect of the decreasing surface friction is larger than that due to the reduction of the buoyant force at the initial stage of the development of the stable boundary layer. As the surface becomes further cooled, the low-level jet is forced. This can be seen in Fig. 4g and Fig. 4h which show the southerly flow at midnight and two hours after midnight. Vertical shear in the southerly flow not only increases

with time, but the horizontal shear also intensifies. From this numerical experiment the concentration of momentum within the x-z cross section is directly related to the horizontal distribution of the surface heat flux, although the existence of the physical mechanism associated with the formation of the one-D jet is a necessary condition, too. By the self-organization mechanism of the turbulent boundary layer, larger surface heat flux is induced at the initial location of higher wind speed, and thus larger cross-isobar flow develops. After the surface boundary layer becomes stable, the unbalanced cross-isobar flow, through the inertial oscillation, rotates in a clockwise sense to form the 2-D low-level jet. Thus, the strength of the southerly jet is actually related to the strength of the cross-isobar flow. This explains the concentration of the momentum. But, this self-organization mechanism can be altered by several possible mechanisms. For example, the large scale distribution of cloud may prevent this boundary layer self-organization mechanism because of differential solar insolation. So, when this self-organization mechanism of the turbulent boundary layer is not present the low-level jet cannot form.

During the period of formation of the low-level jet the ageostrophic component of wind rotates in a clockwise sense. Also, because of the horizontal inhomogeneity of the cross-isobar flow, gravitational oscillations are induced. The inertial wind oscillation is more pronounced at the 500 ~ 1500 m level.

It can be seen in Figs. 4a - 4o that the oscillation propagates eastward. The boundary induced vertical motion field at the 2000-m level is shown in Fig. 21. The mechanism which is responsible for the vertical motion field has already been discussed. The time series show upward motion on the cyclonic-shear side of the southerly flow and downward motion on the anti-cyclonic shear side. Both the upward and downward motion fields are enhanced during the development of the unstable PBL. The upward motion reaches its maximum at about 2000 LST; the maximum upward velocity is about 1.5 cm/sec. After 2000 LST a gravity wave is apparently excited and propagates eastward at a speed of about 15-20 m/sec. The gravity wave discussed in Appendix A is an inertial-gravity wave which is highly dispersive. This probably explains the broadening of the initial peak in the vertical velocity field. The vertical motions die out in the early morning hours when the surface becomes coldest. To explain this, one can again resort to the buoyant-Ekman layer theory. First, one should examine the surface heat flux as shown in Fig. 6. When the surface is cooled and a stable temperature stratification exists, the maximum downward heat flux occurs at the location of the highest wind speed. Thus, according to Eq. (60) for the vertical velocity predicted by the buoyant-Ekman theory, the Ekman pumping and buoyant pumping effects are out of phase and compensate each other. Thus, the vertical motion is reduced. With the same initial and boundary conditions as in Case IV, a larger amplitude of the diurnal

surface temperature wave has been imposed in Case V, as is shown in Table 1. The diurnal variation of the boundary layer wind in Case V is similar to that of Case IV except that the amplitudes are larger. The vertical motion field simulated by the model is shown in Fig. 22. Apparently, the amplitudes of the gravity waves are larger for Case V. Also, the maximum vertical velocity is about 2 cm/sec. From these results, it is clear that the low-level convergence and the formation of the low-level jet are phenomena which accompany each other as a consequence of the diurnal variation of the planetary boundary layer, especially in a boundary layer with sloping terrain. The low-level convergence field is continuously enhanced during the development of the unstable planetary boundary layer and during the initial stages of development of the stable boundary layer. The two-dimensional evolution of the southerly low-level jet simulated by the model may be compared with the observational results by Wexler (1961); the essential features are very similar.

The numerical experiment has been extended to further diurnal cycles. The important characteristics of the second cycle are similar to those of the first cycle except that the southerly flow has been reduced in strength. There are two possible mechanisms which may cause the reduction of the kinetic energy of the southerly flow. First, it could be due to a non-conservative numerical scheme. Secondly, it may be caused by the open boundary condition. The first mechanism

is unlikely, since a quasi-conservative scheme has been used. Thus, it is suspected that with the unrealistic terrain profile, an excess of energy has been dispersed through the open boundary by gravity waves. In the actual case, a very strong western blocking exists due to the Rockies. Thus, it may prevent in some degree the dispersion of kinetic energy by gravity waves. On the other hand, the existence of this western boundary may prevent the up-slope flow induced by the frictional and buoyant forces, and thus cause stronger low-level convergence fields compared with the simulated low-level convergence. Consequently, it is believed that the effects of the Rockies on the mesoscale circulation over the sloping terrain probably has been underestimated in the numerical experiments.

CHAPTER V

SUMMARY AND SUGGESTIONS

Summary

The planetary boundary flow over a large scale sloping surface is significantly modified because of coupling of the momentum and thermal fields. The buoyant-Ekman layer theory developed in Chapter II shows that the heated boundary may cause a buoyant force up the slope. Thus, this effect can significantly alter the cross-isobar flow which is initially controlled by the frictional force along. Applying this theory to the central Great Plains may reveal an important linkage between boundary layer flow and certain mesoscale circulations. The central Great Plains region is characterized by a slope of $1/1000 \sim 1/1400$ which increases westward. With this specific terrain, the structure of the southerly flow boundary layer is quite different from that of the northerly flow boundary layer. With the basic southerly geostrophic flow, the frictionally induced cross-isobar flow combines with the buoyant induced flow and the total cross-isobar flow is significantly increased during period of excess surface heating. By the same token, but with contrasting conditions, northerly flow has a smaller cross-isobar component. Thus, the cross-isobar

flow of the southerly wind depends on both the friction force and the local surface heating. The importance of surface differential heating and differential friction is clearly shown through this boundary layer process.

Contrary to the belief that a direct cause and effect relationship exists between the low-level jet and the low-level convergence field, the results show that both the vertical motion and the low-level jet are phenomena accompanying each other as an effect of the diurnal variation of the structure of the PBL, especially over sloping terrain. The time of occurrence of the maximum low-level convergence occurs prior to the time of maximum development of the low-level jet. According to the statistical averages determined by Wallace (1975), the time of maximum frequency of occurrence of thunderstorms in the summer, in central Oklahoma, Kansas and southern Nebraska, is around midnight. So results from these experiments may explain the correlation of the boundary layer phenomena and the nocturnal thunderstorms for this specific geographical region and time if one assumes that a time lag must exist between the maximum low-level convergence (2000 LST) and the mature stage of convective systems. Actually, the upward motion field persists for 8-10 hrs on the cyclonic shear side of the southerly flow; with an average upward velocity of about 0.5 cm/sec, a layer then can be lifted about 150 m. Although the process of release of potential instability is not included in the model, the boundary layer processes described by this model are believed to be important in the

release of instability at nighttime. The eastward propagation of the upward motion field at a speed of 15 ~ 20 m/sec probably has a close relationship with the motion of the convective system as suggested by Uccellini (1975).

Suggestions

Although this study has provided some persuasive results, several questions still remain unanswered. It is the author's opinion that the problems discussed below need to be studied further.

(a) The Western Blocking Effect on the Southerly Flow

The fact that southerly flow is blocked on the western side by the Rocky Mountains has caused some investigators to draw analogies with the Gulf Stream situation; but by no means are they similar phenomena. The density stratification is more important in the case of atmospheric flow. The ability of an air parcel to rise over an obstacle depends on the total energy of the air parcel and the stratification of the density field which may prevent upward motion of the air parcel. Thus, the development of the unstable boundary layer and the cross-isobar flow must be affected by this western boundary. In future study of boundary layer related phenomena such as the dry line or the low-level jet, the effect of western blocking needs to be carefully evaluated.

(b) The Terrain Effect on the PBL Structure and Transport Process

All the theories of the planetary boundary layer which have been developed are based on the assumption of a flat

terrain surface. But a large-scale sloping surface actually exists over a vast area of the continent. From the results of this study it has been shown that the terrain induces a significant effect on the cross-isobar flow. Thus, it is expected that use of traditional boundary layer resistance laws (Melgarejo and Deardorff, 1974; Zilitinkevich, 1975) must cause erroneous predictions of the boundary layer veering angle and of surface fluxes. A wide scattering of values of constants of the boundary layer resistance laws determined from observations has been obtained. Arya (1975) pointed out that the scattering may be caused by neglect of the thermal wind effect. It is the author's opinion that the variety of terrain slopes at different observational sites may be another factor contributing to this scatter. The basic structure and the transport processes of a sloping-terrain PBL need to be further studied, both theoretically and observationally.

(c) The β -Plane Effect

Even with the assumption of homogeneous terrain along the north-south direction, the time of formation of the nocturnal jet depends on latitude. Thus, with different times of formation of the low-level wind maximum, the low-level wind convergence varies along the north-south direction. From this point of view, the internal gravity waves associated with the nocturnal jet actually are a three-dimensional phenomena. Uccellini (1975), in a case study of the relationship of gravity waves and convective systems, has traced the gravity waves

which originate in the Texas-Oklahoma area and propagate in the northeast direction. Further study of the low-level jet with a three-dimensional model probably would provide needed information about the relationship of these phenomena.

REFERENCES

- Arakawa, A., 1966: Computational design for long-term numerical integration of equations of fluid motion: Two-dimensional incompressible flow. Part 1. J. Comput. Phys., 1, 119-143.
- Arya, S. P. S., J. C. Wyngaard, 1975: Effect of baroclinicity on wind profiles and the geostrophic drag law for the convective planetary boundary layer. J. Atmos. Sci., 32, 767-778.
- Bonner, W. D., 1968: Climatology of the low level jet. Mon. Wea. Rev., 96, No. 12, 833-850.
- _____ and J. Paegle, 1970: Diurnal variations in boundary layer winds over the south-central United States in summer. Mon. Wea. Rev., 98, 735-744.
- Browning, K. A. and C. W. Pardoe, 1973: Structure of the low-level jet streams ahead of mid-latitude cold fronts. Quart. J. R. Meteor. Soc., 99, 619-638.
- Buajitti, K. and A. K. Blackadar, 1957: Theoretical studies of diurnal wind structure variations in the planetary boundary layer. Quart. J. R. Meteor. Soc., 83, 486-500.
- Businger, J. A., J. C. Wyngaard, Y. Izumi and E. F. Bradley, 1971: Flux profile relationships in the atmospheric surface layer. J. Atmos. Sci., 28, 181-189.
- Cole, J. D., 1968: Perturbation Methods in Applied Mathematics. Ginn (Blaisdell), Waltham, Massachusetts.
- Deardorff, J. W., 1972a: Numerical investigation of neutral and unstable planetary boundary layers. J. Atmos. Sci., 29, 91-115.
- _____, 1972b: Parameterization of the planetary boundary layer for use in general circulation models. Mon. Wea. Rev., 100, 93-106.
- _____, 1974: Three-dimensional numerical study of the height and mean structure of a heated planetary boundary layer. Boundary-layer Meteorology, 7, 81-106.
- Elliott, W. W., 1964: The height variation of vertical heat flux from the ground. Quart. J. R. Meteor. Soc., 90, 260-265.

- Fischer, G. O., 1965: A survey of finite-difference approximations to the primitive equations. Mon. Wea. Rev., 93, 1-10.
- Greenspan, H. P., 1968: The Theory of Rotating Fluids. Cambridge Univ. Press, London.
- Haltiner, G. J., 1971: Numerical Weather Prediction. John Wiley and Sons, New York.
- Hoecker, W. H., 1963: Three southerly low-level jet system delineated by the Weather Bureau special pibal network of 1961. Mon. Wea. Rev., 91, 573-582.
- Holton, J. R., 1967: The diurnal boundary layer wind oscillation above sloping terrain. Tellus, 19, 2, 199-205.
- _____, 1972: An Introduction to Dynamic Meteorology. Academic Press, New York.
- Hoxit, L. R., 1973: Variability of planetary boundary layer winds. Dept. of Atmos. Sci., Colo. State Univ., 157 pp.
- Hseuh, Y., 1968: A buoyant Ekman layer. Geophysical Fluid Dynamics Institute, Florida State Univ., 15 pp.
- Krishna, K., 1968: A numerical study of the diurnal variation of meteorological parameters in the planetary boundary layer: I. Diurnal variation of winds. Mon. Wea. Rev., 96, 269-276.
- Kuo, H. L., 1968: The thermal interaction between the atmosphere and the earth and propagation of diurnal temperature wave. J. Atmos. Sci., 25, 682-706.
- Lenschow, D. H., 1973: Two examples of planetary boundary layer modification over the great lakes. J. Atmos. Sci., 30, 568-581.
- Lilly, D. K., 1965: On the computational stability of numerical solutions of time-dependent non-linear geophysical fluid dynamics problem. Mon. Wea. Rev., 93, 11-26.
- _____, 1966: On the instability of Ekman boundary flow, J. Atmos. Sci., 23, 481-489.
- Melgarejo, J. W. and J. W. Deardorff, 1974: Stability functions for the boundary-layer resistance laws based upon observed boundary-layer heights. J. Atmos. Sci., 31, 1324-1333.

- Nitta, T., 1962: The outflow boundary condition in numerical time integration of advective equations. J. Meteor. Soc. Japan, 40, 13-24.
- O'Brien, J. J., 1970: A note on the vertical structure of the eddy exchange coefficient in the planetary boundary layer. J. Atmos. Sci., 27, 1213-1215.
- Ogura, J. and J. G. Charney, 1960: A numerical model of thermal convection in the atmosphere. Proc. Internat. Symposium on Numerical Weather Prediction, Meteor. Soc. Japan, Tokyo, 431-452.
- Orlanski, I., B. B. Ross and L. J. Polinsky, 1974: Diurnal variation of the planetary boundary layer in a meso-scale model. J. Atmos. Sci., 31, 965-989.
- Pearson, R. A., 1974: Consistent boundary conditions for numerical models of systems that admit dispersive waves. J. Atmos. Sci., 31, 1481-1489.
- Phillips, N. A., 1959: An example of non-linear computational instability. The Atmosphere and the Sea in Motion. Rockefeller Ins. Press, New York, 509 pp.
- Pitchford, K. L. and J. London, 1962: The low-level jet as related to nocturnal thunderstorms over Midwest United States. J. Appl. Meteor., 1, 43-47.
- Plate, E. J., 1971: Aerodynamic Characteristics of Atmospheric Boundary Layer. AEC Critical Review Series, U.S. Atomic Energy Commission.
- Sanders, F., 1955: An investigation of the structure and dynamics of an intense surface frontal zone. J. Meteor. Sci., 12, 542-552.
- Sangster, W. E., 1967: Diurnal surface geostrophic wind variations over the great plains. Proceedings of the Fifth Conference on Severe Local Storms, St. Louis, Missouri, American Meteor. Soc., Greater St. Louis Chapter, Mo., 146-153.
- Shapiro, M. A. and J. J. O'Brien, 1970: Boundary conditions for fine mesh limited area forecasts. J. Appl. Meteor., 9, 345-349.
- Spiegel, E. A. and G. Veronis, 1960: On the Boussinesq approximation for a compressible fluid. Astrophysical J., 131, 442-447.

- Tennekes, H., 1973: A model for the dynamics of the inversion above a convective boundary layer. J. Atmos. Sci., 30, 558-567.
- Tepper, M., 1955: On the generation of pressure-jump lines by impulsive addition of momentum to simple current system. J. Meteor., 12, 287-297.
- Uccellini, L. W., 1975: A case study of apparent gravity wave initiation of severe convective storms. Mon. Wea. Rev., 103, 497-513.
- Uthe, E. E., 1972: Lidar observation of the urban aerosol structure. Bull. AMS, 53, 358-360.
- Veronis, G., 1967: Analogous behavior of rotating and stratified fluids. Tellus, 19, 620-633.
- Wagner, K. K., 1975: Inflection point instability within an inversion layer. Atmos. Res. Lab., Office of Res. Administration, University of Oklahoma.
- Wallace, J. M., 1975: Diurnal variation in precipitation and thunderstorm frequency over the conterminous United States. Mon. Wea. Rev., 103, 406-419.
- Wexler, H., 1961: A boundary layer interpretation of the low-level jet. Tellus, 13, 368-378.
- Williamson, D., 1966: Stability of difference approximations to certain partial differential equations of fluid dynamics. J. Comp. Phys., 1, 51-67.
- Yamamoto, G., A. Shimanuki, M. Aida and N. Yasuda, 1973: Diurnal variation of wind and temperature fields in the Ekman layer. J. Meteor. Soc. Japan., 51, 377-387.
- Zilitinkevich, S. S., 1975: Resistance laws and prediction equations for the depth of the planetary boundary layer. J. Atmos. Sci., 32, 741-752.

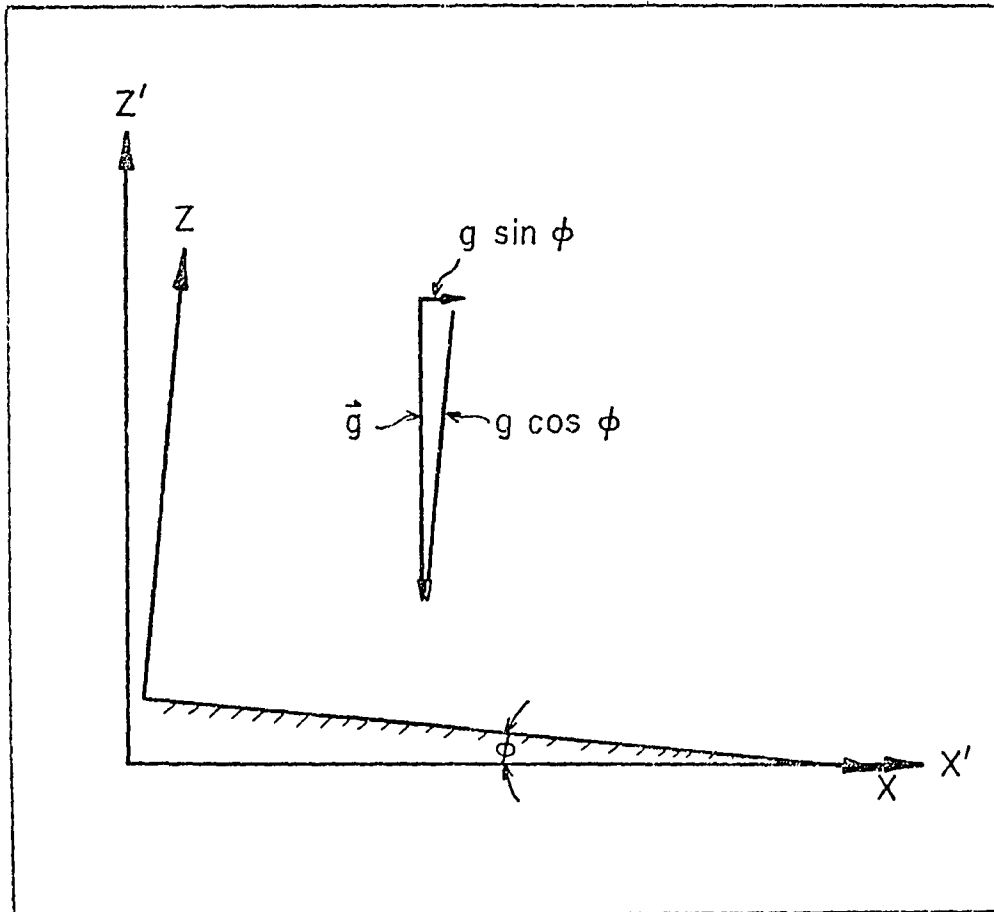


Fig. 1. The sloping terrain coordinate system; the gravitational force has a component $g \sin \phi$ along the terrain.

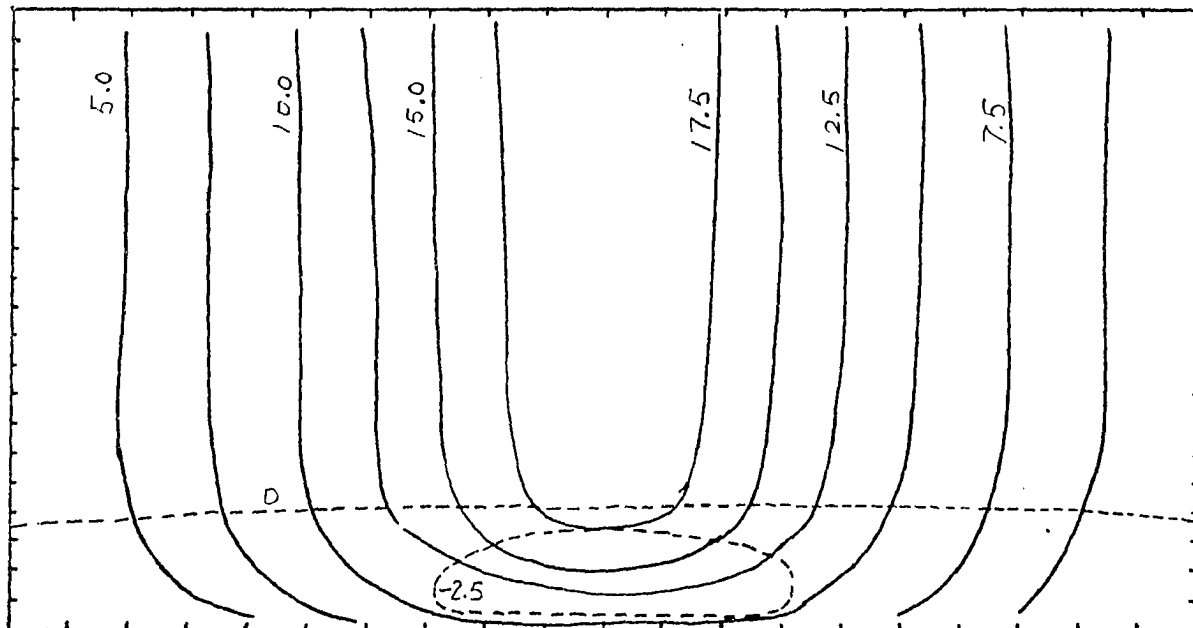


Fig. 2a. Initial (1000 LST) u-, v-field for the numerical experiments, Case IV and Case V. Solid lines in the figure denote the y-component of wind; dashed lines in the figure denote the x-component of wind. The isotachs are constructed at intervals of 2.5 m/sec.

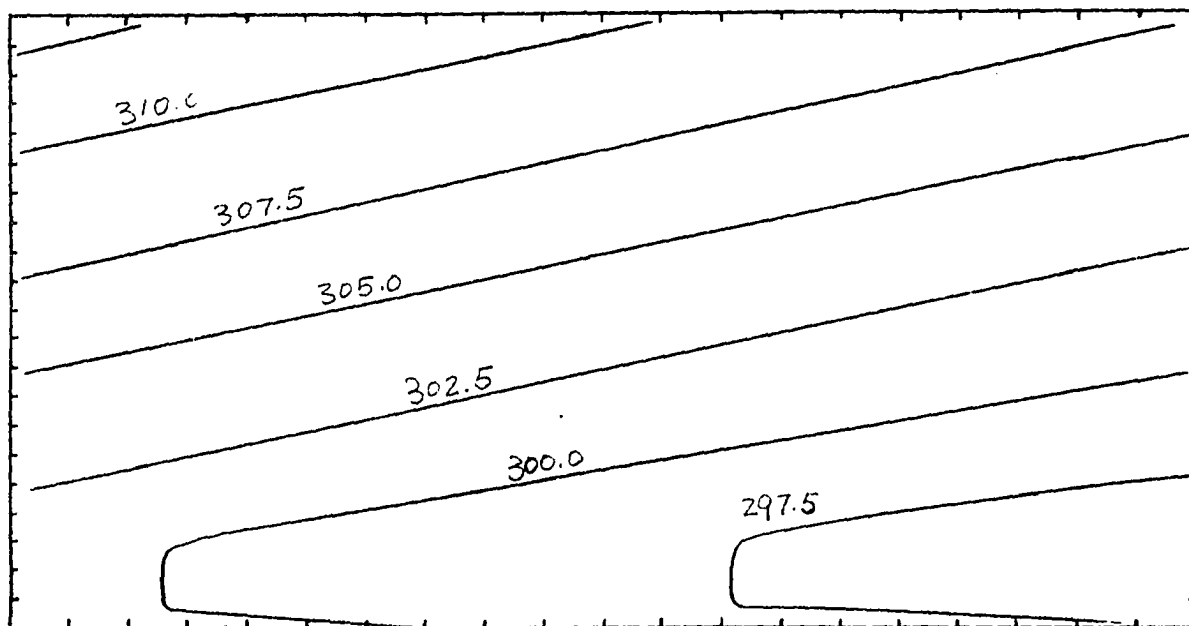


Fig. 2b. The initial field of potential temperature for the numerical experiments, Case IV and Case V. Isotherms are constructed at intervals of 2.5 K.

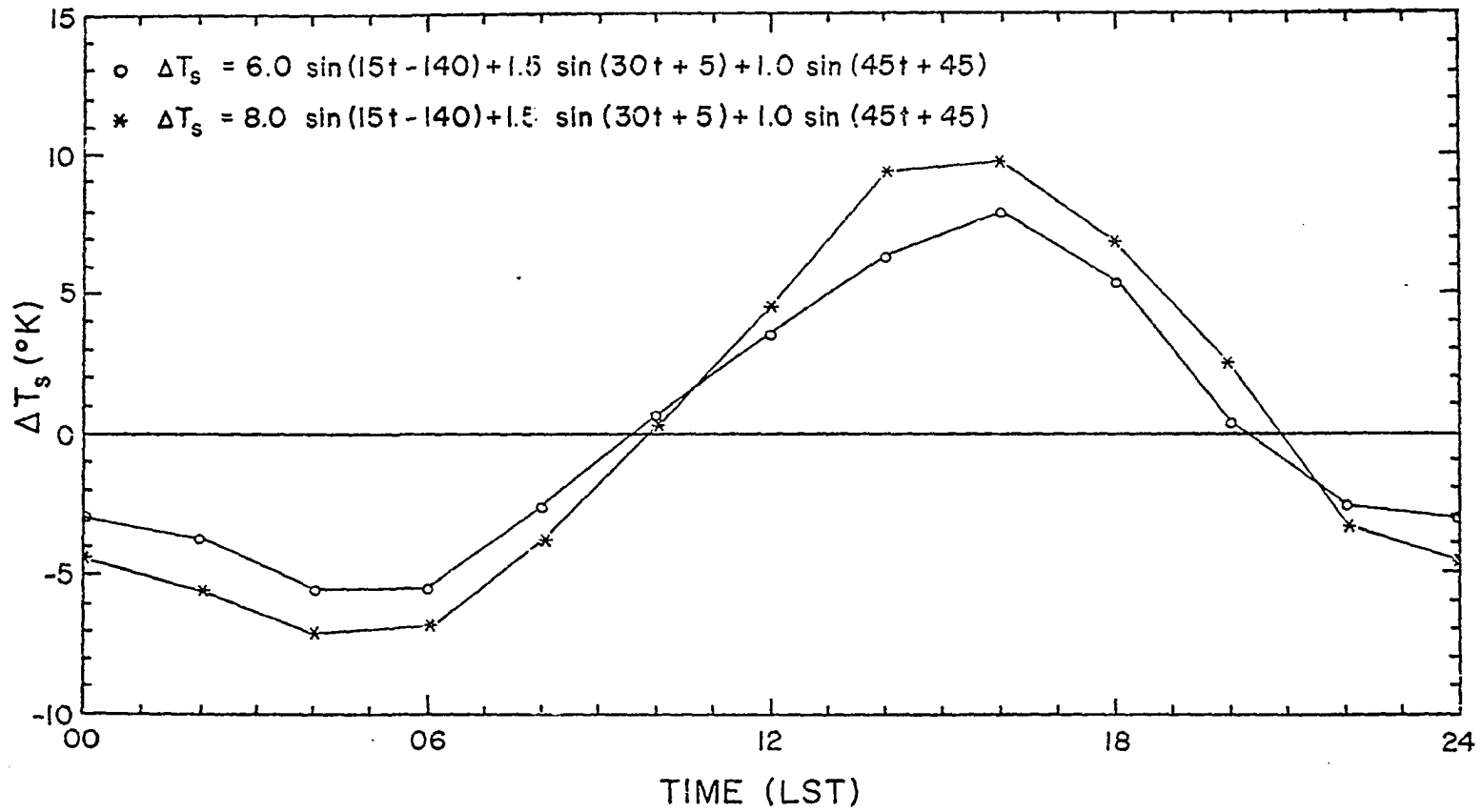


Fig. 3. The two diurnal surface temperature waves used in the numerical experiments. For details, see Table 1 and the text.

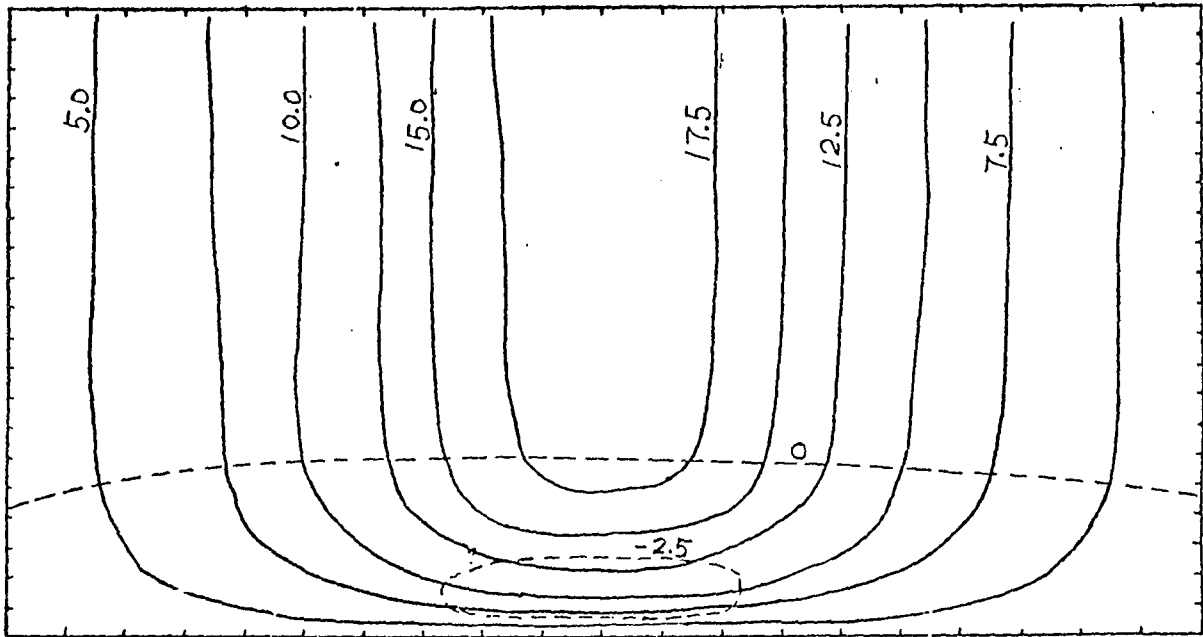


Fig. 4a. Wind field at 1200 LST for Case IV. Dashed lines are isotachs for the x-component of the wind; solid lines are isotachs for the y-component of the wind. Isotachs are drawn at intervals of 2.5 m/sec.

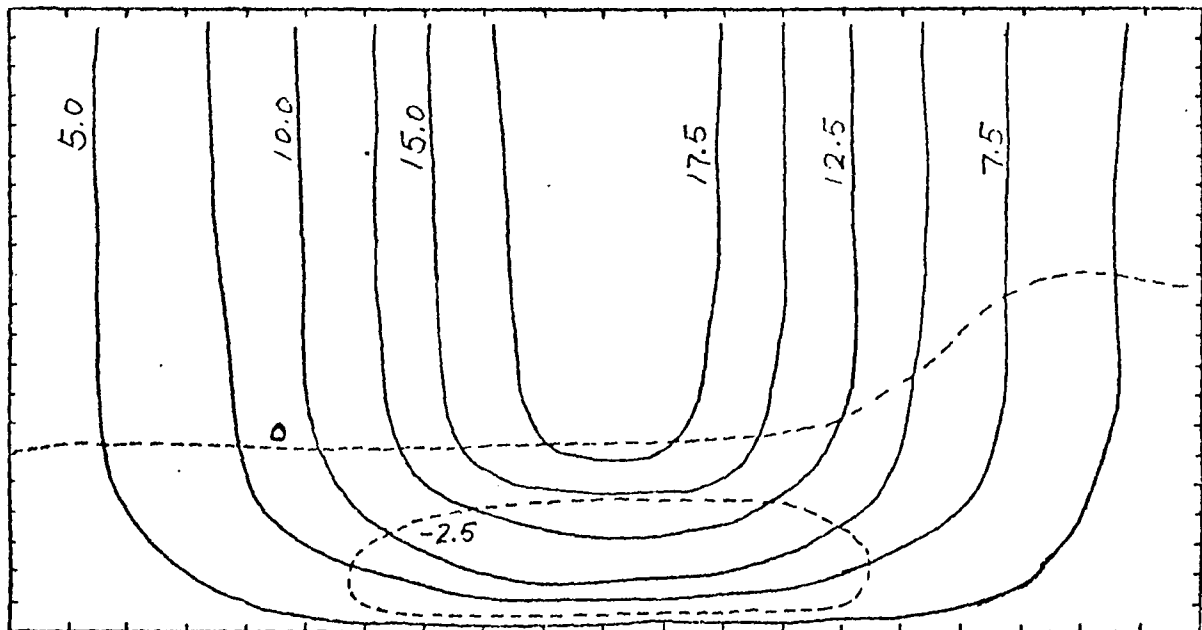


Fig. 4b. Same as Fig. 4a., except for 1400 LST.

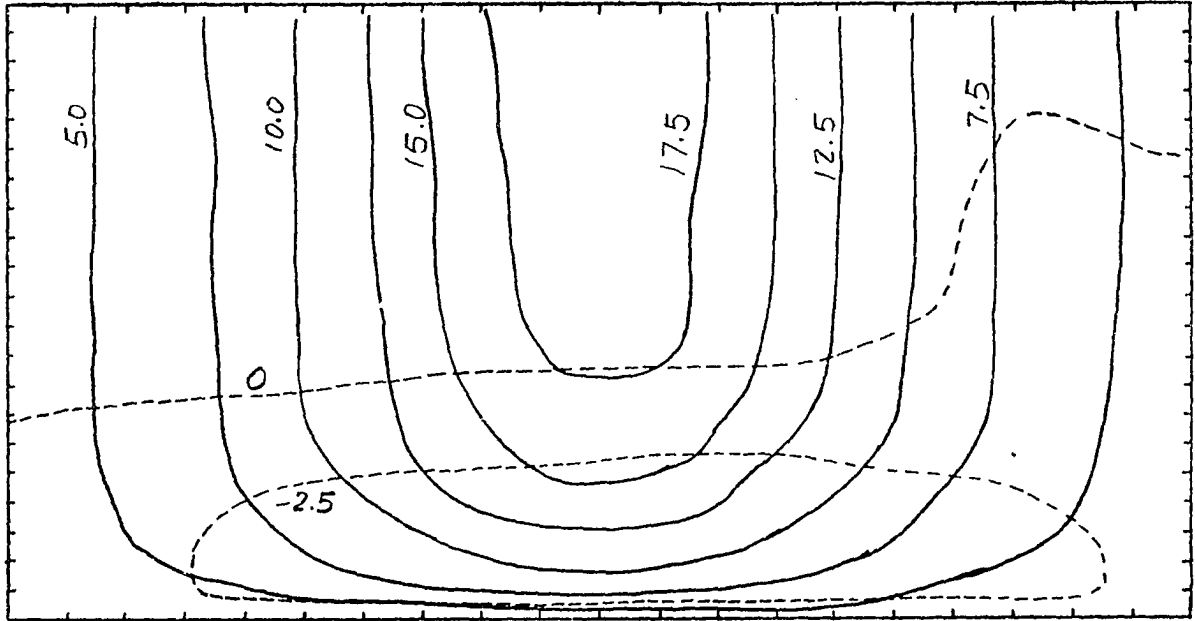


Fig. 4c. Same as Fig. 4a., except for 1600 LST.

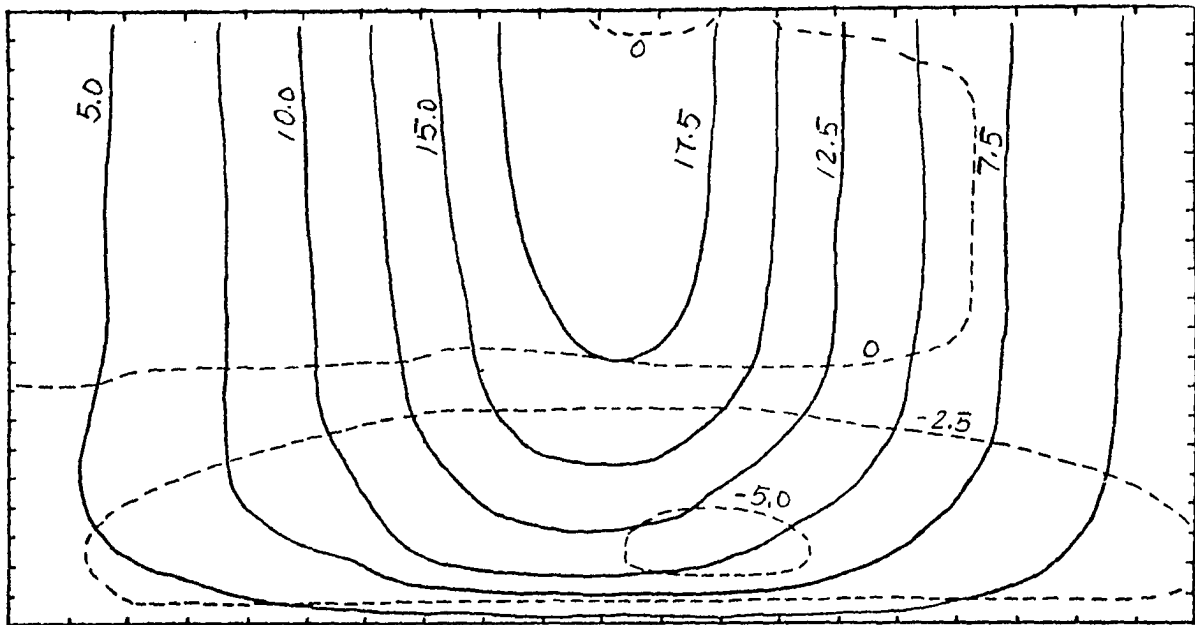


Fig. 4d. Same as Fig. 4a., except for 1800 LST.

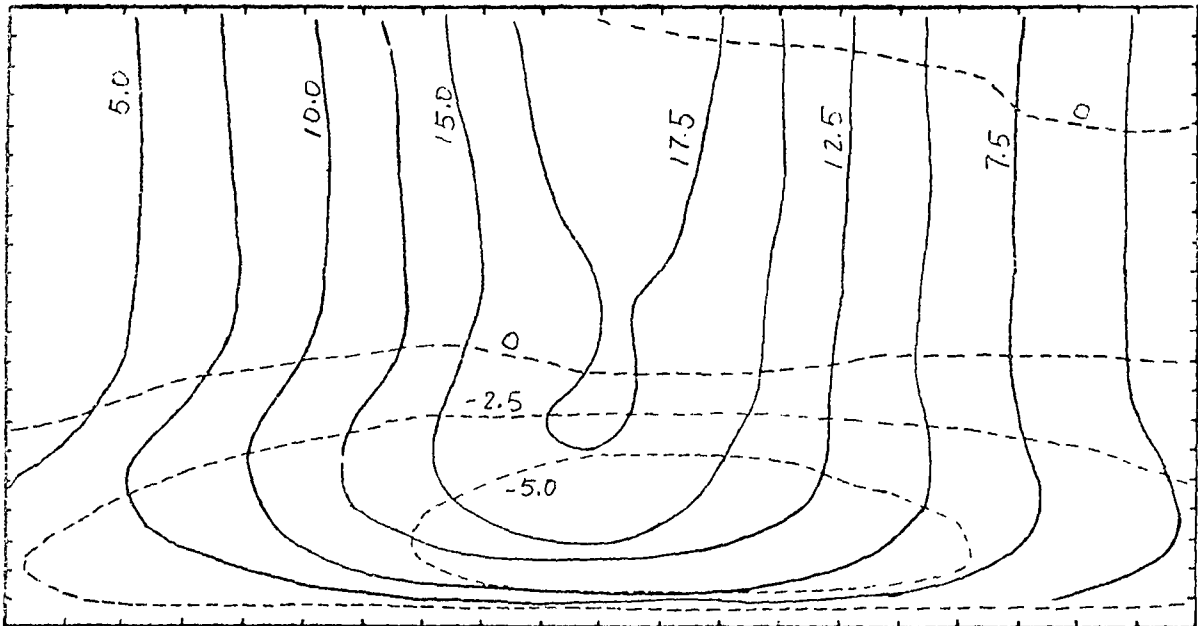


Fig. 4e. Same as Fig. 4a., except for 2000 LST.

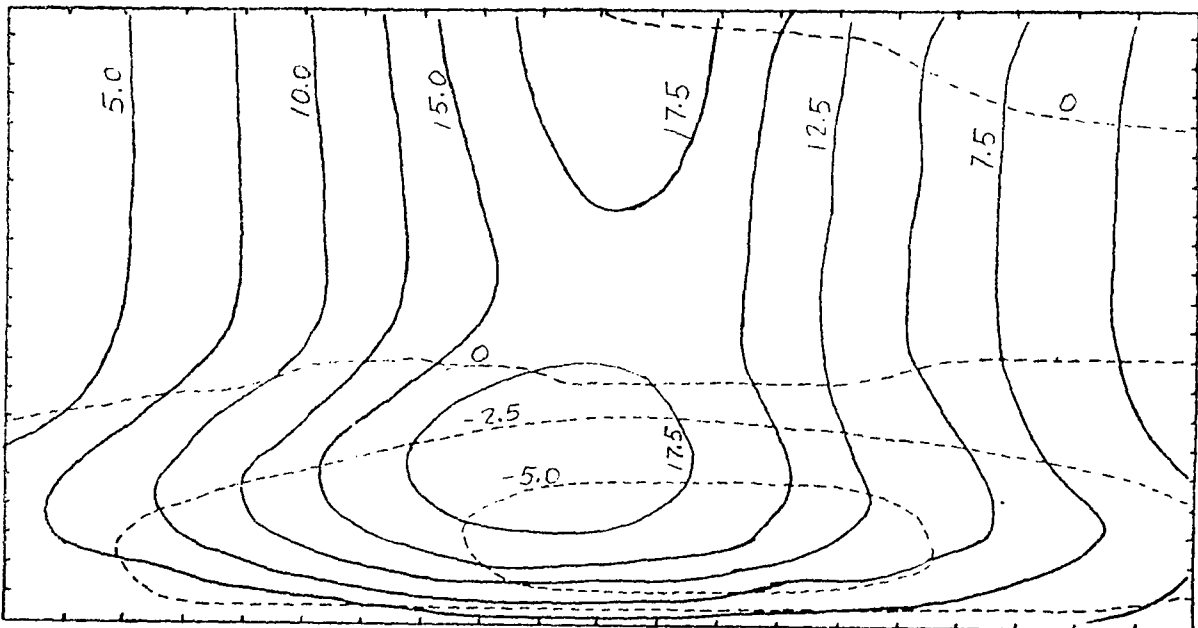


Fig. 4f. Same as Fig. 4a., except for 2200 LST.

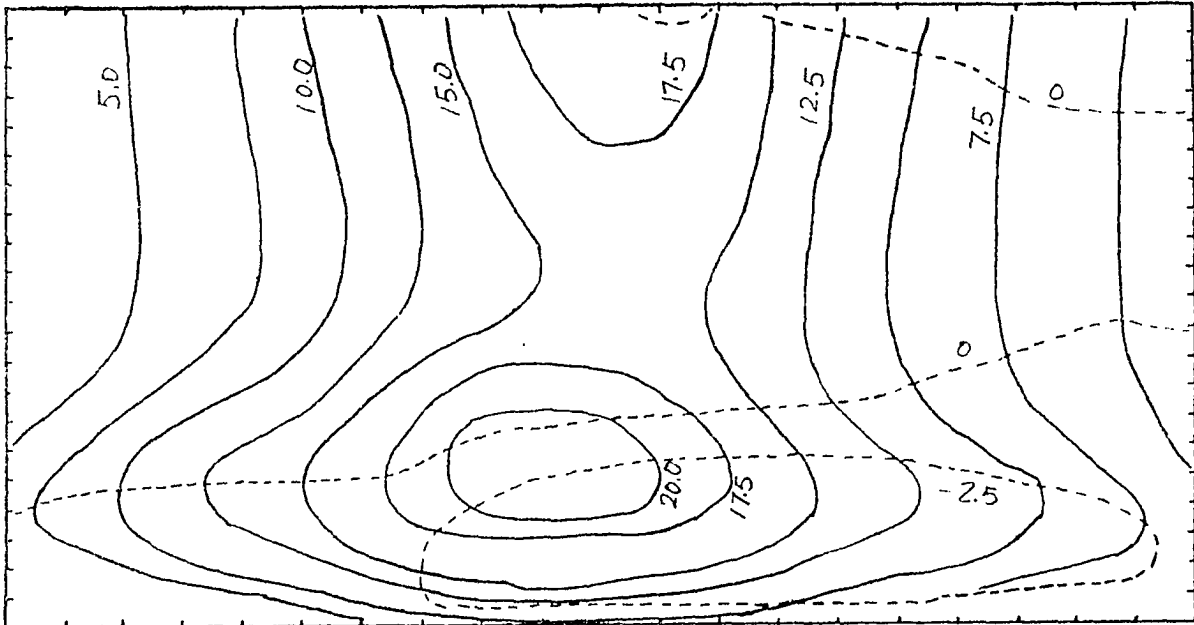


Fig. 4g. Same as Fig. 4a., except for 2400 LST.

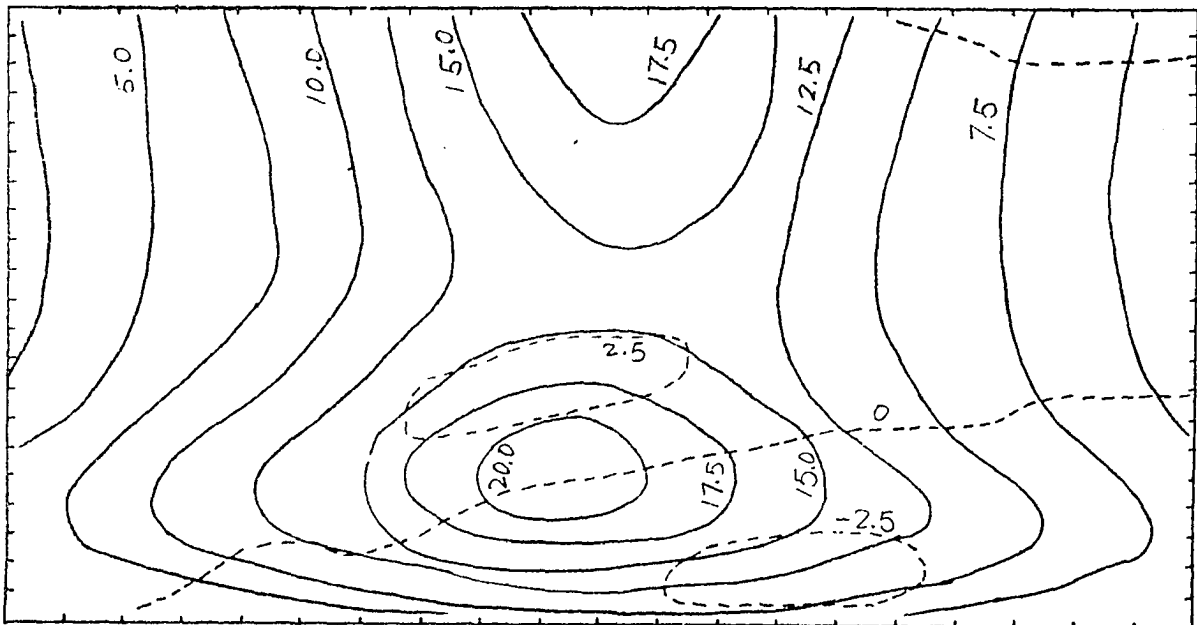


Fig. 4h. Same as Fig. 4a., except for 0200 LST on the second day.

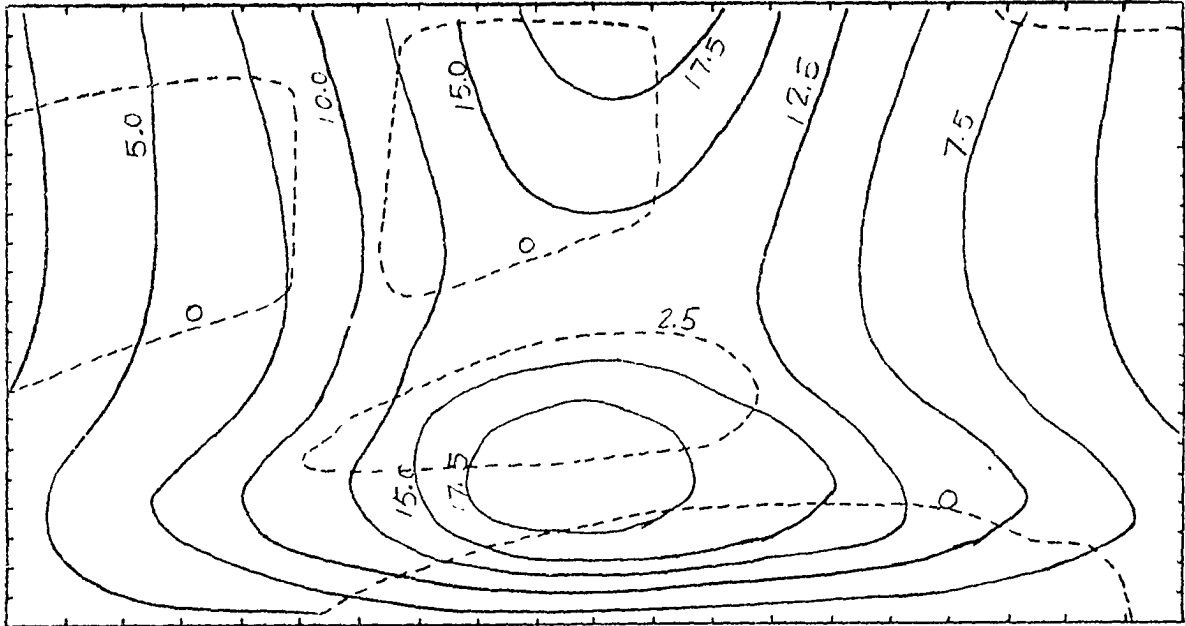


Fig. 4i. Same as Fig. 4a., except for 0400 LST on the second day.

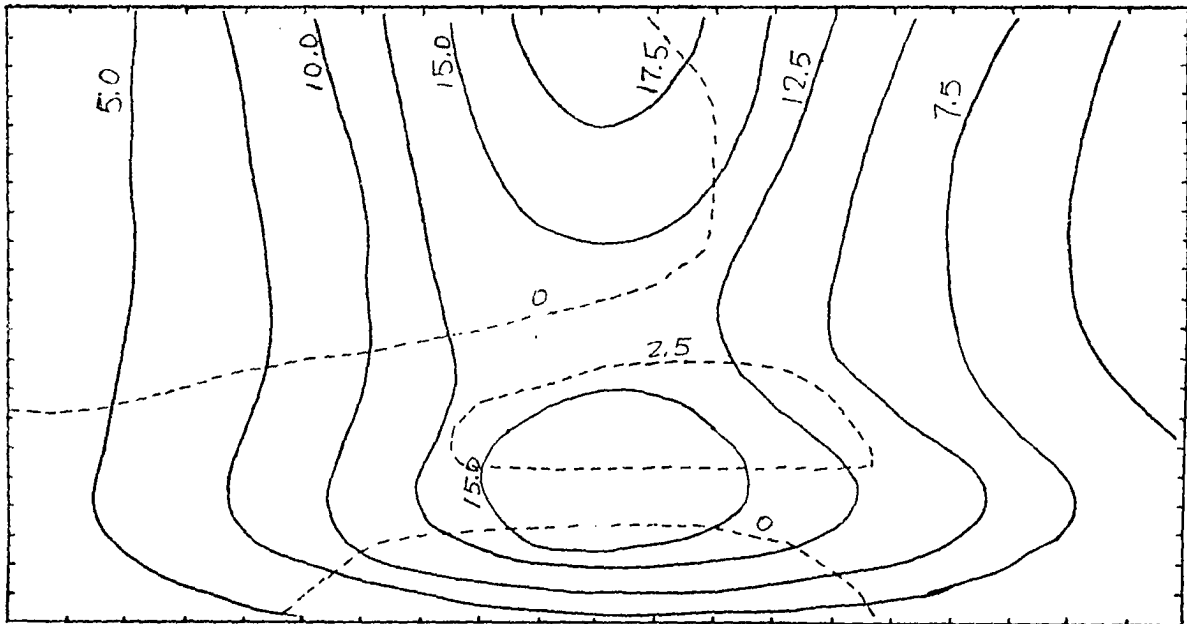


Fig. 4j. Same as Fig. 4a., except for 0600 LST on the second day.

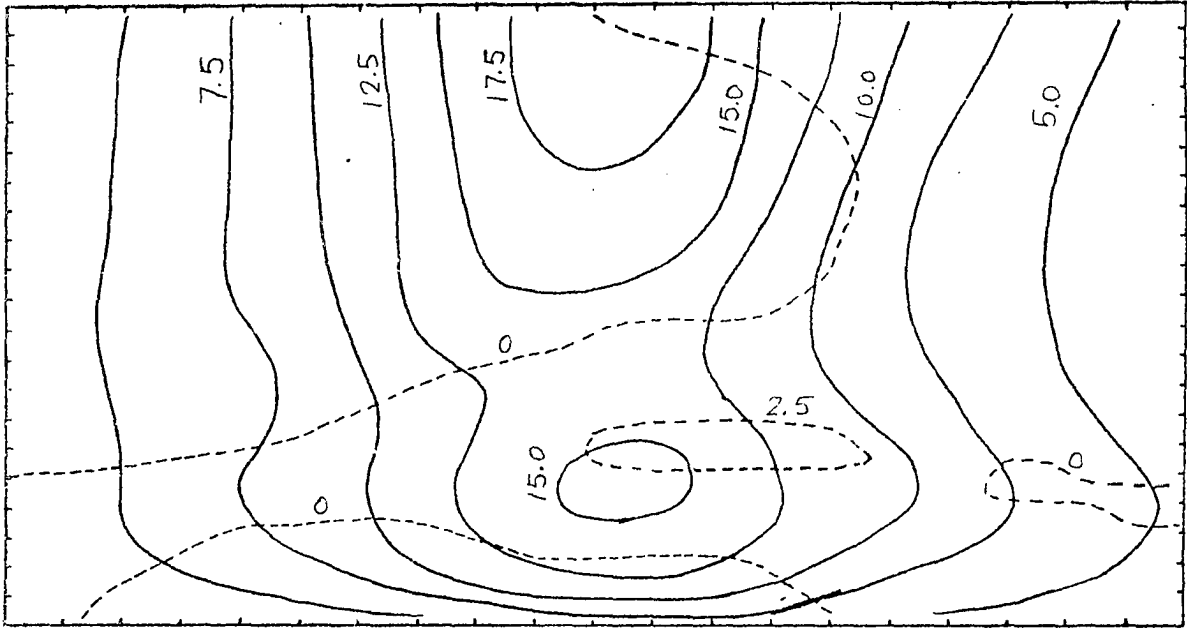


Fig. 4k. Same as Fig. 4a., except for 0800 LST on the second day.

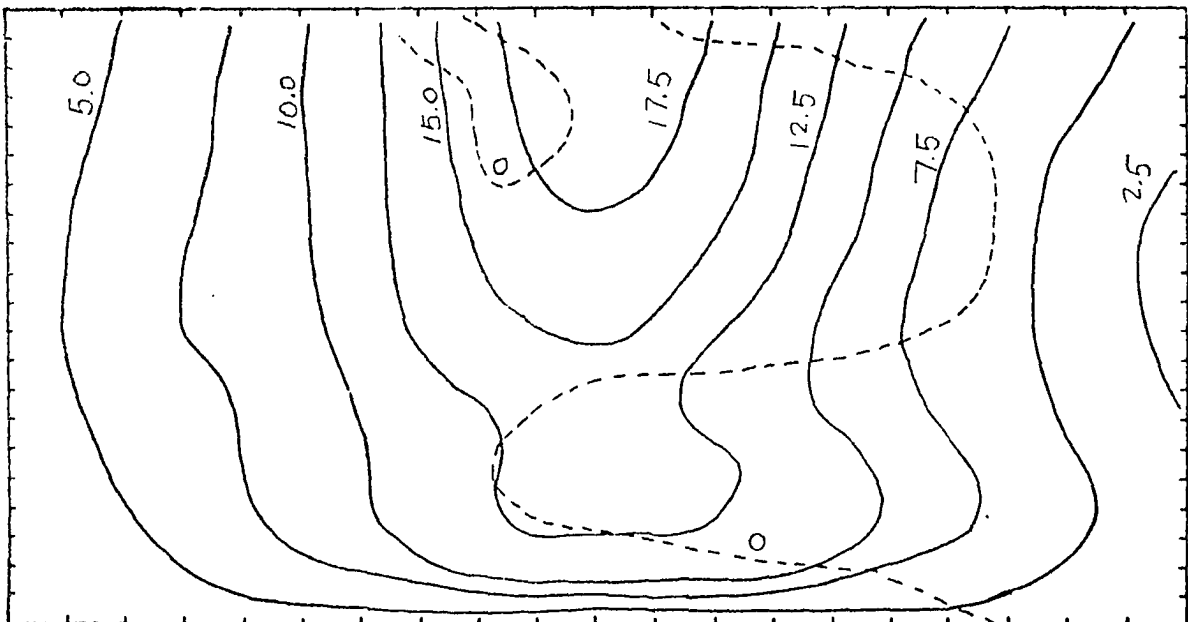


Fig. 4l. Same as Fig. 4a., except for 1000 LST on the second day.

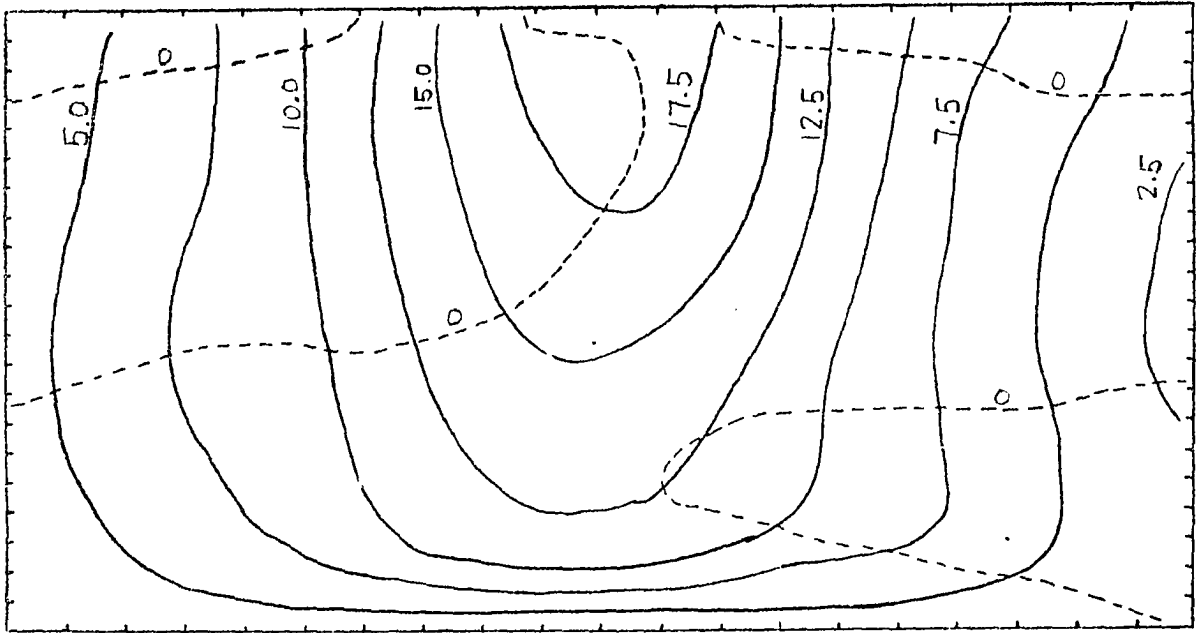


Fig. 4m. Same as Fig. 4a., except for 1200 LST on the second day.

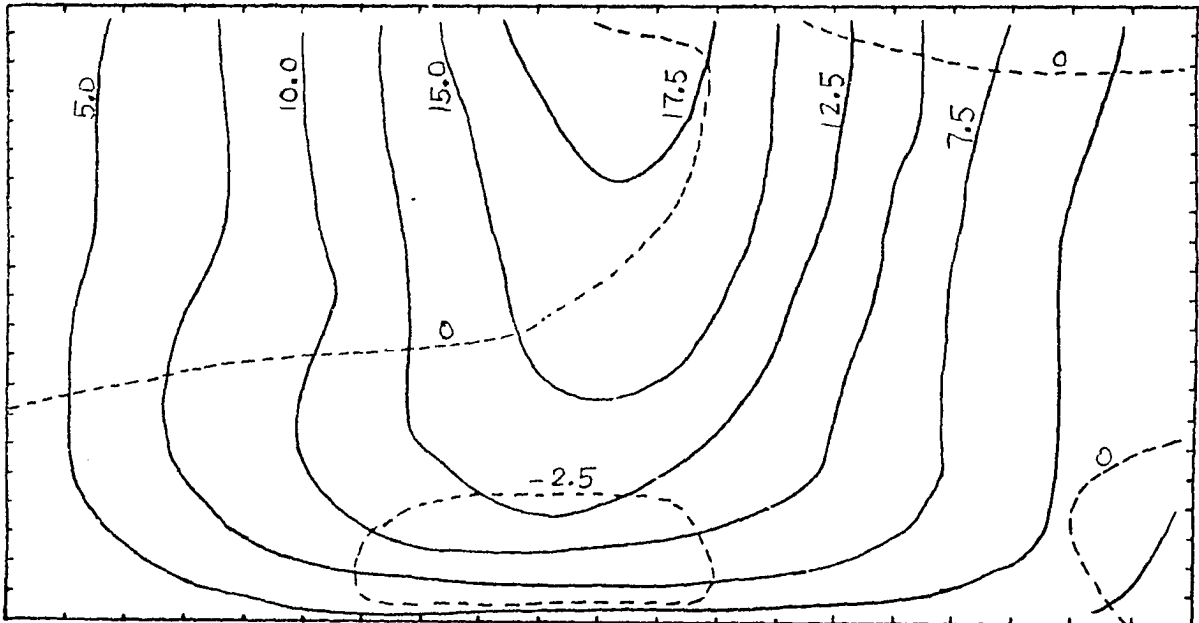


Fig. 4n. Same as Fig. 4a., except for 1400 LST on the second day.

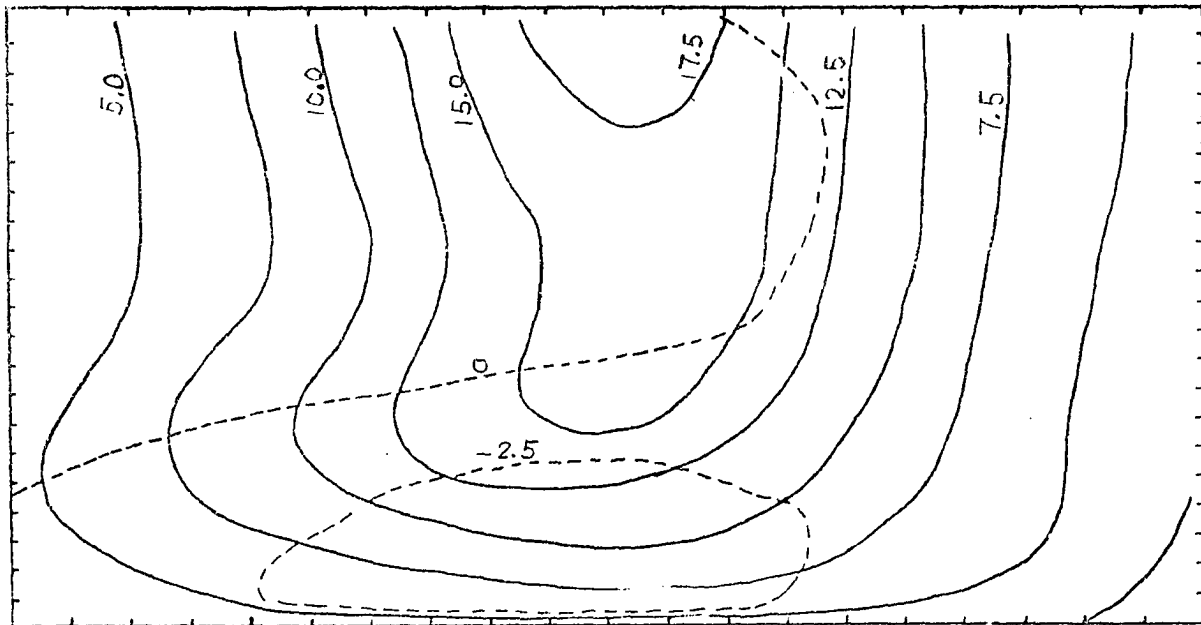


Fig. 4o. Same as Fig. 4a., except for 1600 LST on the second day.

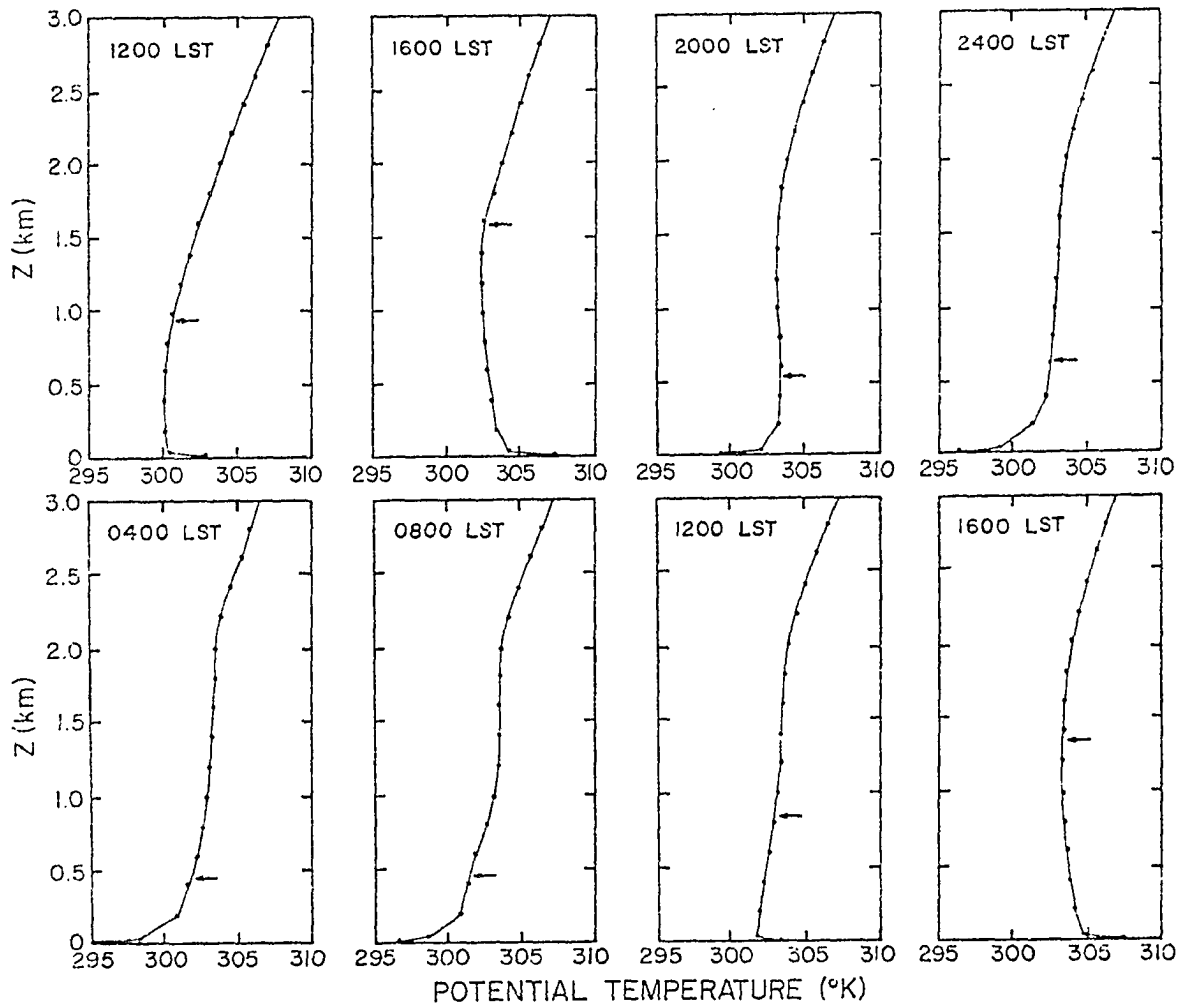


Fig. 5. Potential temperature profiles for the middle grid point for Case IV. The time is indicated at the upper-left corner of the figure. The arrows in each figure indicate the PBL height predicted by the model.

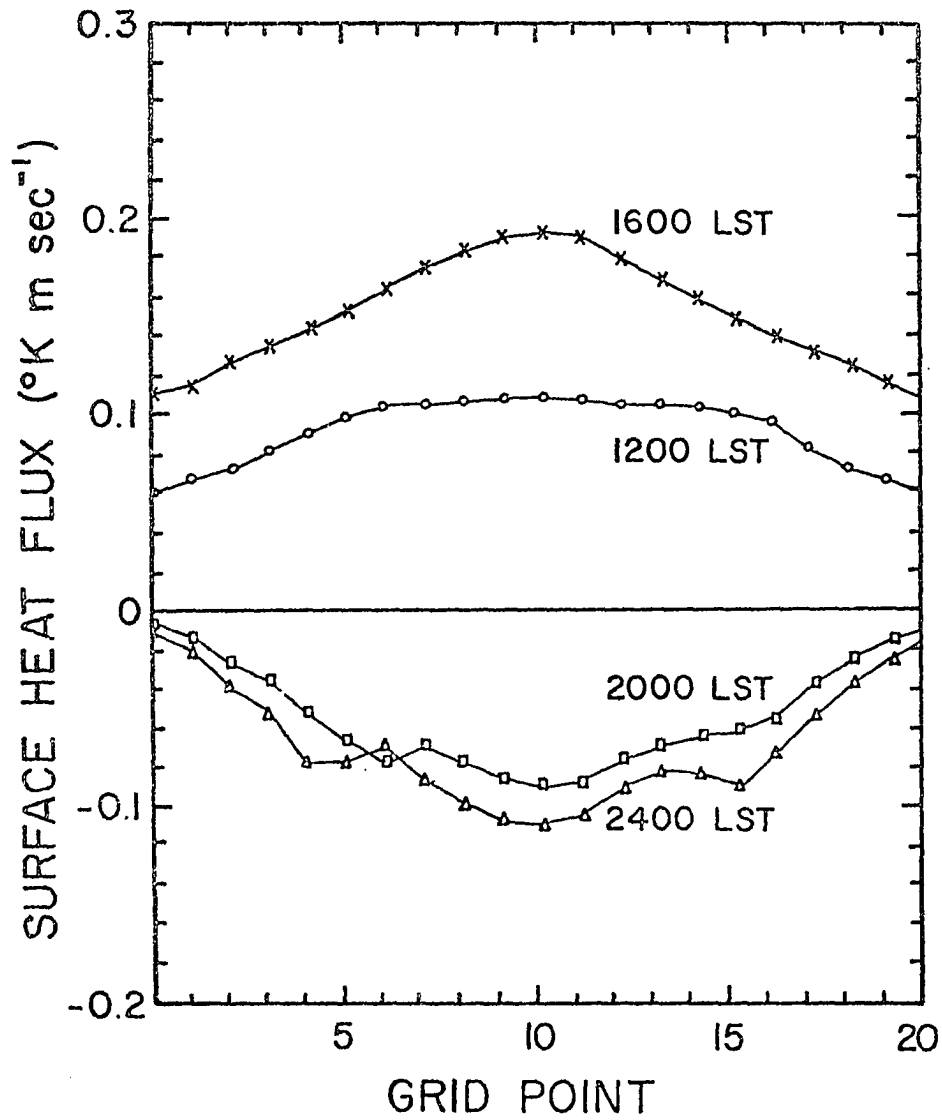


Fig. 6. Surface heat flux predicted by the model for Case IV.

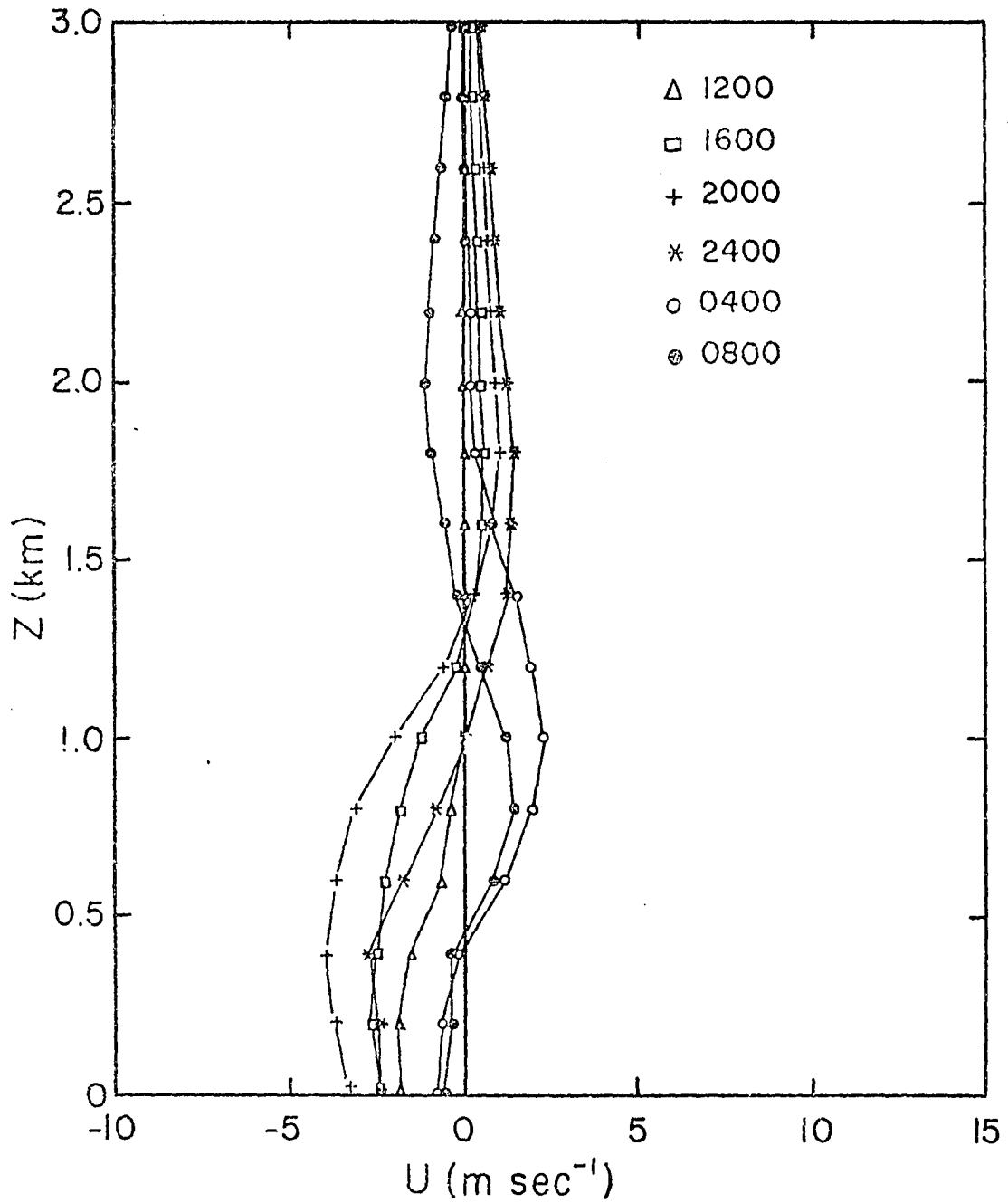


Fig. 7. u -profiles for the middle grid point for Case I (slope = 0). All times are LST.

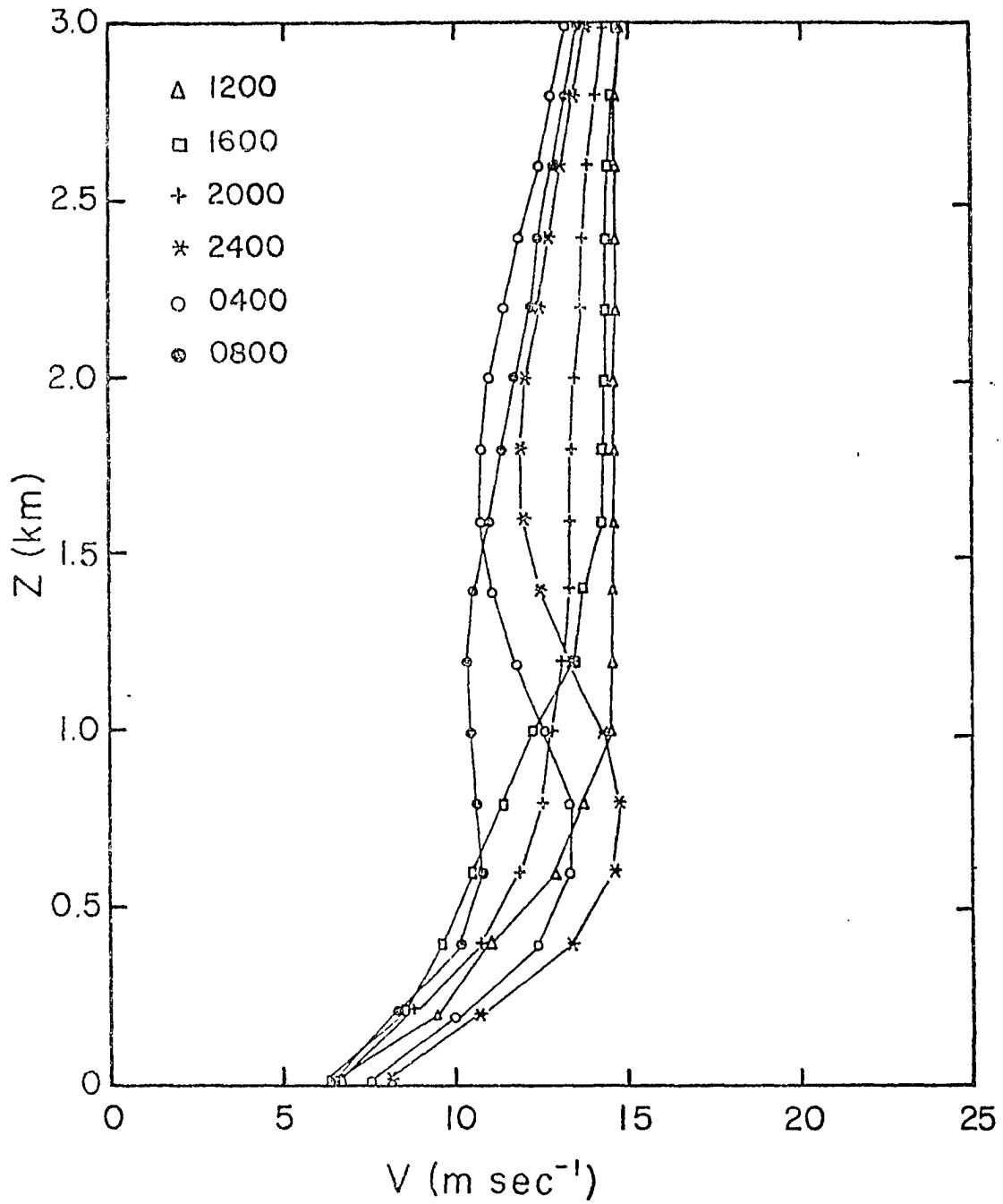


Fig. 8. v -profiles for the middle grid point for Case I.

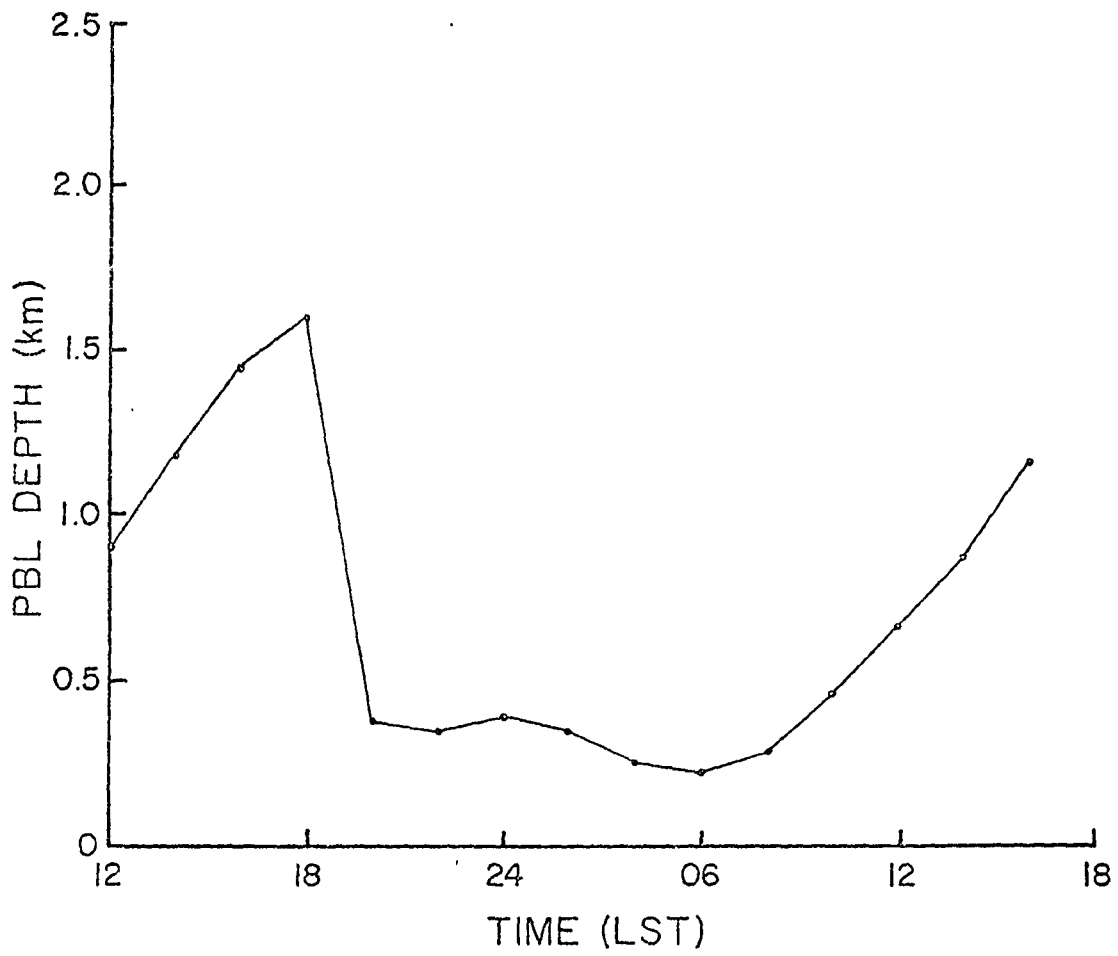


Fig. 9. Diurnal variation of PBL depth for the middle grid point for Case I.

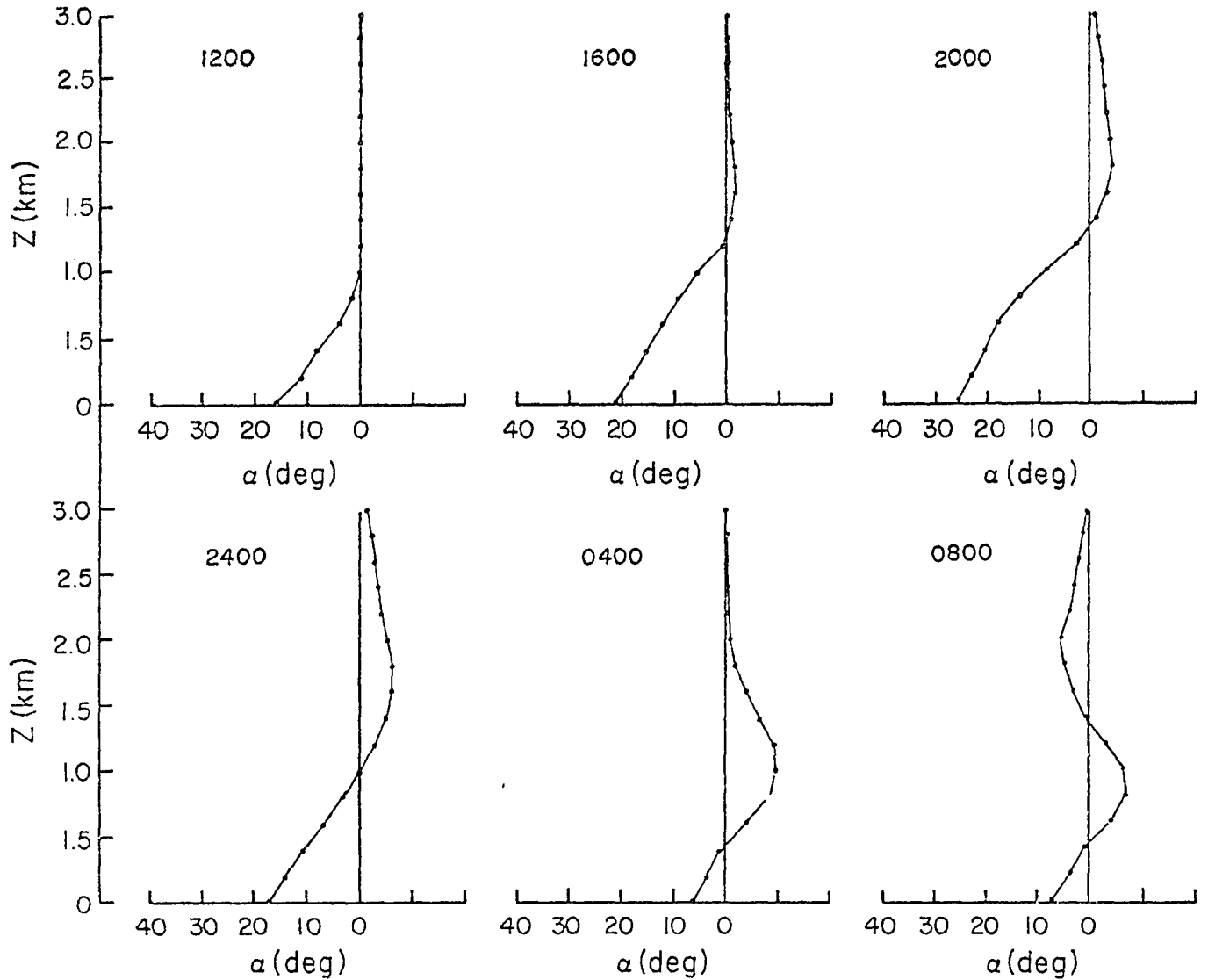


Fig. 10. Diurnal variation of the veering angle for the middle grid point for Case I. The veering angle is defined as the angle between the horizontal wind vector and the geostrophic wind. Positive value of veering angle indicate cross-isobar flow toward low pressure, and vice versa.

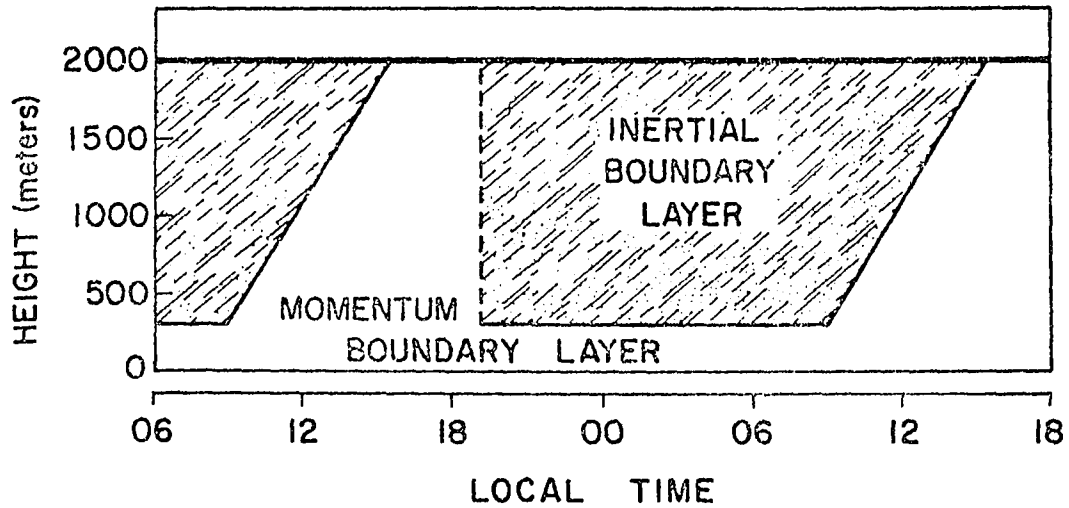


Fig. 11. Schematic diagram showing the diurnal variation of PBL depth as suggested by Hoxit (1973). The terminology "inertial boundary layer" is used by Hoxit because of the fact that within this layer the wind vector shows strong inertial rotation.

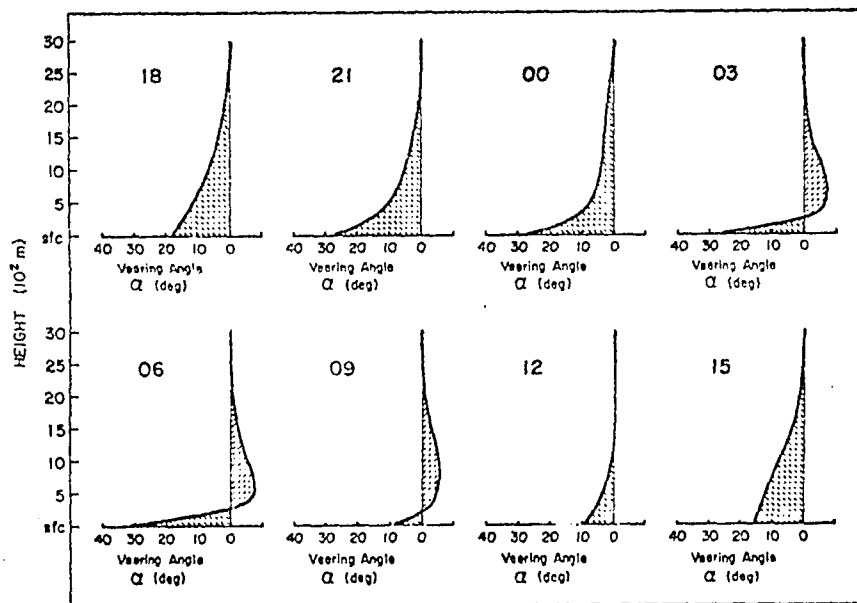


Fig. 12. Same as Fig. 10 except this figure is based on observations for the southeast United States (Hoxit, 1973).

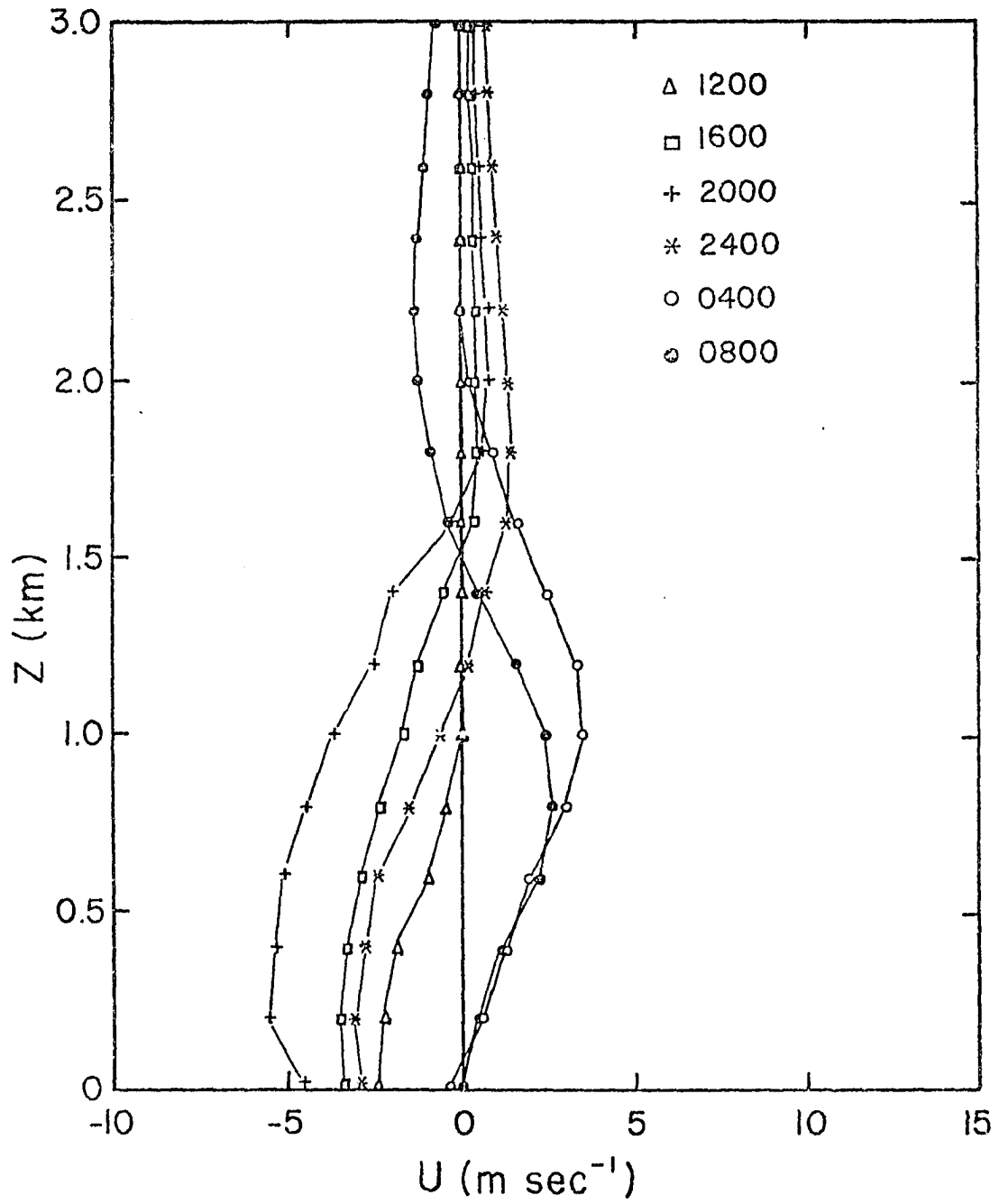


Fig. 13. Diurnal variation of u-profiles for the middle grid-point for Case II (slope = 1/600).

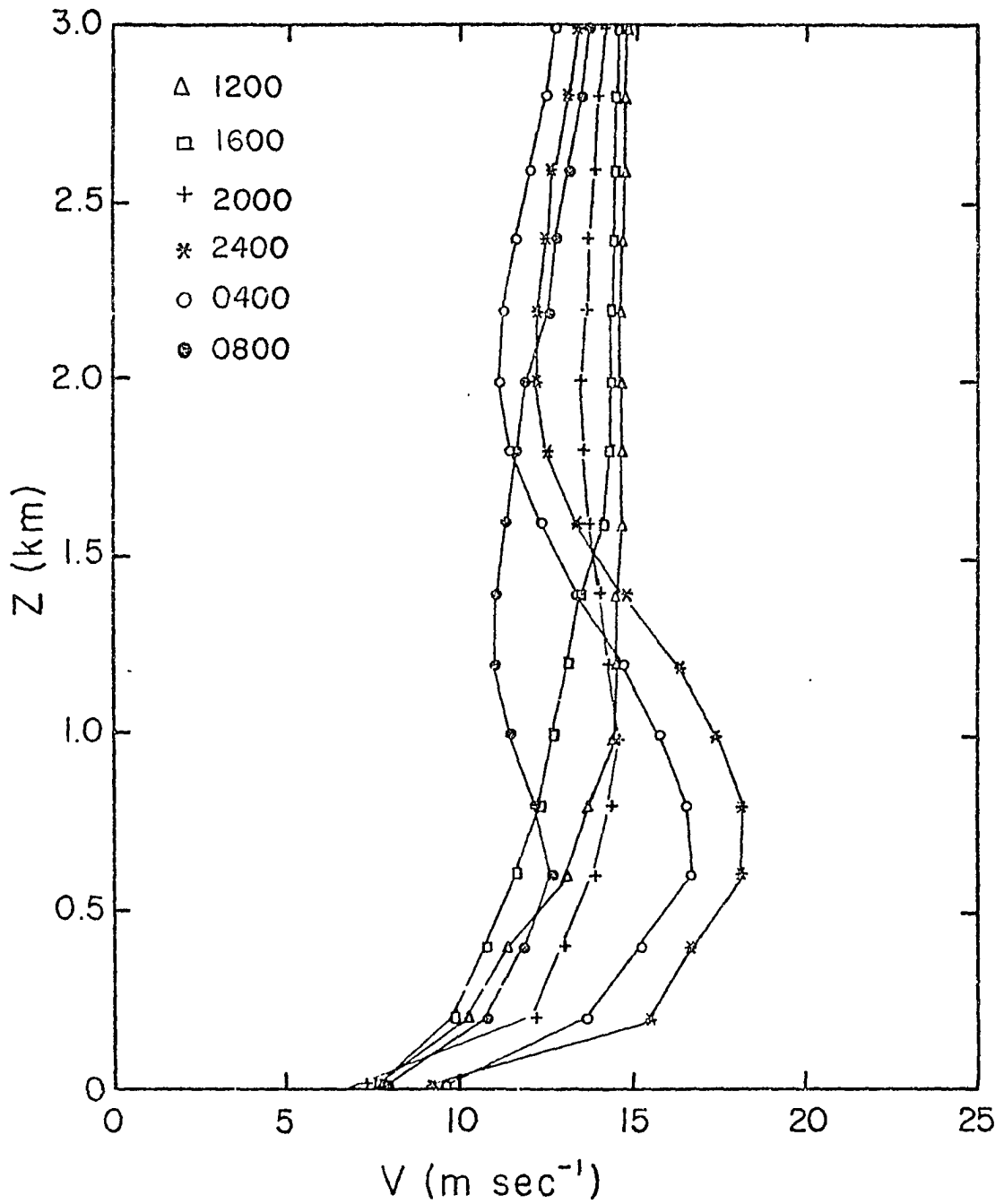


Fig. 14. Same as Fig. 13 except for v-profiles.

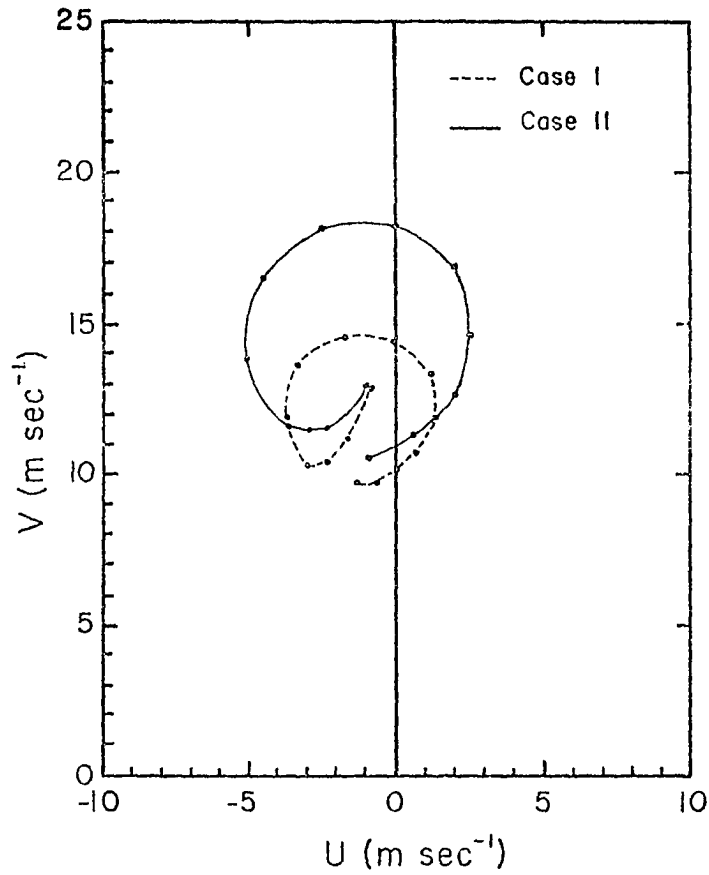


Fig. 15. Hodographs for the middle grid point at an altitude 625 m above ground. The hodographs start at 1200 LST and the interval between dots is 2 hrs.

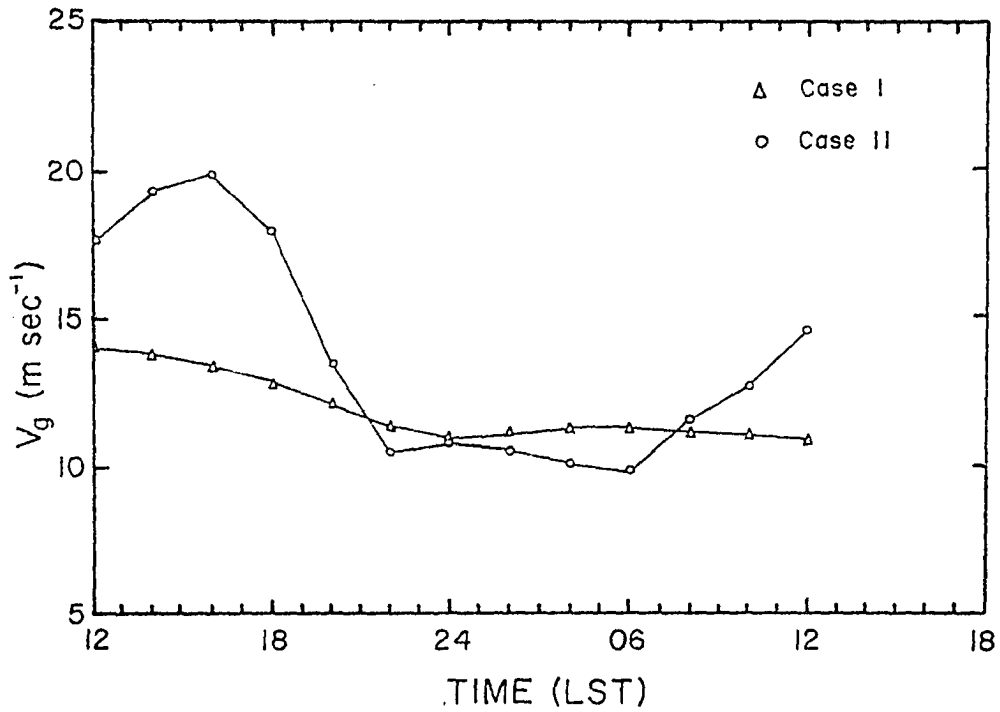


Fig. 16. Diurnal variation of the surface geostrophic wind for the middle grid point.

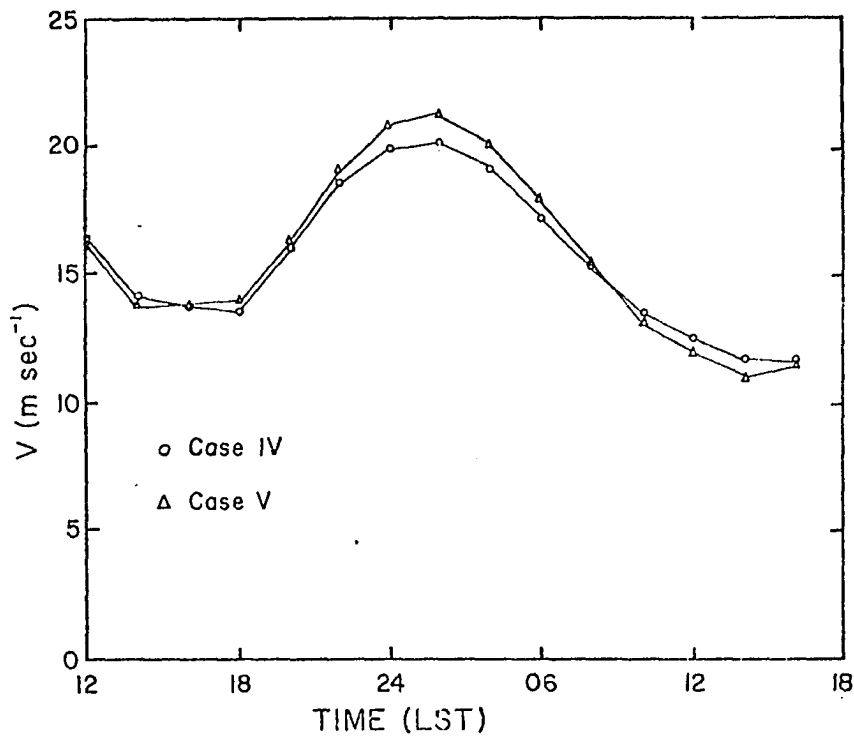


Fig. 17. A comparison of diurnal wind variations associated with large and small amplitude temperature waves. The y-component of the wind at the middle grid point of the model at 625 m above the ground is shown.

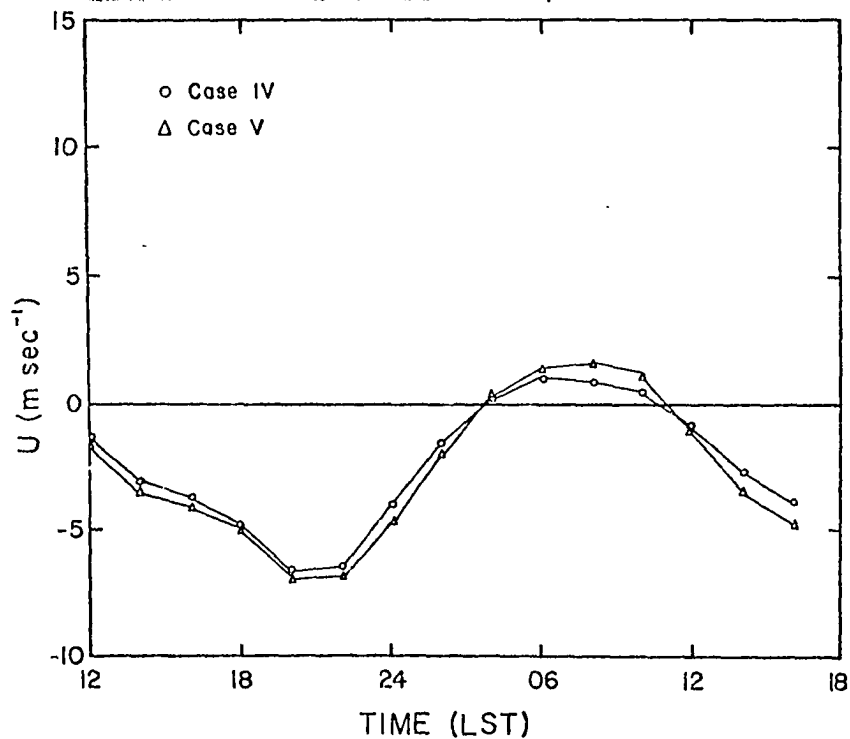


Fig. 18. Same as Fig. 17, except for the x-component.

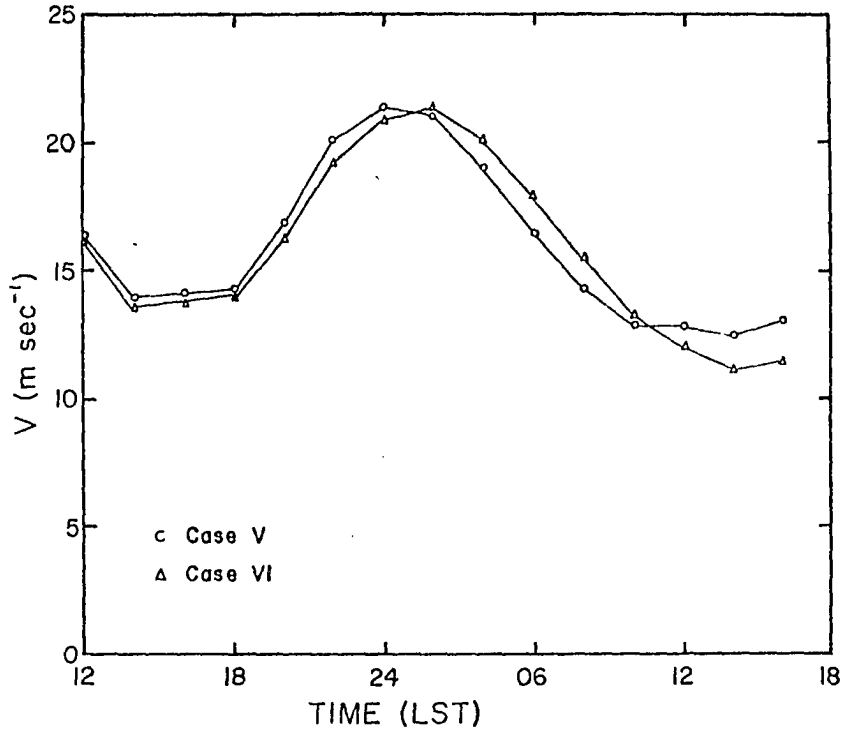


Fig. 19. A comparison of diurnal wind variations at different latitudes. The y-component of winds at middle grid point and 625 m above ground for Case V ($\varphi = 35^\circ\text{N}$); and Case VI ($\varphi = 40^\circ\text{N}$).

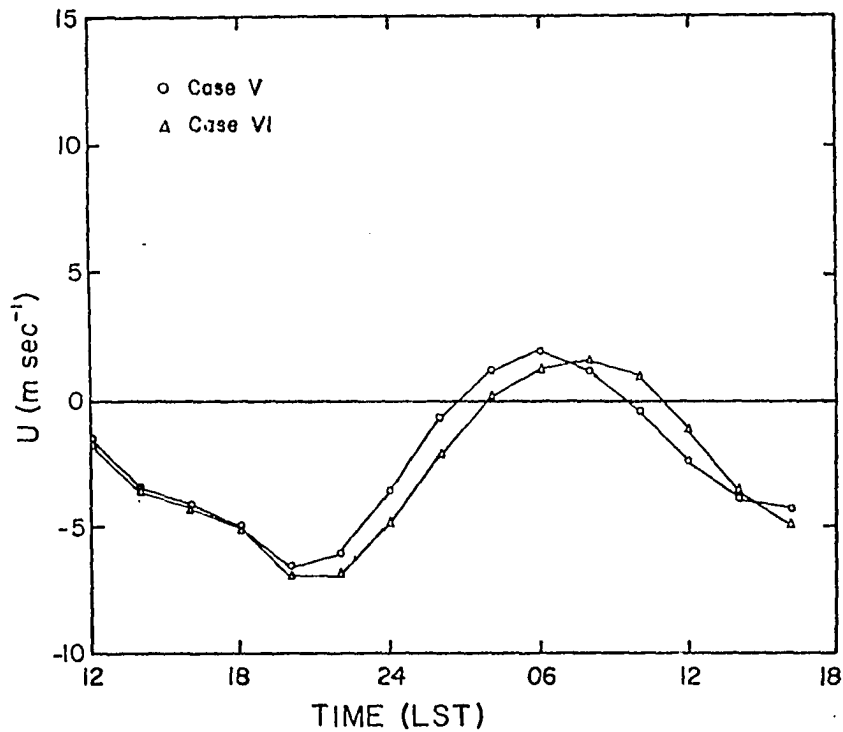


Fig. 20. Same as Fig. 19, except for x-component of winds.

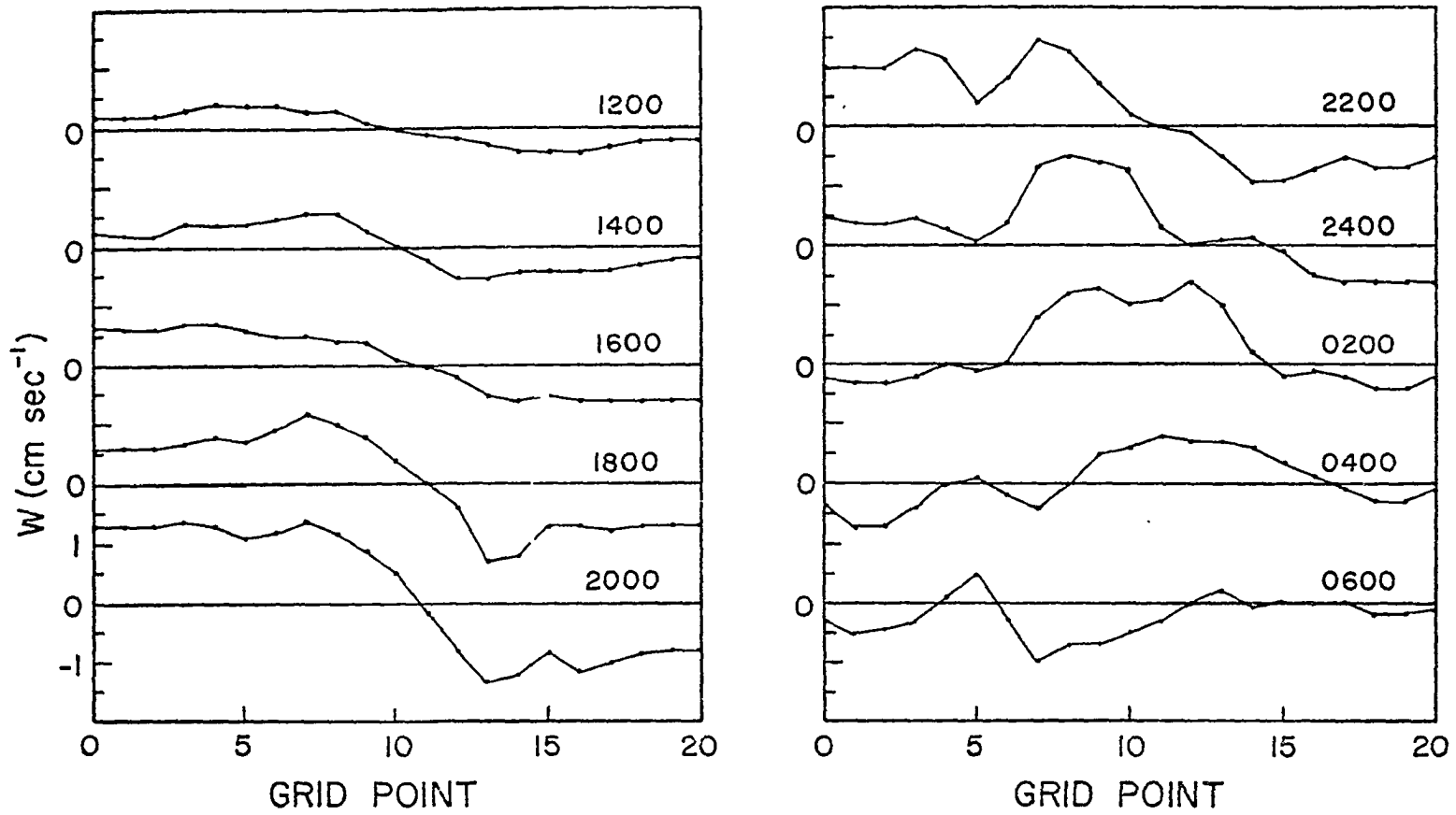


Fig. 21. Vertical velocity at 2 km above ground for Case IV. The interval between each scale mark on the left-hand side of the figure is 0.5 cm sec^{-1} . Times are indicated above each zero-base line.

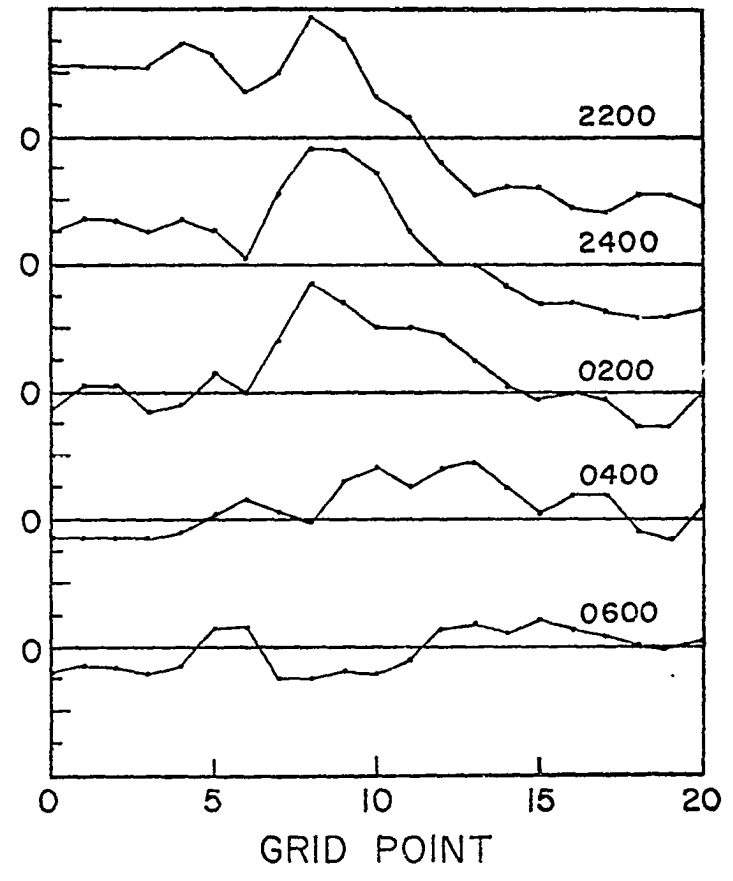
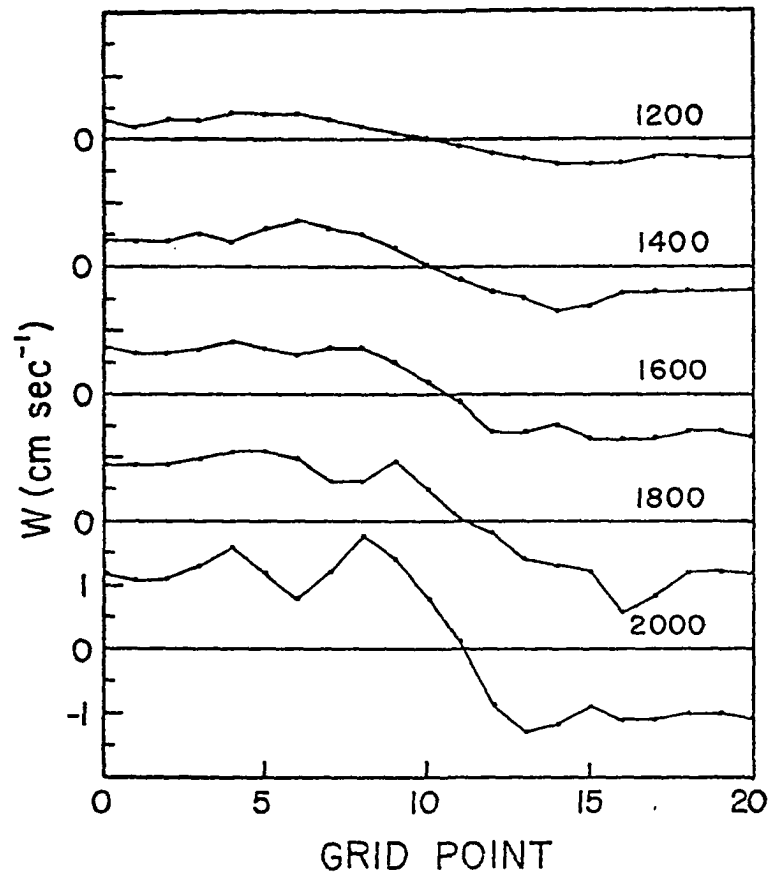


Fig. 22. Same as Fig. 21 except for Case V.

APPENDIX A

THE WAVE SOLUTIONS INHERENT IN THE NUMERICAL MODEL AND CONSISTENT UPPER BOUNDARY CONDITIONS

With the assumption of small values of the Rossby number R_0 , the Ekman number E , and the aspect ratio λ , a set of linear equations is obtained from the results of the scale analysis in Chapter II. Omitting the terms associated with R_0 , E , and λ does not dramatically change the basic physical mechanism responsible for the wave phenomena. Terms associated with the Rossby number are responsible for the non-linear interaction between different wave modes; this interaction is only of secondary physical significance. Terms associated with the Ekman number are responsible for the damping effects of wave activity. With the understanding that the basic state is in geostrophic and hydrostatic balance, the linearized equations may be written as

$$\frac{\partial u}{\partial t} - \hat{f} v = - \frac{\partial \hat{p}}{\partial x} - \hat{\theta} \sin \varphi , \quad (\text{A.1})$$

$$\frac{\partial v}{\partial t} + \hat{f} u = 0 , \quad (\text{A.2})$$

$$\frac{\partial \hat{\theta}}{\partial t} + N^2 (w \cos \varphi - u \sin \varphi) = 0, \quad (\text{A.3})$$

$$\frac{\partial \hat{p}}{\partial z} = \hat{\theta} \cos \varphi, \quad \text{and} \quad (\text{A.4})$$

$$\frac{\partial u}{\partial x} + \frac{\partial w}{\partial z} = 0. \quad (\text{A.5})$$

In these equations, $\hat{f} = f \cos \varphi$, $\hat{p} = p/\rho_m$, $\hat{\theta} = g\alpha_m \theta$, $N^2 = \Gamma g\alpha_m$. Other symbols have the same meaning as in Chapter II. With some mathematical manipulation of this set of equations a single equation in \hat{p} may be written as

$$\frac{\partial^3}{\partial t^3} \left(\frac{\partial^2 \hat{p}}{\partial z^2} \right) + (\hat{f}^2 + N^2 \sin^2 \varphi) \frac{\partial}{\partial t} \left(\frac{\partial^2 \hat{p}}{\partial z^2} \right) + N^2 \cos^2 \varphi \frac{\partial}{\partial t} \left(\frac{\partial^2 \hat{p}}{\partial x^2} \right) = 0. \quad (\text{A.6})$$

N is the Brunt-Väisälä frequency and its value is determined by the lapse rate of the basic state temperature field. For simplicity \hat{f} and N are assumed to be constants so that the normal mode method can be applied. Since the horizontal domain of the physical model extends to infinity, a harmonic form can be assumed as a solution along the horizontal direction. The solution in the vertical direction depends primarily on the upper and lower boundary conditions used in the model. A solution of the form

$$\hat{p} = P(z) \exp [i(kx - \nu t)], \quad (\text{A.7})$$

is assumed, where k is the horizontal wave number and ν is the frequency.

By substituting (A.7) into (A.6) the partial

differential equation is reduced to

$$\frac{d^2 P}{dz^2} + \mu^2 P = 0 , \quad (\text{A.8})$$

where

$$\mu^2 \equiv \frac{k^2 N^2 \cos^2 \varphi}{v^2 - (f^2 + N^2 \sin^2 \varphi)} . \quad (\text{A.9})$$

The solution of (A.8) then becomes the so-called eigenvalue problem; it depends on the boundary conditions only. The μ 's are the eigenvalues to be determined. The physical lower boundary condition consistent with the equation set (A.1) - (A.5) is the free-slip condition over the material surface. Thus,

$$w = \frac{\partial u}{\partial z} = \frac{\partial v}{\partial z} \equiv 0 \quad \text{at } z = 0 . \quad (\text{A.10})$$

On the other hand, there are several choices for the upper boundary condition. It is desired that the choice of the upper boundary condition may satisfy the physical condition there and also render an internal gravity wave solution ($\mu^2 > 0$). Under this consideration the upper boundary condition for \hat{p} becomes

$$\hat{p} = 0 \quad \text{at } z = D , \quad (\text{A.11})$$

where D is the top of the model. Since \hat{p} represents the time varying pressure perturbation its vanishing at the top of the model means that the total pressure at the top of the model

is time invariant and is equal to its initial value. This is because it is assumed that the mass field above the model is not disturbed by the activity within the model domain; thus, by the hydrostatic equation total pressure at the top of the domain is time invariant. The mathematical conditions equivalent to (A.10) and (A.11) are

$$\frac{dP}{dz} = 0 \quad \text{at } z = 0 \quad \text{and } P = 0 \quad \text{at } z = D . \quad (\text{A.12})$$

Then the eigenfunctions of (A.8) with the boundary condition (A.12) becomes

$$P(z) = A \cos \mu z , \quad (\text{A.13})$$

where A is an arbitrary constant amplitude and

$$\mu D = \frac{\pi}{2} , \quad \frac{3\pi}{2} , \quad \frac{5\pi}{2} , \quad \text{-----} . \quad (\text{A.14})$$

So the eigenvalues, with the proposed boundary conditions, are always real which implies that the solutions represent an internal type wave.

The horizontal phase speed of the wave is

$$C_x \equiv \frac{v}{k} = \pm \left[\frac{f^2 + N^2 \sin^2 \varphi}{k^2} + \frac{N^2}{\mu^2} \cos^2 \varphi \right]^{\frac{1}{2}} . \quad (\text{A.15})$$

This is the familiar inertial-gravity wave; the form is slightly modified terrain coordinates. Since the phase speed C_x depends on the wave number (k, μ) so it is a dispersive type of wave.

APPENDIX B

A PROOF OF THE STABILITY OF THE FINITE-DIFFERENCE TREATMENT OF THE ADVECTION EQUATIONS

Nonlinear computational instability is a phenomenon that arises because of the nonlinear interaction between different wave modes in the numerical evaluation of the advection terms in the hydro-thermodynamic equations. Linear and quadratic quantities associated with the calculations are continuously accumulated by the aliasing processes in the wave band of $2d$ and $4d$ waves and finally become unbounded. So a necessary, though not sufficient, condition for stability is that linear and quadratic quantities be conserved throughout the numerical integration if there are no sources or sinks. Arakawa (1966) proposed a method to treat the vorticity equation; Lilly (1965) further extended this idea and proposed a method for treating the primitive form of the shallow water equations. In general, in order to form a conservative scheme, there should be consistency in the finite-difference forms of the continuity equation and the advection equations.

Because of the hydrostatic assumption and the two dimensionality of the numerical model proposed for the simulation of the low-level jet, it is impossible either to form a vorticity equation or to express the equations in a form similar to the shallow water equations. So the methods used by Arakawa and Lilly cannot be applied directly to the numerical model of the low-level jet. But with a careful examination of the governing equations it is still possible to form a pseudo-conservative scheme to treat the nonlinear terms. Simple advection equations similar to those used in the simulation experiment may be written as

$$\frac{\partial u}{\partial t} + \frac{\partial}{\partial x}(u u) + \frac{\partial}{\partial z}(u w) = 0 , \quad (\text{B.1})$$

$$\frac{\partial v}{\partial t} + \frac{\partial}{\partial x}(u v) + \frac{\partial}{\partial z}(v w) = 0 , \quad (\text{B.2})$$

$$\frac{\partial \theta}{\partial t} + \frac{\partial}{\partial x}(u \theta) + \frac{\partial}{\partial z}(w \theta) = 0 , \quad \text{and} \quad (\text{B.3})$$

$$\frac{\partial u}{\partial x} + \frac{\partial w}{\partial z} = 0 . \quad (\text{B.4})$$

It can be easily proved that the linear quantities u , v , θ and the quadratic quantities u^2 , v^2 , θ^2 are conserved provided that there are no net boundary fluxes into the integration domain. However, for the finite-difference analogue of this set of equations a similar property is not necessarily guaranteed. This is caused by nonlinear interactions of different wave modes in a finite spectral domain; aliasing

will eventually render an unbounded error. To insure stability in the absence of source and/or sink terms and net boundary fluxes the finite-difference analogue of the advection terms should conserve linear and/or quadratic quantities. The finite-difference analogues of (B.1), (B.2), (B.3), and (B.4) used in the numerical experiment are

$$\delta_t \bar{u}^t + \delta_x (\bar{u}^x \bar{u}^x) + \delta_z (\bar{w}^z \bar{u}^z) = 0 , \quad (\text{B.5})$$

$$\delta_t \bar{v}^t + \delta_x (\bar{u}^x \bar{v}^x) + \delta_z (\bar{w}^z \bar{v}^z) = 0 , \quad (\text{B.6})$$

$$\delta_t \bar{\theta}^t + \delta_x (\bar{u}^x \bar{\theta}^x) + \delta_z (\bar{w}^z \bar{\theta}^z) = 0 , \quad (\text{B.7})$$

$$\delta_x \bar{u}^x + \delta_z \bar{w}^z = 0 . \quad (\text{B.8})$$

For further verification of the stability properties of the proposed numerical scheme it is very helpful to define some finite-difference operators and useful relations as follows:

$$\delta_x \varphi \equiv (\varphi_{i+\frac{1}{2}} - \varphi_{i-\frac{1}{2}})/d , \quad (\text{B.9})$$

$$\bar{\varphi}^x \equiv (\varphi_{i+\frac{1}{2}} + \varphi_{i-\frac{1}{2}})/2 . \quad (\text{B.10})$$

In this definition, d is the distance between grid points and the subscript i has its usual meaning. With the above definitions it can be shown that

$$\delta_x \bar{\varphi}^x = \overline{\delta_x \varphi^x} = (\varphi_{i+1} - \varphi_{i-1})/(2d) , \quad (\text{B.11})$$

$$\varphi \delta_x \psi = \delta_x (\bar{\varphi}^x \psi) - \overline{\psi \delta_x \varphi^x} , \quad (\text{B.12})$$

$$\overline{\varphi}^x \delta_x \varphi = \delta_x (\varphi^2/2) . \quad (\text{B.13})$$

Eqs. (B.12) and (B.13) are the finite-difference analogues of the distributive law of derivatives. Since the advection terms of (B.5), (B.6), and (B.7) are written in flux form it is obvious that this finite-difference scheme conserves linear quantities over the integration domain if there is no net boundary flux into the domain. The conservation of quadratic quantities can be verified as follows. After multiplying both sides of (B.7) by θ and using (B.11), (B.12), and (B.13) the equation becomes

$$\begin{aligned} \delta_t [(\overline{\theta}^t)^2] - \overline{\theta}^t \delta_t \theta + \delta_x [\overline{u}^x (\overline{\theta}^x)^2] - \overline{u}^x \overline{\theta}^x \delta_x \theta \\ + \delta_z [\overline{w}^z (\overline{\theta}^z)^2] - \overline{w}^z \overline{\theta}^z \delta_z \theta = 0 . \end{aligned} \quad (\text{B.14})$$

After adding $-\theta^2 [\delta_x \overline{u}^x + \delta_z \overline{w}^z]/2$ to (B.14) and performing additional manipulations the equation may be written as

$$\begin{aligned} \delta_t [(\overline{\theta}^t)^2 - (\frac{\theta^2}{2})] + \delta_x [\overline{u}^x (\overline{\theta}^x)^2] - \overline{u}^x \delta_x (\frac{\theta^2}{2}) \\ + \delta_z [\overline{w}^z (\overline{\theta}^z)^2] - \overline{w}^z \delta_z (\frac{\theta^2}{2}) \\ - \left\{ \begin{aligned} & \delta_x [\overline{u}^x (\frac{\theta^2}{2})] - \overline{u}^x \delta_x (\frac{\theta^2}{2}) + \delta_z [\overline{w}^z (\frac{\theta^2}{2})] \\ & - \overline{w}^z \delta_z (\frac{\theta^2}{2}) \end{aligned} \right\} = 0 . \end{aligned} \quad (\text{B.15})$$

After cancellation of the identical terms within (B.15)

the finite-difference analogue of the conservation equation becomes

$$\begin{aligned} \delta_t \left[(\bar{\theta}^t)^2 - \left(\frac{\theta^2}{2} \right)^t \right] = & - \delta_x \left[\bar{u}^x \left((\bar{\theta}^x)^2 - \left(\frac{\theta^2}{2} \right)^x \right) \right] \\ & - \delta_z \left[\bar{w}^z \left((\bar{\theta}^z)^2 - \left(\frac{\theta^2}{2} \right)^z \right) \right]. \end{aligned} \quad (\text{B.16})$$

From (B.16) it can easily be seen that when the terms in (B.16) are summed over the integration domain the quadratic quantity $(\bar{\theta}^t)^2 - \left(\frac{\theta^2}{2} \right)^t$ is conserved provided there is no net boundary flux. A similar relation can be derived for the kinetic energy $\frac{u^2 + v^2}{2}$.

In summary the quadratic quantities are conserved by this kind of finite-difference treatment of the advection terms. However, this does not necessarily prevent other kinds of instability, especially instability associated with the time integration method. However, when the equations are integrated numerically and the linear stability criterion is satisfied satisfactory stable calculations are obtained.

APPENDIX C

OPEN BOUNDARY CONDITIONS

For numerical simulation of localized atmospheric or oceanic phenomena, the domain of the model is usually truncated to a finite space extent to conform to time and storage limitations of the computer. This may become a serious problem for those phenomena involving wave generation and wave propagation. The artificially posed boundary conditions at the boundaries may cause reflection of the incident wave and as time goes on the spurious reflected waves propagate back into the domain of interest and contaminate the forecast field. So the search for an ideal boundary condition which allows waves generated inside the domain to propagate through the boundary has long been an important problem.

Boundary conditions which allow waves to pass through are generally called open boundary conditions. On the other hand it is well known that the specified value or slope at the artificial boundary does cause reflection of the incident waves. Among open boundary conditions, the Sommerfeld radiation boundary condition has been used in many different forms. Below the properties of the Sommerfeld condition are discussed

and a new open boundary condition is proposed. Then a comparison between these two open boundary conditions is made.

The Sommerfeld radiation boundary condition for a variable φ is formulated as

$$\frac{\partial \varphi}{\partial t} + \tilde{c} \frac{\partial \varphi}{\partial x} = 0, \quad (\text{C.1})$$

at the boundary of the model. It can be shown (Pearson, 1974) that if \tilde{c} is chosen to be the phase speed of the incident wave the wave can completely pass through the boundary. This is true provided that (C.1) is evaluated in analytic form. For numerical simulation of atmospheric phenomena the waves generally are of the dispersive type. That is, the phase speed of the waves depends on the wave number. Under this condition the incident waves at the boundary have different phase speeds. With a definite value of \tilde{c} the Sommerfeld boundary condition will cause partially transmitted and partially reflected waves. Pearson (1974) suggested that the value of \tilde{c} can be determined a priori if the waves generated inside the domain are of certain types. However, this situation is not generally reliable. On the other hand, Nitta (1962) suggested that \tilde{c} be equal to u_I , the velocity at the outflow boundary. Shapiro and O'Brien (1970) used $\tilde{c} = u + c$, where u is the velocity at the boundary point and c is a predetermined wave speed. The computational stability at localized points required that (C.1) be formulated as

$$\varphi_I^{n+1} = \varphi_I^{n-1} - \frac{2 \Delta t \tilde{c}}{\Delta x} (\varphi_I^{n-1} - \varphi_{I-1}^{n-1}), \quad (\text{C.2})$$

where I is the grid point at the boundary of the numerical

model and n denotes the time step of the numerical calculation. This formulation is known as a forward time and upstream finite-difference approximation. Assuming an incident wave at $n-1$ time step is of the form

$$\varphi_j^{n-1} = A \cos k[j \Delta x - (n-1) c \Delta t] , \quad (C.3)$$

where k is the wave number and c is the phase speed of an incident wave, the forecast value of the impending wave at the boundary grid "I" by (C.2) becomes

$$\begin{aligned} \varphi_I^{n+1} = & A[(1 - \tilde{\lambda}) \cos \frac{2\pi\lambda}{p} + \tilde{\lambda} \cos \frac{2\pi(\lambda-1)}{p}]x \\ & \cos k[I \Delta x - (n+1) c \Delta t] + \\ & A[(\tilde{\lambda} - 1) \sin \frac{2\pi\lambda}{p} - \tilde{\lambda} \sin \frac{2\pi(\lambda-1)}{p}]x \\ & \cos[\frac{\pi}{2} - k I \Delta x + k(n+1) c \Delta t] . \end{aligned} \quad (C.4)$$

Here, $\tilde{\lambda} = 2 \tilde{c} \Delta t / \Delta x$, $\lambda = 2 c \Delta t / \Delta x$, and $p = 2\pi / (k \Delta x)$. The first term on the right-hand side of (C.4) represents the transmitted part of the incident wave. The second term of (C.4) represents the spurious part of the incident wave. The spurious part has a phase lag of ninety degrees, has the opposite sign, and wave number k , compared with the incident wave. So the spurious part of the solution has a tendency to reflect back into the domain of the numerical model. The amplitudes of the transmitted part and the spurious part of the incident wave are given by A_T and A_R , respectively. Thus,

$$\frac{A_T}{A} = (1 - \tilde{\lambda}) \cos \frac{2\pi\lambda}{p} + \tilde{\lambda} \cos \frac{2\pi(\lambda-1)}{p}, \quad (C.5)$$

$$\frac{A_R}{A} = (\tilde{\lambda} - 1) \sin \frac{2\pi\lambda}{p} - \tilde{\lambda} \sin \frac{2\pi(\lambda-1)}{p}. \quad (C.6)$$

For an ideal open boundary condition it is desired that $|A_T/A| \rightarrow 1$ and $|A_R/A| \rightarrow 0$. This situation can be achieved by the Sommerfeld boundary condition as long as $\tilde{\lambda} = \lambda = 1$. Physically, this means that the constant \tilde{c} chosen in (C.2) be equal to the phase speed c of the incident wave, and the computational time step Δt be chosen such that the computational stability parameter $\tilde{\lambda}$ has a value of one. For $\tilde{\lambda} \neq 1$, even when $\tilde{c} = c$, the reflection still depends on the wave number of the incident wave. For computational stability it generally is required that λ and $\tilde{\lambda}$ be less than one. In conclusion, the successful use of the Sommerfeld boundary condition depends on a priori choice of the phase speed of the incident wave and on the wave number of the incident wave. A proposed open boundary condition for the variable φ is formulated as

$$\varphi_I^{n+1} = 3(\varphi_{I-1}^{n+1} - \varphi_{I-2}^{n+1}) + \varphi_{I-3}^{n+1}. \quad (C.7)$$

Here I is the grid point at the boundary. The variable φ at time step $n+1$ and at points next to the boundary can be evaluated by variables at time step n and $n-1$. Physically, this formulation is equivalent to a quadratic extrapolation with constant grid distance. Under this open boundary condition variables have the same curvature at the two points nearest

the boundary. This easily can be seen by rearranging (C.7) so that

$$\varphi_I^{n+1} - 2 \varphi_{I-1}^{n+1} + \varphi_{I-2}^{n+1} = \varphi_{I-1}^{n+1} - 2 \varphi_{I-2}^{n+1} + \varphi_{I-3}^{n+1}. \quad (C.8)$$

The transmission or reflection properties of this open boundary condition easily can be revealed by the same analytic procedure as before. Assuming an incident wave at time step n and grid point j is of the form

$$\varphi_j^n = A \cos k[j \Delta x - c n \Delta t], \quad (C.9)$$

at time $(n+1)\Delta t$ the open boundary condition in (C.7) predicts

$$\begin{aligned} \varphi_I^{n+1} &= A(3\cos k\Delta x - 3\cos 2k\Delta x + \cos 3k\Delta x) \cos k[I\Delta x - (n+1)c\Delta t] \\ &+ A(3 \sin k \Delta x - 3 \sin 2 k \Delta x + \sin 3 k \Delta x) \times \\ &\cos\left[\frac{\pi}{2} - k I \Delta x + k(n+1)c \Delta t\right]. \end{aligned} \quad (C.10)$$

The amplitudes of the transmitted wave, A_T , and of the spurious wave, A_R , become

$$\frac{A_T}{A} = 3 \cos \frac{2\pi}{p} - 3 \cos \frac{4\pi}{p} + \cos \frac{6\pi}{p}, \quad (C.11)$$

$$\frac{A_R}{A} = 3 \sin \frac{2\pi}{p} - 3 \sin \frac{4\pi}{p} + \sin \frac{6\pi}{p}. \quad (C.12)$$

It can be seen that the transmissivity and/or reflectivity of this open boundary condition depends only on the wave number of the impending wave. This property is very

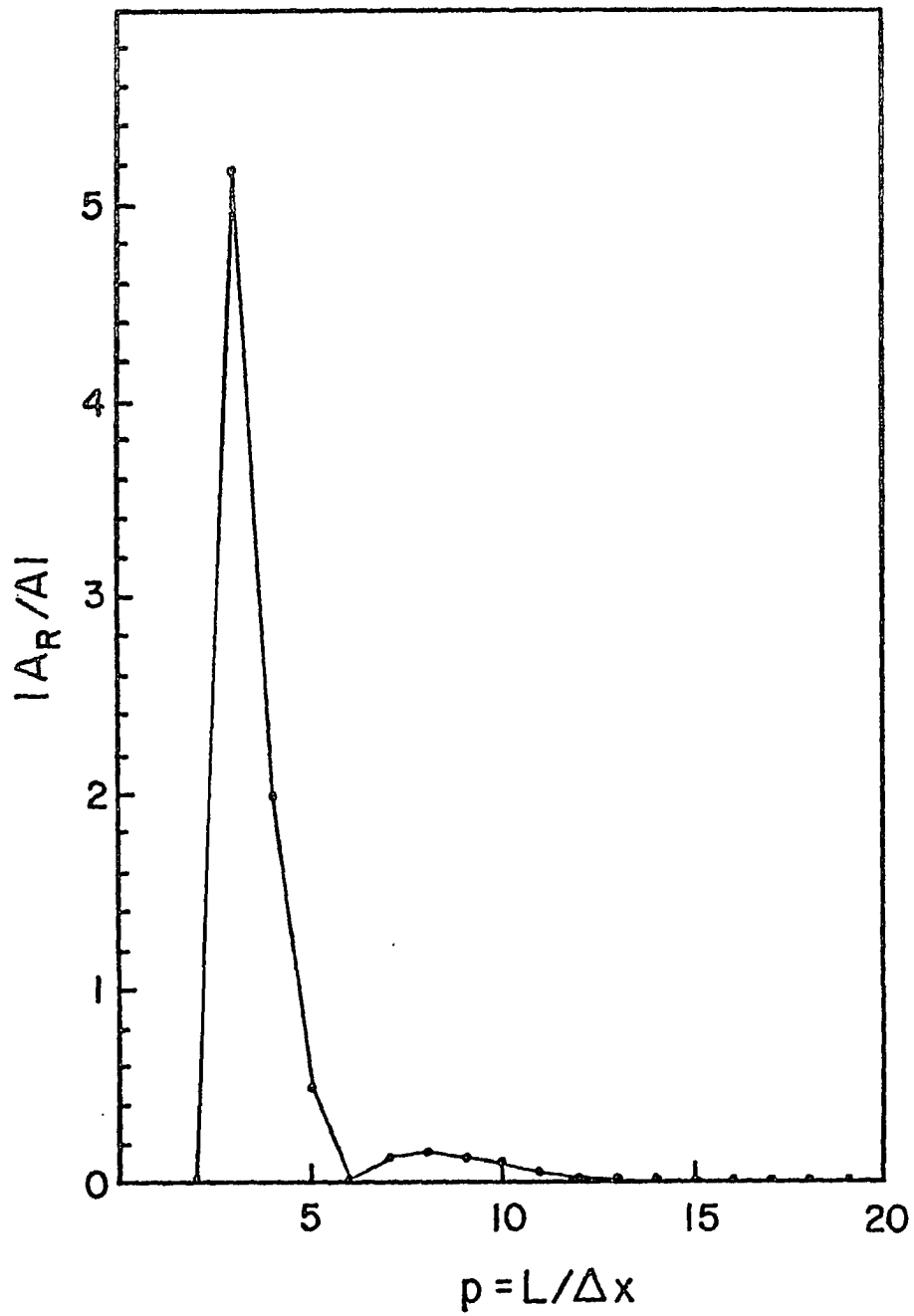


Fig. C.1. Relative amplitude of the spurious wave as a function of the wave numbers of the incident wave.

helpful because of the dispersive type of waves simulated in the numerical model. The relative amplitude $|A_R/A|$ of the spurious part of wave is plotted against the wave number p in Fig. C.1. It can be seen that for waves with wavelength larger than $5 \Delta x$ the reflectivity is satisfactory. In order to test this open boundary condition, a simple numerical experiment has been made for a one dimensional advection equation of the form

$$\frac{\partial u}{\partial t} + u \frac{\partial u}{\partial x} = g(x,t) . \quad (C.13)$$

If $g(x,t)$ is given by

$$g(x,t) = A k \cos k (x - c t) [(u_0 - c) + A \sin k (x - c t)] \quad (C.14)$$

then u has the analytic solution

$$u = u_0 + A \sin k (x - c t) . \quad (C.15)$$

Over a finite span along the x -axis numerical solutions of (C.13) are obtained. Then the numerical solution is compared with the analytic solution of (C.15) by computing the correlation coefficient between these two solutions. Although the finite-difference scheme adopted in the experiment does affect the correlation it is believed that the open boundary condition has the dominant effect because of the possibility of reflecting or transmitting waves. Consistent with the numerical scheme used in the study of the low-level jet simulation, the leap-frog scheme was used. Then

$$u_j^{n+1} = u_j^{n-1} + 2 \Delta t [g_j^n - u_j^n (u_{j+1}^n - u_{j-1}^n) / (2 \Delta x)] , \quad (C.16)$$

where the subscript and superscript have the usual meaning.

The constants used in the experiment are

$$A = 2. \text{ (m/sec) ,}$$

$$C = 20. \text{ (m/sec) ,}$$

$$\Delta t = 100. \text{ (sec) ,}$$

$$\Delta x = 5000. \text{ (meters) ,}$$

$$u_0 = 10. \text{ (m/sec) ,}$$

$$k = 2\pi/L = 2\pi/(p \Delta x) \text{ ,}$$

and

$$p = 6, 8, 10, 15.$$

At the first grid point $j = 1$, u is calculated according to (C.4) and at the grid point $j = 21$ the open boundary condition in (C.7) is used. At selected time steps the correlation between the numerical solutions and the analytic solution in (14) is evaluated. The definition of the correlation coefficient is as follows:

$$\rho_{12}^2 = \frac{\text{Cov.}[X_1, X_2]^2}{\text{Var.}[X_1]\text{Var.}[X_2]} \text{ ,} \quad (\text{C.17})$$

where

$$\text{Var.}[X_1] = E[(X_1 - \mu_1)^2] \text{ ,} \quad (\text{C.18})$$

$$\text{Var.}[X_2] = E[(X_2 - \mu_2)^2] \text{ ,} \quad (\text{C.19})$$

$$\text{Cov.}[X_1, X_2] = E[(X_1 - \mu_1)(X_2 - \mu_2)] \text{ .} \quad (\text{C.20})$$

The sample space for the numerical solutions and for the analytic solutions are denoted by X_1 and X_2 , respectively.

Table C.1. Correlation coefficients showing the relationship between analytic solutions and numerical solutions of the advection equation obtained with an open boundary condition; p is the wave number ($p = L/\Delta x$).

t(sec)	6	8	10	15
1. x 10 ³	0.966	0.992	0.998	1.000
2. x 10 ³	0.927	0.942	0.984	0.998
3. x 10 ³	0.959	0.980	0.979	0.992
4. x 10 ³	0.945	0.991	0.990	0.991
5. x 10 ³	0.953	0.978	0.997	0.992
6. x 10 ³	0.949	0.956	0.992	0.996
7. x 10 ³	0.964	0.986	0.987	0.997
8. x 10 ³	0.953	0.986	0.986	0.997
9. x 10 ³	0.938	0.976	0.991	0.997
10. x 10 ³	0.980	0.968	0.994	0.996
15. x 10 ³	0.945	0.985	0.992	0.996
20. x 10 ³	0.937	0.978	0.992	0.996
25. x 10 ³	0.978	0.984	0.992	0.995
30. x 10 ³	0.949	0.977	0.992	0.995
35. x 10 ³	0.939	0.983	0.992	0.996
40. x 10 ³	0.978	0.977	0.992	0.995
45. x 10 ³	0.949	0.983	0.992	0.996

The means of the samples are denoted by μ_1 and μ_2 , respectively, and $E[]$ is the expectation operator. The ensemble of this statistic is for the twenty-one grid points. Since a computational mode is induced by the leap-frog scheme a time filter is used to control this mode. That is,

$$\bar{u}_j^n = (u_j^{n+1} + 2u_j^n + u_j^{n-1})/4 . \quad (C.21)$$

The barred variable \bar{u}_j^n means the filtered value at time step n and grid point j . The results of this experiment are shown in Table C.1. The numerical values shown inside the table are the square of the correlation coefficient ρ_{12}^2 . And the symbol t represents the time after the initial integration. For waves with wavelength larger than $5\Delta x$ the numerical solution with an open boundary condition is quite satisfactory. This situation is maintained even after an integration of 12 hours. Thus, the open boundary condition in (C.7) is better than the Sommerfeld radiation boundary condition, when used in the finite-difference model. For practical use of the open boundary condition it is suggested that a stronger damping or low-pass filtering of the impending waves be employed near the open boundary such that it is insured that the impending waves have a wavelength larger than $5\Delta x$.